# MORPHOLOGY AND CONDUCTIVITY TUNING OF III-V SEMICONDUCTOR NANOWIRES

by

Omid Salehzadeh Einabad
M. Sc., Simon Fraser University, 2010

A THESIS SUBMITTED IN PARTIAL FULFILLMENT OF
THE REQUIREMENTS FOR THE DEGREE OF

DOCTOR OF PHILOSOPHY

In the
Department of Physics
Faculty of Science



SIMON FRASER UNIVERSITY

Summer 2013

APPROVAL

| | |
|---|---|
| Name: | Omid Salehzadeh Einabad |
| Degree: | Doctor of Philosophy |
| Title of Thesis: | Morphology and conductivity tuning of III-V semiconductor nanowires |

Examining Committee:

Chair: Dr. J. Steven Dodge, Chair
Associate Professor

_____

Dr. Simon Watkins, Senior Supervisor
Professor

_____

Dr. Karen Kavanagh, Supervisor

Professor

_____

Dr. George Kirczenow, Supervisor
Professor

_____

Dr. Erol Girt, Internal Examiner
Associate Professor

_____

Dr. Lincoln J. Lauhon, External Examiner
Professor, Department of Materials Science and Engineering, Northwestern University

Date Defended/Approved: July 29, 2013

# Partial Copyright Licence

ABSTRACT

Semiconductor nanowires (NWs) offer a wide range of opportunities to explore the fundamentals of the crystal growth process as well as the possibility to design and fabricate novel nano-scale devices. The rational design of these devices requires the understanding of the NW growth mechanism in order to control the NW size and morphology, the NW doping, and the ability to grow coherent heterostructures.

In this thesis, we grew gold-catalyzed III-V NWs via the vapour-liquid-solid (VLS) mechanism using the metalorganic vapour phase epitaxy (MOVPE) technique. We explored the details of VLS growth mechanisms by analyzing the dependence of NW growth rate on NW diameter. We presented a systematic study of the effect of precursor chemistry (i.e. group III precursor, and $CBr_4$ dopant on the growth of GaAs NWs. We showed that precursor chemistry can be employed as a useful means to grow axial or radial heterostructures.

A model to estimate the critical dimensions of core/shell NWs based on elasticity theory was presented. The numerical calculations were carried out for various III-V core/shell NWs and showed excellent agreement with experimental results.

We demonstrated both core and shell doping of GaAs NWs using Te- (*n*-type) and C- (*p*-type) dopants. Electrical measurements were performed using a nanoprobe within a scanning electron microscope on individual NWs and doping levels and conduction mechanisms were determined. The incorporation pathways of dopants into the NWs were discussed based on the analysis of the observed dependence of measured resistivity on NW diameter.

Keywords: GaAs; nanowire; carbon; tellurium; doping; heterostructures; MOVPE.
Subject Terms: nanowires; GaAs; III-V semiconductors.

**ACKNOWLEDGEMENTS**

I would like to thank my senior supervisor, Professor Simon Watkins, for his great patience and encouragement during this research. I am really grateful for all his guidance, valuable advice, unlimited support and the opportunity he gave me to work under his supervision.

I am thankful to my supervisory committee members, Dr. Karen Kavanagh and Dr. George Kirczenow. I especially like to thank Dr. Karen Kavanagh for helping me to interpret TEM results. I would like to thank Dr. Li Yang for training me to use the nano-imaging facilities. Special thanks to Bryan Gormann for all his help to keep the machines running.

I would like to thank all my lab-mates and friends and every member of the physics department for helping me during these five amazing and unforgettable years of my life at Simon Fraser University.

TABLE OF CONTENTS

## Contents

LIST OF FIGURES

LIST OF TABLES

LIST OF ABBREVATIONS

| | |
|---|---|
| BF | bright field |
| BP | boiling point |
| $CBr_4$ | carbon tetrabromide |
| DETe | diethyltellurium |
| DF | dark field |
| EDS | energy dispersive spectroscopy |
| FE | field emission |
| G-R | generation-recombination |
| GTE | Gibbs-Thomson effect |
| HRTEM | high resolution transmission electron microscope |
| MBE | molecular beam epitaxy |
| MFC | mass flow controller |
| MOVPE | metalorganic vapour phase epitaxy |
| MP | melting point |
| NP | nanoparticle |
| SAD | selected area diffraction |
| SEM | scanning electron microscope |

| | |
|---|---|
| NW | nanowire |
| TB | triple boundary |
| TBAs | tertiarybutylarsine |
| TEGa | triethylgallium |
| TEM | transmission electron microscope |
| TBP | tertiarybutylphosphine |
| TD | threading dislocation |
| TE | thermionic emission |
| TFE | thermionic field emission |
| TMIn | trimethylindium |
| TMGa | trimethylgallium |
| TMSb | trimethylantimony |
| ZB | zincblende |
| XRD | X-ray diffraction |
| WZ | wurtzite |

## Introduction

Semiconductor nanowires (NWs), grown via a bottom-up approach, are emerging as versatile building blocks for future nanoscale devices. The small diameters, as low as 3 nm [1], with atomically smooth surfaces are the key properties which make them superior over their lithographically scaled counterparts. In addition, the ability to grow axial and radial heterostructure NWs, that are difficult or impossible to grow in thin films, opens new opportunities to design and fabricate novel devices [2, 3]. Furthermore, the ability to integrate III-V NWs on Si substrates [4] is another characteristic which makes them desirable from the technological point of view. Some of the reported NW-based devices, such as wrapped-gate field effect transistors [5], have already shown better performance compared to their counterparts manufactured via top-down technology. Recently, axial and core/shell III-V NW solar cells have received considerable attention, and single junction cells with efficiencies up to 13.8% (InP-based axial p-i-n junction) [6] and 6.6% (GaAs-based radial p-i-n junction ) [7] have been reported. The rational design of these devices depends on the understanding of the NW growth mechanisms in order to control the NW size and morphology, the NW doping, and the ability to grow coherent heterostructures.

In the first chapter, I will outline the experimental procedures and apparatus used in this work. In the second chapter, I explore the basic aspects of Au-catalyzed GaAs NWs grown via vapor-liquid-solid (VLS) growth mechanism in a metalorganic vapor phase epitaxy (MOVPE) reactor. Analysis of the dependence of the NW growth rate on diameter and group III precursor partial pressure is an indirect approach to examine the VLS growth mechanism. In this method, agreement between the proposed model and the experimental data gives insight into the microscopic mechanisms involved in the VLS growth of the NWs.

Other parameters involved in the growth of III-V NWs include the growth temperature [8, 9], V/III ratio [9, 10], substrate material and orientation [11] and the size, spacing and choice of catalyst nanoparticles [12, 13]. In comparison, the precursor chemistry has received little attention [14]. In chapter 3, we investigate the effect of group III precursor chemistry on the morphology of GaAs NWs. We show that by the appropriate choice of group III precursor, one can grow axial or radial NW

heterostructures without changing other growth parameters. Another example of precursor chemistry, the effect of dopant precursor ($CBr_4$), will be presented in chapter 4.

In thin film lattice-mismatched heterostructures, the strain is predominantly accommodated by the layer. The structure remains coherent if the layer thickness is below a "critical thickness", otherwise the structure relieves the strain energy by forming dislocations at the heterointerface. In thin films, the critical thickness is usually estimated by the Matthews-Blakeslee's (M-B) theory, which is a force balance model [15]. This model relies on the assumption that pre-existing threading dislocations exist in the substrate surface prior to the layer growth. This assumption is not generally true in NWs since the initial core structures are free of dislocations. Therefore, equilibrium energy models are widely employed in NW heterostructures to determine the critical dimension of the axial [16] and radial [17-19] heterostructures. In radial NW heterostructures, depending on the dimensions of the structure, both core and shell materials can share the strain. This partitioning of the strain in core/shell NWs is expected to result in critical thicknesses above the values reported for thin film heterostructures. In chapter 5, we present an equilibrium energy model based on elasticity theory to estimate the geometric limits of coherent III-V core/shell NWs and compare the predictions with experimental results we found for different III-V core/shell NWs.

Control of NW doping is still a challenging area for crystal growers. In VLS growth of NWs, dopant atoms may incorporate into the NWs via (1) diffusion through a dopant-NP solution into the NW or (2) diffusion through the NP/NW interface from the vapor phase into the NW. Also, dopant atoms may incorporate from the vapor phase directly into the layer grown on the facets of the NWs to form a doped shell around the core. In chapter 6, we demonstrate controlled tellurium- (*n*-type) and carbon- (*p*-type) doping of GaAs NWs, both core doping via VLS growth and shell doping via the vapour-solid (VS) growth mechanisms. We performed electrical measurements inside a scanning electron microscope by contacting individual NWs by a tungsten nanoprobe to determine the doping levels of the NWs. Accurate determination of the dopant atoms distribution across the NW is challenging and requires precise measurements using atom probe tomography [20] or holography [21] techniques. In this work, we employed a rather

indirect method to infer the dopant distribution across the NW. In addition to the effects of sidewall depletion of doped GaAs NWs, the presence of any radial inhomogeneity in dopant distribution must result in a variation in the ***measured*** resistivity of the NWs with NW radius. Therefore, based on diameter dependent analysis of the measured resistivity, we could infer information about the radial distribution of the dopants and the incorporation pathways of the dopants into the NWs.

# 1: EXPERIMENTAL METHODS

This chapter provides an overview of the experimental methods used for nanowire (NW) growth and characterization. NW fabrication was performed using metalorganic vapour phase epitaxy (MOVPE). Scanning electron microscopy (SEM) and transmission electron microscopy (TEM) were used for structural characterization. Electrical measurements were performed using a nanoprobe inside an SEM chamber.

## 1.1 Metalorganic vapour phase epitaxy (MOVPE)

MOVPE is a synthesis technique to grow epitaxial single crystal films or NWs on single crystal substrates. In this process the metalorganic chemical constituents (precursors), containing the required chemical elements bound to a hydrocarbon ligand, decompose in the vapour phase and react on a heated substrate to form a solid crystalline deposit. An alternative name for this process is metalorganic chemical vapour deposition (MOCVD).

### 1.1.1 MOVPE system

In this work, we used a Thomas Swan vertical MOVPE reactor, operating at a pressure of 50 Torr, to grow the NW samples. Figure 1.1 shows three main components of a vertical MOVPE system:

- The reactant supply.
- The deposition system or reactor.
- The exhaust system.

Most of the metalorganic precursors are liquid at room temperature and are stored in stainless steel bubblers (Fig. 1.2) which are held in a temperature controlled bath filled with ethylene glycol. A carrier gas (such as $H_2$) bubbles through the liquid precursor and transfers the saturated mixture to the reactor via the run line. There are three-way valves on the vent/run line that switch the precursor flow to the run (reactor) or vent (exhaust)

lines. The system includes pressure balanced run and vent lines to keep the precursor flow constant and to make fast switching of the precursor flow to the reactor possible, while minimizing pressure transients. The control of the carrier gas and precursor flow is performed by electronic pressure controllers (EPC) and mass flow controllers (MFC).

To minimize unwanted pre-reactions, the group III and V precursors are carried into the reactor via separate run lines. The precursor mixing happens above a showerhead in the reactor. The precursor cracking and deposition occurs above a substrate which is mounted on a susceptor that is heated to the growth temperature. The susceptor rotates at 15 rpm in order to ensure uniform growth rate and composition of alloys. An optical pyrometer was used to control the temperature. The *p*- and *n*-dopant sources were carrier from the lower and upper run lines to the reactor, respectively.

The decomposition reactions are never complete and some of the precursor materials may reach the exhaust without reacting. In addition, many of the by-products of the reaction are toxic. This means all these effluents must be eliminated or neutralized before they are released to the environment. The exhaust manifold includes a particle trap, which collects solid particles originating in the reactor, which might otherwise damage the pump. The trap also minimizes back-streaming of pump oil into the reactor and subsequent contamination. A chemical duty vacuum pump is used to control the pressure and gas velocity inside the reactor. Downstream from the pump, the exhaust gases pass through an oil mist eliminator and an activated carbon scrubber, where they are eventually oxidized.

If the vapour pressure ($P_V(T)$) of the liquid reactant is known, its flow rate ($f_p$) can be calculated, using the ideal gas law, and controlled by the volume flow rate of the carrier gas ($F_H$, cm$^3$/min), bubbler pressure ($P_B$), and temperature ($T$) [22]:

$$f_p = \frac{F_H}{22407.47}\frac{P_V(T)}{P_B - P_V(T)} \text{ (mol/min)} \qquad (1.1)$$

The vapour pressure of the precursor depends on the bubbler temperature and two other empirical parameters ($a$ and $b$) that are characteristic of each material (summarized in Table 1.1):

$$P_V(T) = 10^{a-b/T} \text{ (Torr)} \qquad (1.2)$$

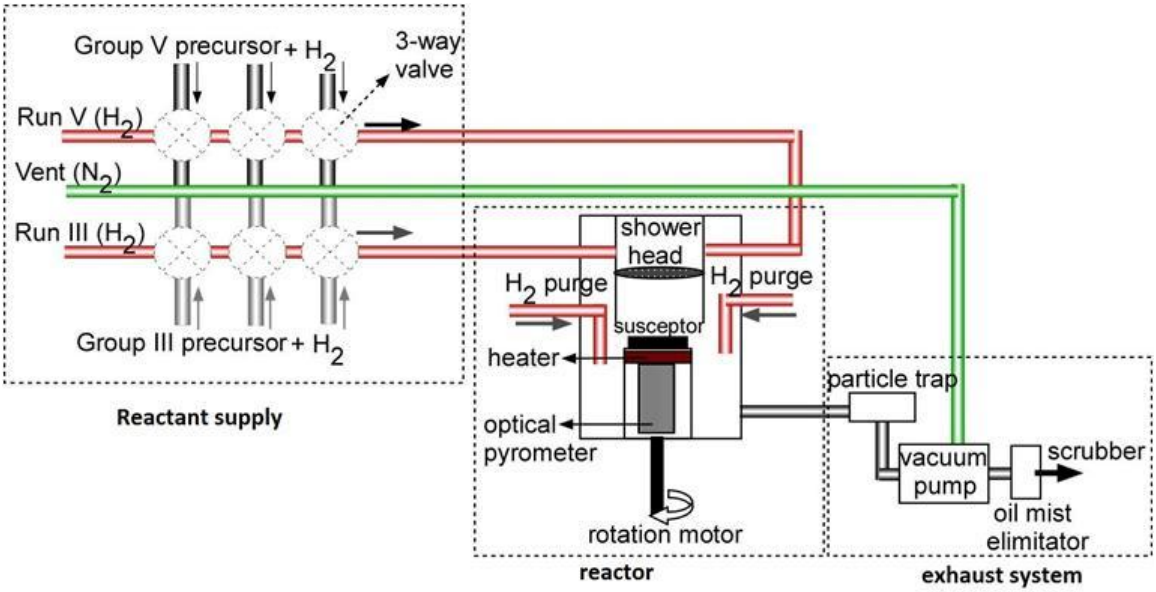


Figure 1.1. Schematic of an MOVPE system.

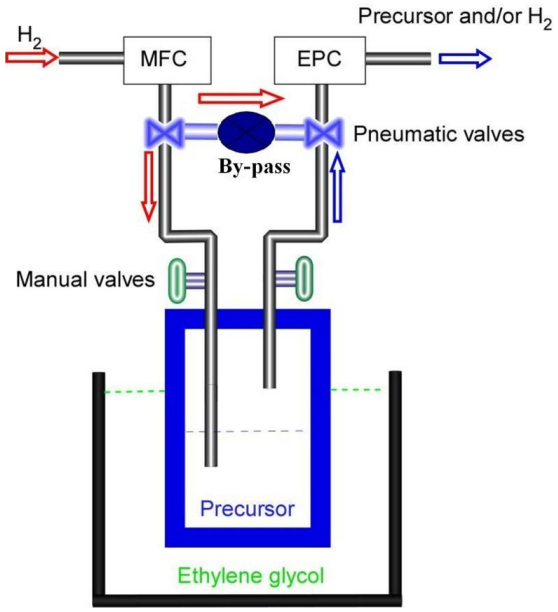


Figure 1.2. Schematic of a precursor bubbler placed in a temperature bath filled with ethylene glycol.

### 1.1.2 Decomposition of the metalorganic precursors

Metalorganics are compounds in which the atom of a metal is bound to one or more carbon atoms of an organic hydrocarbon group. Metal-alkyls ($M\text{-}C_n H_{2n+1}$) are the major MOVPE precursors. In this work, we used trimethylgallium (TMGa), triethylgallium (TEGa) and trimethylindium (TMIn) as group III precursors and tertiarybutylarsine (TBAs), tertiarybutylphosphine (TBP) and trimethylantimony (TMSb) as group V precursors. Diethyltellurium (DETe) and $CBr_4$ were use as Te and C dopant sources. A summary of the physical properties of the metalorganic precursors is given in Table 1.1.

Homolysis and β-hydride elimination are the two common types of pyrolysis (thermal decomposition) that occur in the gas phase. In a homolysis decomposition reaction, a molecule is split into reactive radicals with no mass transfer between fragments. In β-hydride elimination, a hydrogen atom on one of the hydrocarbon ligands transfers to the metal with the liberation of a nonreactive alkene.

Table 1.1. A summary of the physical properties of the organometallic precursors used in this study [22].

| Abb. | Name | Chem. form. | MP [˚C] | BP [˚C] | *a* | *b* [K] | $T_{bubbler}$ [˚C] |
|---|---|---|---|---|---|---|---|
| TEGa | Triethylgallium | $(C_2H_5)_3Ga$ | -82.3 | 143 | 8.08 | 2162 | 18 |
| TMGa | Trimethylgallium | $(CH_3)_3Ga$ | -15.8 | 55.8 | 8.07 | 1703 | -10 |
| TMIn | Trimethylindium | $(CH_3)_3In$ | 88.4 | 133.8 | 10.52 | 3014 | 18 |
| TBAs | Tertiarybutylarsine | t-$(C_3H_9)AsH_2$ | -1.0 | 68 | 7.24 | 1509 | 10 |
| TBP | Tertiarybutylphosphine | t-$(C_3H_9)PH_2$ | 4.0 | 54 | 7.71 | 1539 | 10 |
| TMSb | Trimethylantimony | $(CH_3)_3Sb$ | -87 | 80 | 7.70 | 1697 | 10 |
| DETe | Diethyltellurium | $(C_2H_5)_2Te$ | -30 | 117.6 | 7.99 | 2093 | - |

TMGa decomposes via homolysis, producing highly reactive $CH_3$, as follows [23]:

$Ga(CH_3)_3 \rightarrow CH_3 + Ga(CH_3)_2$

$Ga(CH_3)_2 \rightarrow CH_3 + Ga(CH_3)$

$Ga(CH_3) \rightarrow CH_3 + Ga$

The bond dissociation is an endothermic reaction and requires specific amount of heat energy, known as the activation energy ($E_a$). A molecular orbital calculation of the first Ga-$CH_3$ bond energy gives a value of 64.9 kcal/mol [24] in a close agreement with the experimentally determined value of $E_a$ = 64.6 kcal/mol. Complete decomposition of TMGa occurs at an approximate temperature of 470 ˚C [25]. Similar to TMGa, TMIn decomposes via homolysis. The first order activation energy of TMIn in $H_2$ ambient is 39.8 Kcal/mol and the complete decomposition occurs at an approximate temperature of 350 ˚C [26].

TEGa pyrolyzes by β-hydride elimination with the formation of $GaH_3$ and three ethylene molecules ($C_2H_4$) [27] which are non-reactive carbon-containing species, as follows:

$Ga(CH_3\text{-}CH_2)_3 \rightarrow CH_2 = CH_2 + GaH(CH_3\text{-}CH_2)_2$

$GaH(CH_3\text{-}CH_2)_2 \rightarrow CH_2 = CH_2 + GaH_2(CH_3\text{-}CH_2)$

$GaH_2(CH_3\text{-}CH_2) \rightarrow CH_2 = CH_2 + GaH_3$

The first order reaction is the rate limiting step with an experimentally determined $E_a$ = 47 Kcal/mol [28], consistent with a calculated value of 44 Kcal/mol [24]. Complete decomposition of TEGa occurs at an approximate temperature of 340 ˚C [29].

Pyrolysis of TBAs is a complex process and different decomposition pathways have been postulated [22]. One possibility is β-hydride elimination which involves the transfer of a hydrogen atom from the butyl radical to the As atom to form $C_4H_8$ and $AsH_3$ (Fig. 1.3(a)). The other possibility is the intermolecular coupling reaction which involves the breaking of As-H and As-C bonds and formation of a bond between the H and central C atoms. This process will produce AsH and $C_4H_{10}$ (Fig. 1.3(b)). In general, parallel decomposition pathways are considered for TBAs pyrolysis with β-hydride elimination to be the dominant mechanism [30].

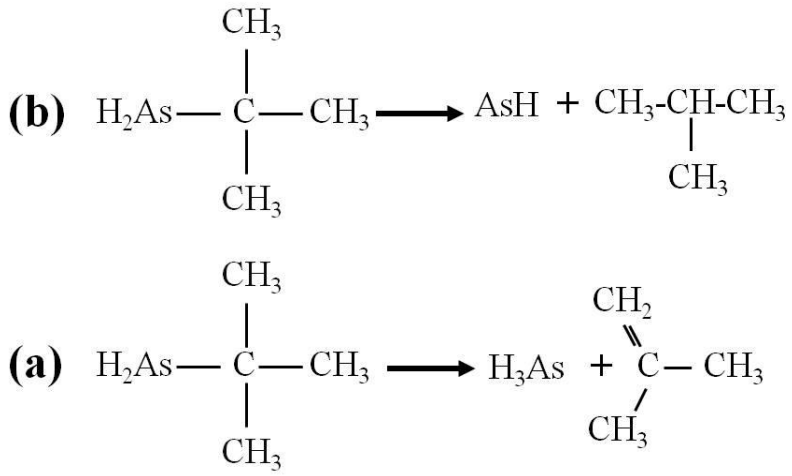


Figure 1.3. Pyrolysis of TBAs through a) β-hydride elimination and b) intermolecular coupling.

### 1.1.3 Basics of the MOVPE growth process

MOVPE reactions are governed by *thermodynamics* and *kinetics.* Thermodynamics determines whether the desired reaction can take place or not. A given reaction can occur if the change of the free energy is negative. Kinetics determines the rate at which the chemical reaction occurs.

The rate-limiting step is generally determined by either the mass transport or by surface reaction kinetics. When the growth rate is limited by mass-transport phenomena, the controlling factor is the diffusion rate of the reactant through the carrier gas which forms a boundary layer on the substrate. The boundary layer is the region above the heated substrate in which the flow velocity changes from the bulk gas velocity (away from the substrate) to zero at the substrate. This usually happens when the temperature is high. At high temperature, surface reactions are very fast, therefore diffusion becomes the rate limiting step for the transport of reactants to the surface. Surface reaction kinetics is the limiting factor at lower temperatures where the surface reaction rates are smaller.

### 1.1.4 Thin film growth modes

On an atomically flat substrate, the epitaxial growth mode depends on the lattice mismatch between the substrate and the epilayer, the interaction strength between the adatoms and the substrate surface, and the perfection of the substrate surface. The step-flow growth mode is common on substrates with imperfections (see Fig. 1.4) which might be introduced intentionally (presence of step edges and terraces on a miscut substrate) or unintentionally (such as kinks or vacancies). On a defect free substrate surface, three growth modes are possible (see Fig. 1.5): (1) layer-by-layer (Frank-Van der Merwe (F-V)), (2) island formation (Volmer-Weber (V-W)), and (3) layer plus island growth (Stranski-Krastanov (S-K)).

After diffusion through the boundary layer, in the vicinity of the heated substrate precursors will fully or partially decompose. In the first step of the growth, the decomposed precursors will be physisorbed on the heated substrate and may migrate on the substrate or desorb back into the gas phase. The physisorbed adatoms then preferentially attach to the low energy sites such as step edges, kinks or vacancies, as shown in Fig. 1.4. These step edges grow until they meet each other or meet the edges of the substrate. This is called the step-flow growth mode.

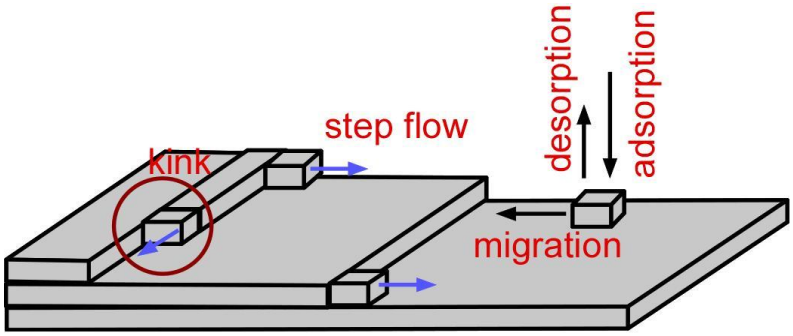


Figure 1.4. Schematic of the step-flow growth.

In the F-V growth mode, the interactions between adatoms and substrate are strong and the adatoms preferentially attach to the substrate sites resulting in atomically flat layer. In this growth mode, a complete layer forms prior to the formation of the next layer (Fig. 1.5(a)). In the V-W mode, interactions between adatoms are stronger than

those of the adatom with the surface, resulting in the formation of three-dimensional islands. The growth of these islands and coarsening results in rough multi-layer films on the substrate (Fig. 1.5(b)). During the coarsening process, the smaller islands lose their surface atoms to the larger islands and get smaller, while the larger ones get larger. S-K growth occurs for interaction strengths somewhere in the middle. S-K growth starts with layer-by-layer growth mode up to a critical thickness (about 3 monolayer in the growth of GaSb on GaAs substrate) and then switches to island growth mode (Fig. 1.5(c)).

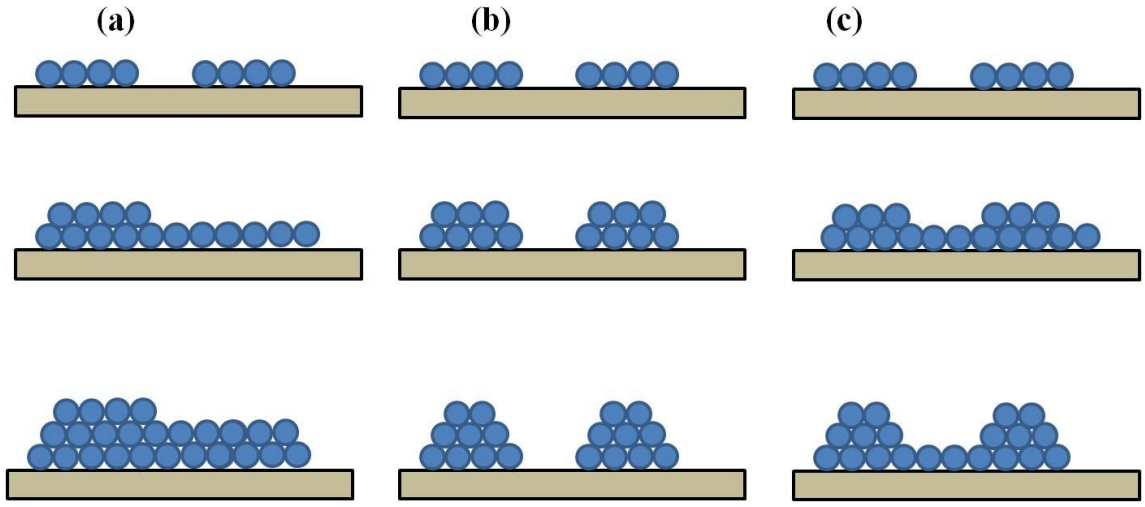


Figure 1.5. Schematic of the three primary growth modes in thin films (a) layer-by-layer (Frank-Van der Merwe), (b) island formation (Volmer-Weber) and (c) layer plus island (Stranski-Krastanov).

### 1.1.5 Nanowire growth

The growth of NWs has been accomplished by a variety of techniques including MOVPE, molecular beam epitaxy (MBE) and chemical beam epitaxy. The use of metal nanoparticles (NP) as catalysts is the most common approach to grow the NWs. In III-V NWs, the metal NP can be a foreign material such as Au or a droplet formed by the group III precursor. Another approach is catalyst free selected-area epitaxy which allows control of the position of the NW arrays and their diameters by means of a lithographically patterned dielectric layer on a substrate.

In the case of foreign metal assisted NW growth, the metal nanoparticle should not be reactive or soluble in the semiconductor which is to be grown. The choice of metal nanoparticle is also important in the case of NW doping (see chapter 6). It's generally assumed that these nanoparticles enhance the decomposition of the growth precursors in their immediate vicinity, and are not normally consumed during the growth process.

The first metal assisted NW growth was reported by Wagner and Ellis in 1964 [31]. They grew Si "whiskers" using Au particles on Si substrates. The schematic of the growth steps are outlines in Fig. 1.6. First a thin Au layer was thermally deposited on the substrate and then loaded in a chemical vapor deposition reactor. In the second step, the Au-coated wafer was annealed at a temperature above the eutectic temperature of Au and Si ($T > 363$ ˚C). During the heating, according to the Au-Si phase diagram, shown in Fig. 1.7, Si from the substrate diffuses into the Au and at $T > 363$ ˚C forms a liquid Au-Si alloy (18 atomic percent Si). Then, the thin liquid Au/Si layer de-wets the substrate surface and NPs are formed. The diffusion of Si from the substrate into the Au/Si liquid NPs continues following the equilibrium temperature and composition of the Si-rich liquidus line. A dashed line in Fig. 1.7 shows the change in the composition of Au during the annealing step. In the third step, the gas phase precursor is introduced ($SiCl_4$). Wagner and Ellis proposed two possibilities for the roles of the alloyed particles involved in the whisker growth. They argued that ***liquid*** Au/Si NPs have unity absorption coefficient (100% absorption) and therefore the cracked precursors preferentially would incorporate into the alloyed particles. They also speculated that the alloyed particles might act as catalysts. The first argument was later questioned by many authors [12, 32, 33]. Most likely, Au/Si particles act as catalysts enhancing the decomposition efficiency of the precursors in the vicinity of the NPs as will be discussed in chapter 3. In the final step, two scenarios may happen. At low temperatures (close to the eutectic temperature), the thermal energy is not enough to crack the precursors away from the alloyed particles. Therefore, precursors only decompose catalytically in the vicinity of the alloyed particles and incorporate preferentially into the Au/Si particles. The incorporation of the cracked precursors into the alloyed particles is driven by the high concentration gradient in the vicinity of the particles surface and the particle/NW interface. According to the Au-Si

phase diagram, a further increase in the concentration of Si in the alloyed particles will result in the precipitation of solid Si in the particle/NW interface. This growth process is called the vapor-liquid-solid (VLS) mechanism where the precursors are in vapor phase, the alloyed particle is in the liquid phase and the NW is in the solid phase. At low temperatures the cracked precursors only result in VLS growth of the NWs. At high temperatures, the thermal energy might be enough to crack the precursors even away from the alloyed particles. Therefore, at high temperatures, in addition to VLS growth, the cracked precursors directly deposit on the substrate and on the NW side facets via vapor-solid (VS) growth. This results in tapered NWs.

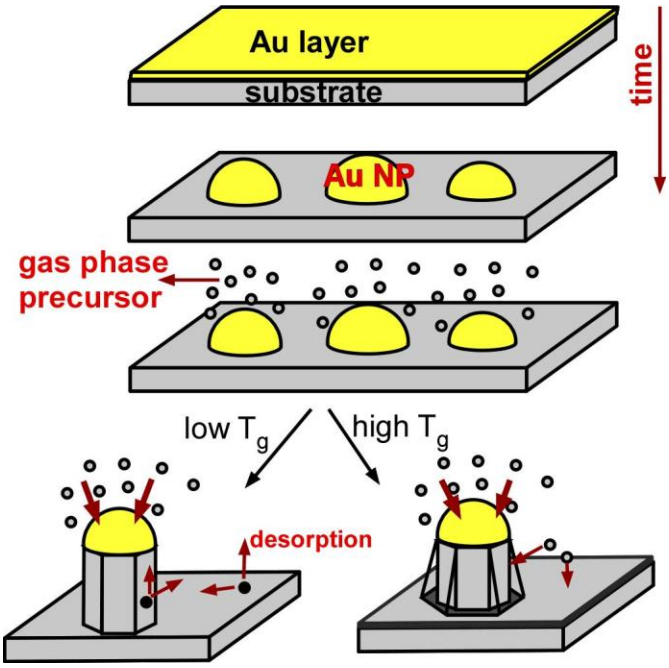


Figure 1.6. Schematic of NW growth via Au-catalyzed VLS growth mechanism. The open and solid circles represent the cracked and uncracked precursors.

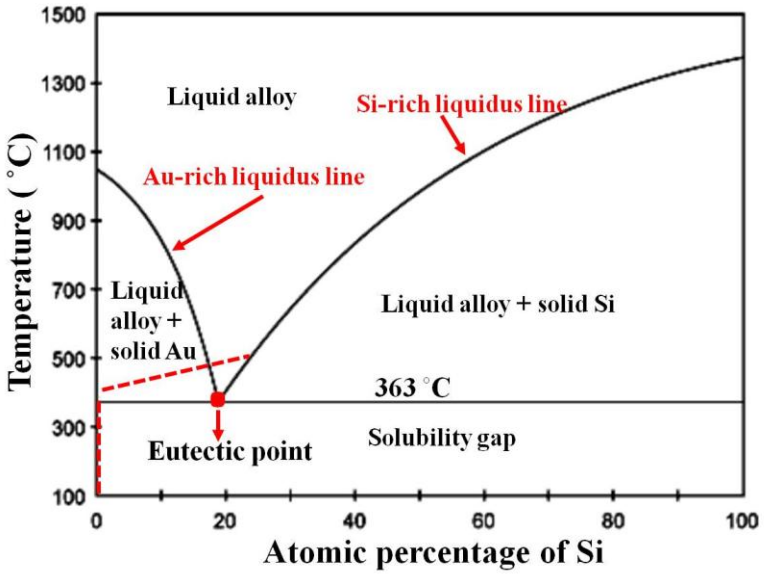


Figure 1.7. Phase diagram of Au-Si showing the VLS process.

The growth of III-V compound NWs requires the incorporation of two precursors and is more complicated than the growth of Si NWs. However, in the case of GaAs, As has a low solubility in Au [34]. Ga and Au form alloy above 346 ˚C, therefore it's believed that the Ga dissolves in the Au NP and it is speculated that As diffuses through the boundary of the NP/NW interface to incorporate in the NW [35]. Therefore, the Au-Ga phase diagram (with a eutectic temperature of 346 ˚C), shown in Fig. 1.8, is used instead of the ternary Ga-As-Au phase diagram to describe the primary features of VLS growth of GaAs NWs using Au NPs.

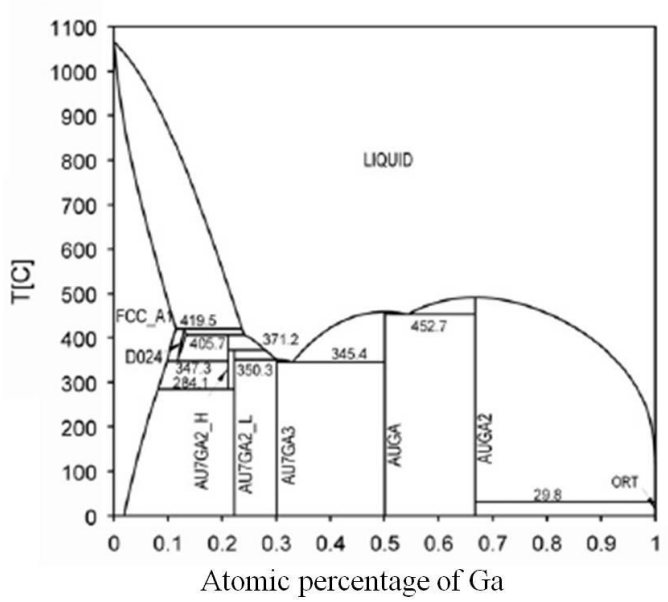


Figure 1.8. Au-Ga phase diagram [134].

### 1.1.6 Critical shell thickness

When an epitaxial layer is grown on a substrate with a different lattice constant, initially the layer distorts itself to have an in-plane lattice constant similar to the substrate's in-plane lattice constant as shown in Fig. 1.9(a). This lattice deformation builds-up strain energy in the layer. If the layer thickness exceeds a specific value known as the critical thickness, the formation of misfit dislocations at the layer/substrate interface will be energetically favourable relieving a portion of strain as shown in Fig. 1.9 (b). In other words, a dislocation will form if the initial strain energy before relaxation exceeds the sum of the residual strain energy after relaxation and the self-energy of the dislocation (energy due to the stress field of a dislocation).

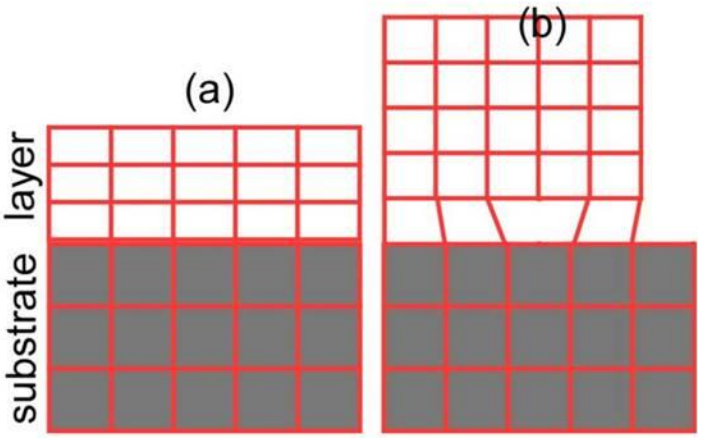


Figure 1.9. Schematic of a (a) coherent and (b) a relaxed heterostructures by a misfit dislocation at the substrate/layer interface.

Several theories have been proposed to calculate the critical thickness in thin film heterostructures. Matthews-Blakeslee's (M-B) theory, due to its simplicity, is widely used [15]. M-B theory is based on the existence of threading dislocations (TDs) in the substrate prior to the layer growth. A schematic of the formation of a dislocation via the M-B mechanism is shown in Fig. 1.10. To calculate the critical thickness, they equated the force exerted on the dislocation by the stress field, generated by the lattice mismatch, to the sum of the line tension of the TD and the Peierls force (friction force) which oppose the glide of the pre-existing TD. We should note that the value predicted by M-B theory is usually smaller than the experimental value by a factor of around 2.

The source of the pre-existing TDs in mismatched heterostructures is not clear. One possibility is the presence of pre-existing TDs in the substrate as shown in Fig. 1.10. Another argument is that the dislocations are not pre-existing and form during the heterostructure growth process. The half-loop dislocations likely nucleate on the free surface where the local stress concentration is a maximum followed by a glide process toward the substrate/layer interface [36]. Further discussion of dislocation formation mechanisms is outside of the scope of this dissertation.

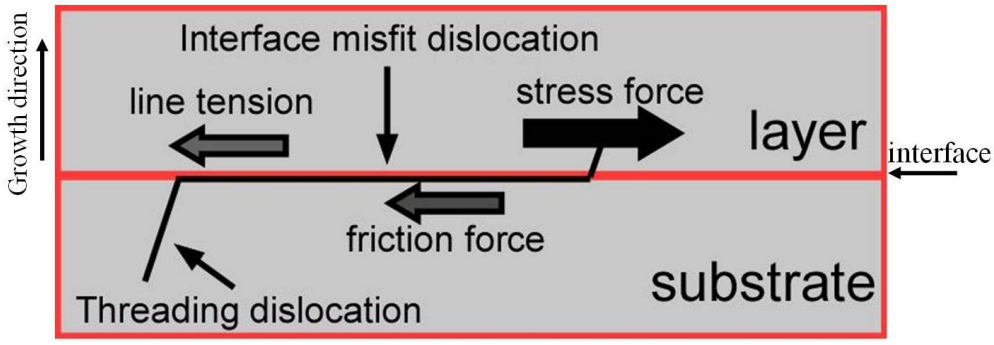


Figure 1.10. Cross-sectional illustration of the formation of a misfit dislocation at the substrate/layer interface by extension of a pre-existing threading dislocation from the substrate.

## 1.2 Electrical measurements

Electrical measurements were performed using a tungsten nanoprobe inside a scanning electron microscope (FEI Strata dual-beam DB235) chamber. The NWs were standing vertically on the substrate and were contacted individually by the nanoprobe to the Au NP on the tip of the NW as shown in Fig. 1.11(a). Large area indium and indium/zinc contacts on the backside of the *n*-GaAs and *p*-GaAs substrates, respectively, served as the second contact. Considering the equivalent circuit of the measurement setup shown in Fig. 1.11(b), the current passing through the NW, in general, will be a rectifying current passing through the Au NP/NW interface which acts as a diode, and is limited by the series resistance of the NW. In the case where the resistance of the NW is much larger than the shunt leakage resistance of the measurement system, the current will be dominated by the shunt leakage current (from the measurement circuit). A simple outline of a metal-semiconductor contact will be given in the following.

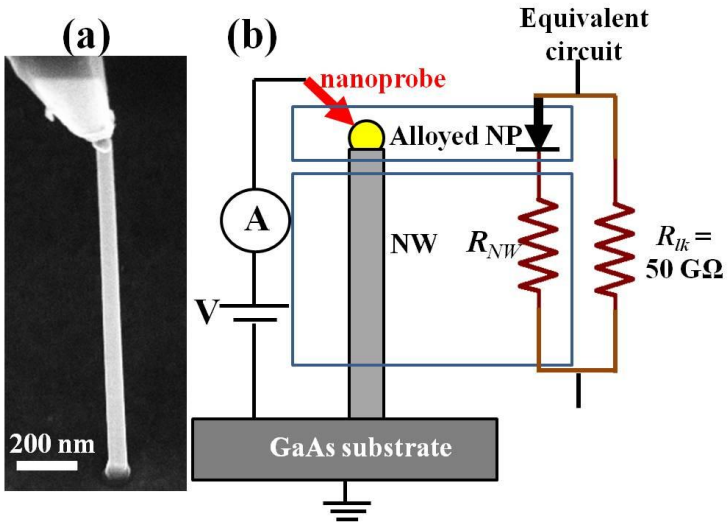


Figure 1.11. (a) An SEM image of a tungsten nanoprobe contacting the Au tip of a Te-GaAs NW and (b) schematic and the equivalent circuit of the measurement setup.

### 1.2.1 Rectifying transport characteristics

The first explanation of the commonly observed current rectification in moderately doped semiconductor and metal contacts was given by Schottky and Mott independently in 1938. They pointed out that the observed rectification can be explained by considering a barrier at the metal-semiconductor interface.

Figure 1.12 (a) shows the energy band diagram of a metal and an n-type semiconductor before contact. The Fermi level ($E_f$) of the semiconductor is higher than the $E_f$ of the metal. Therefore, after contacting them, the electrons from the semiconductor will flow into the metal leaving positively ionized impurities in the semiconductor (the depletion region) and building up a negatively charged region, which is much narrower compared to the depletion width $l_{dep}$ in the semiconductor. Equilibrium is reached when the $E_f$ of the metal and the semiconductor line up with each other. This process results in $E_f$ lowering of the semiconductor by an amount equal to the $q.(\varphi_m - \varphi_{sc})$ ($q\varphi_m$ and $q\varphi_{sc}$ are the work functions of metal and semiconductor, respectively, and $q$ is the charge on an electron) and an upward bending of the valence ($E_v$) and conduction ($E_c$)

bands in the semiconductor and the creation of a built-in potential energy ($qV_{bi0}$) in semiconductor which prevents further electron flow from semiconductor to metal. Likewise, the electrons in the metal encounter a barrier ($q\varphi_{b0}$) to flow into the semiconductor. Applying positive bias to the metal reduces the built-in potential energy ($qV_{bi} = qV_{bi0} - qV_{app}$) and therefore the electron flow from the semiconductor to the metal increases exponentially with the applied bias. At high positive bias, the current saturates due to the series resistance of the semiconductor. If we apply a negative voltage to the metal (reverse bias), the energy barrier remains unchanged but the depletion width become larger and therefore a very small current flows under reverse bias, limited ideally by the fixed barrier height ($q\varphi_{b0}$). A comprehensive discussion of the metal-semiconductor contacts can be found in ref. [37]

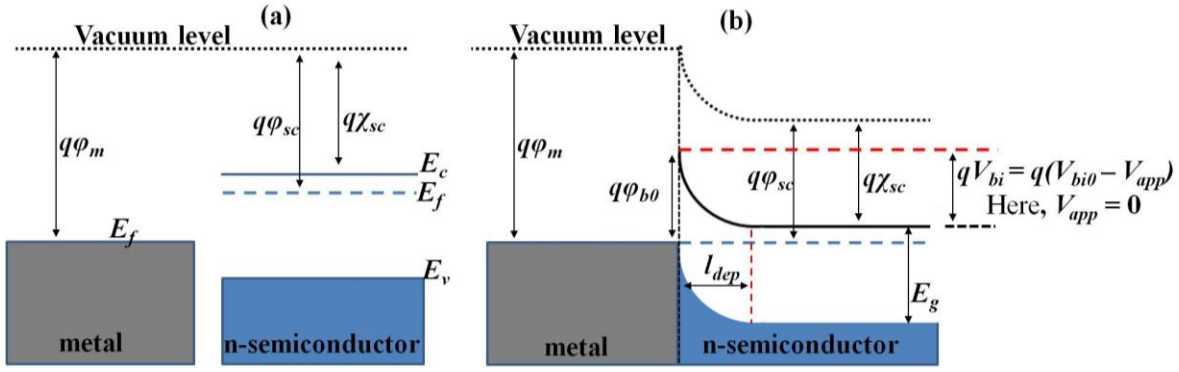


Figure 1.12. Energy band diagram of a metal and n-semiconductor (a) before and (b) after contact under zero applied bias.

In general, the *I-V* characteristics of a metal-semiconductor diode, including the series resistance ($R$), can be described by the following semi-empirical equation [37]:

$$I_{diode} = I_0\left(e^{\frac{q(V-IR)}{nk_BT}} - 1\right) \tag{1.3}$$

with

$$I_0 = AA^*T^2e^{\frac{-q\varphi_{b0}}{k_BT}} \tag{1.4}$$

where $I_0$ is the saturation current that is exponentially related to the zero bias barrier height ($\varphi_{0b}$), $A$ is the cross-sectional area of the Au NP/NW interface, $A^*$ is Richardson's constant (74.4 $A \cdot cm^{-2} \cdot K^{-2}$ for *p*-GaAs and 8.16 $A \cdot cm^{-2} \cdot K^{-2}$ for an n-type GaAs), and $n$ is the ideality factor. Three major transport mechanisms in metal/doped-semiconductor contacts are: thermionic emission (TE), thermionic field emission (TFE) and field emission (FE). TE corresponds to an ideality factor of one. In TE, the depletion width is large and the carriers are transported by thermal emission over the barrier height ($q\varphi_{b0}$). TE is common in metal-semiconductor with low doping level ($< 10^{17}$ $cm^{-3}$). In the TFE mechanism, the ideality factor is slightly larger than unity. TFE occurs in metal-semiconductor junctions with moderate doping level ($10^{17}$-$10^{18}$ $cm^{-3}$) where the carriers tunnel through the top of the barrier. In FE, the semiconductor doping level is high ($\sim 10^{19}$ $cm^{-3}$) and the depletion region is narrow enough for the carriers to tunnel through the entire barrier, which results in a linear or nearly linear *I-V* characteristics. The contact between a *heavily* doped semiconductor and a metal is commonly known as a tunnel diode. These transport mechanisms are schematically shown in Fig. 1.13.

Generation (dominant in reverse bias) and recombination (dominant in forward bias) of carriers in the depletion region of a metal-semiconductor contact is another transport mechanism which is common in doped semiconductors with deep level traps. This transport mechanism results in an ideality factor of close to 2.

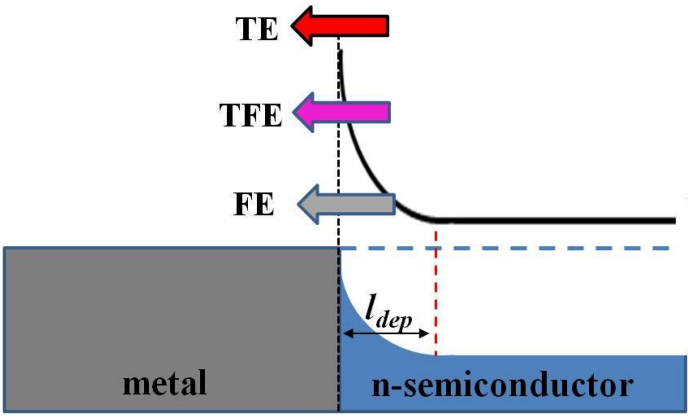


Figure 1.13. Schematic energy band diagram of a metal/n-semiconductor contact showing three major transport mechanisms: thermionic emission (TE), thermionic field emission (TFE) and field emission (FE).

### 1.2.2 Space-charge-limited current transport

The analogy of charge transport through an intrinsic semiconductor or an insulator, known as space-charge-limited current (SCLC) transport, to a vacuum diode was first pointed out by N. F. Mott and R. W. Gurney in 1940 [38]. Two requirements which must be fulfilled to observe SCLC flow through an intrinsic semiconductor are (1) the formation of at least one contact at the metal electrode and semiconductor interface with a small barrier height and (2) the presence of no or low free carrier concentration (background doping) within the semiconductor. Under these conditions, SCLC flow will be observed when the density of the injected charge is higher than the density of the thermally generated carriers within the semiconductor. In particular, these conditions should be easily met in thin semiconductor nanowires (NWs). Due to their high surface to volume ratio, NWs are more sensitive to surface states compared to bulk materials. These surface states result in sidewall depletion ($l_d$) of the GaAs NWs where $l_d$ its length is inversely proportional to the square root of the carrier concentration. Therefore, if the sidewall depletion length exceeds the NW radius, the NW will be depleted of free carriers.

In a trap-free insulator or intrinsic semiconductor (bulk case), the current density ($J$) is related to the applied voltage ($V$) by [38, 39]:

$$J = \varepsilon\mu\frac{V^2}{L^3} \tag{1.5}$$

where $\varepsilon$, $\mu$ and $L$ are the permittivity of the semiconductor, the carrier mobility and the separation between electrodes, respectively. The above equation can be understood by considering the electrodes as a parallel plate capacitor where the injected amount of charge is proportional to the applied voltage and the transition time between two electrodes is inversely proportional to the applied voltage. Therefore, the current flowing between electrodes (amount of charge per unit time passing through the electrodes) is proportional to $V^2$. Experimental results of SCLC conduction in thin NWs are qualitatively in agreement with the theory for bulk materials. However, Talin et al [40]. argued that, in thin NWs with length of $L$ and radius of $R$, the SCL current is enhanced due to a poor screening of the injected carriers. By examining the experimental data obtained for GaN NWs, they suggested the following modified formula in the case of a NW with length of $L$ and radius of $R$:

$$J = (\frac{L}{R})^2\varepsilon\mu\frac{V^2}{L^3} \tag{1.6}$$

## 1.3 Transmission electron microscopy (TEM)

### 1.3.1 TEM system

In this work, we used a FEI Tecnai field emission Scanning TEM. A TEM is composed of an electron source, magnetic lenses, and condenser and objective apertures as shown in Fig. 1.14. Also, there are several pumps to keep the electron column under high vacuum. A thermionic (tungsten or lanthanum hexaboride filaments) or field-emission (fine tungsten needle) electron source on top produces a stream of coherent electrons. Magnetic lenses in a TEM control all the operational functions of the instrument such as focusing and magnifying the image. There are four basic lenses in a TEM: condenser (C1 and C2), objective, intermediate and projector lens. The condenser and the objective apertures are other key components of a TEM. The condenser aperture is a metal disk with different sized holes located under the condenser lens, whose role is

to knock out the high angle electrons from the beam (those far from the optical axis). The objective aperture, which is a disk with different sized holes on it, is placed at the back focal plane of the objective lens and is used to choose which electrons (transmitted or scattered) are used to form the image. The first two condenser lenses are used to illuminate the specimen by a parallel beam. The parallel beam strikes the specimen and part of it is transmitted depending on the thickness of the sample and the energy of the electrons striking the sample. The objective lens takes the transmitted electrons from the exit face of the specimen, disperses them to create a diffraction pattern in the back focal plane, and recombines them to form an image in the first image plane, as shown in Fig. 1.13 (b). The image is then passed down the column by the intermediate lens and magnified by the projector lens. Finally, the image strikes the phosphor image screen and light is generated, allowing the user to see the image. The processes mentioned above happen under high vacuum.

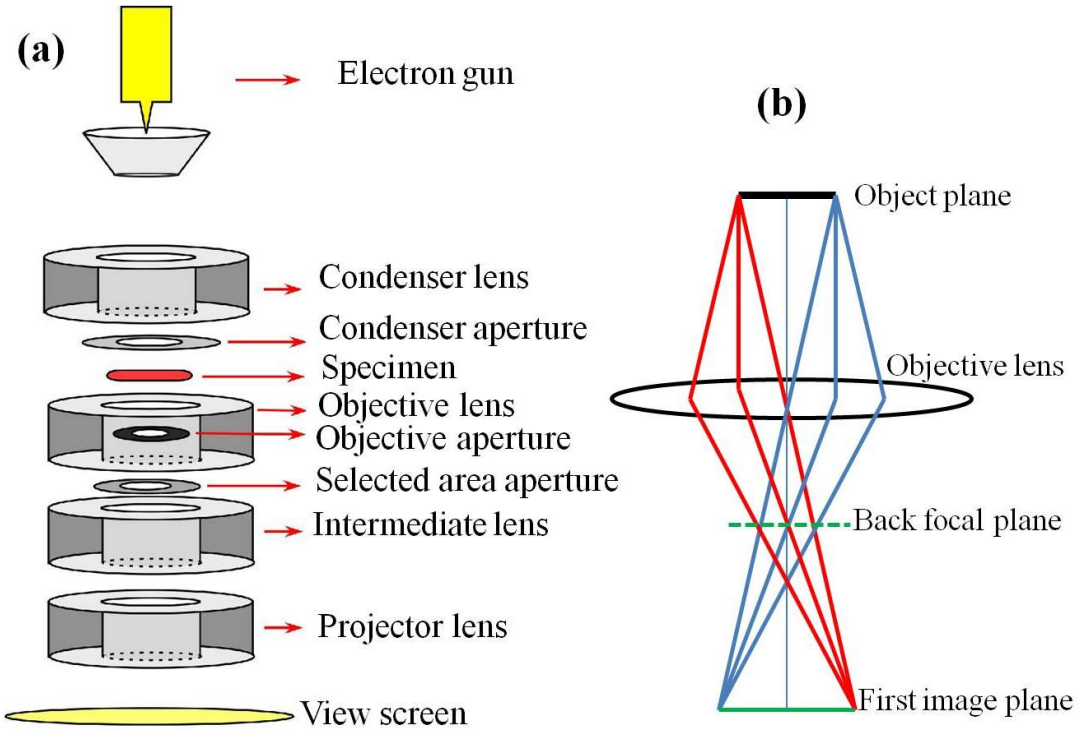


Figure 1.14. (a) Simplified schematic view of a TEM and (b) schematic ray diagram formed by objective lens.

### 1.3.2 TEM operation modes

The main TEM operation modes are: bright field (BF) and dark field (DF) TEM, selected area electron diffraction (SAD), phase-contrast imaging (high resolution TEM (HRTEM)) and energy dispersive X-ray spectroscopy (EDS).

We can form an image either by using the main beam (unscattered) or the scattered electrons. The image formed by the direct beam is called a bright field (BF) TEM image and the image formed by the scattered electrons is called a dark field (DF) TEM image. The choice of which electrons form the image is done by inserting the objective aperture in the back focal plane of the objective lens and tilting the appropriate beam down the centre of the optic axis.

To form a SAD pattern, we choose the area of the specimen by inserting the selected area aperture in the image plane of the objective lens and adjust the strength of the intermediate lens such that the back focal plane of the objective lens acts as the object

plane for the intermediate lens. Therefore, the diffraction pattern formed in the back focal plane will be projected onto the viewing screen. In contrast, to form a BF or DF image, we adjust the intermediate lens such that the image plane of the objective lens acts as the object plane for the intermediate plane. Therefore, the image will be projected onto the viewing screen.

In a HRTEM image the phase of the electron wave carries the information about the sample structure. Electrons entering the crystal which interact with the potential of the crystal will carry a phase shift with respect to the main beam which passes directly through the sample without interaction. The interference of the diffracted and undiffracted electrons generates the contrast in the image. This is true only if the sample is thin enough so that amplitude variations only slightly affect the image intensity.

Characteristic X-rays are emitted when the electron beam removes an inner shell electron from the sample, causing a higher energy electron to fill the hole and release a photon. These photons can be detected by an energy dispersive spectroscopy (EDS) detector to identify the composition and measure the abundance of the various elements in the sample.

Moiré fringes are commonly observed in relaxed heterostructures. Moiré patterns are the result of interference of electrons passing through two sets of lattices with nearly equal periodicy. Two fundamental types of Moiré fringes are translational (two sets with slightly different spacing are translated in a direction perpendicular to the line directions) and rotational (two sets with same spacing are rotated) which are, respectively, parallel and perpendicular to the lines forming them, as shown in Fig. 1.15. In mixed (general) Moiré fringes (Fig. 1.15 (c)) the spacing between the two sets of lattices ($d_1$ and $d_2$) are slightly different and the two sets are rotated with respect to each other by an angle $\beta$. The spacing of general Moiré fringes ($d_{gm}$) can be calculated by [41]:

$$d_{gm} = \frac{d_1 d_2}{\sqrt{(d_1 - d_2)^2 - d_1 d_2 \beta^2}} \tag{1.7}$$

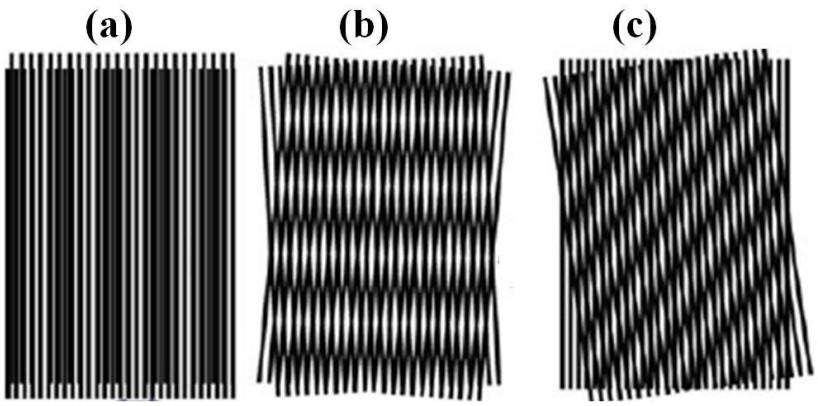


Figure 1.15. (a) Translational, (b) rotational and (c) mixed Moiré fringes [41].

## 2: DEPENDENCE OF NW GROWTH RATE ON DIAMETER

A vapor-liquid-solid (VLS) growth mechanism is the most widely used model to explain the growth of semiconductor nanowires (NWs). Growing the NWs inside a transmission electron microscope (TEM) and observing their evolution during the growth process is the best method to confirm a VLS growth mechanism. However, this method is only possible over limited range of precursor partial pressure and catalyst supersaturation. Analysis of the dependence of NW growth rate on diameter and the precursor partial pressure is an alternative indirect approach to shed light into the VLS growth mechanism. In this method, the consistency of the proposed model with the experimental data can give insight into the steps involved in the VLS growth. This approach has been employed over the past few decades by several groups. In the mid-1970s, Givargizov [42] observed a higher growth rate for thick Si NWs compared to thinner ones and explained it via a thermodynamic model accounting for the elevation of the chemical potential of a nano-scale surface known as the Gibbs-Thomson effect (GTE). Three decades later, a higher growth rate for thick GaAs NWs compared to the thinner ones was reported in the case where the growth temperature was high and NWs were tapered [43]. This behaviour was explained by a kinetic model accounting for the adatoms diffusing from NW sidewalls and substrate surface toward the triple boundary (the line connecting the three phases involved in the VLS growth) [43]. Later, Dubrovskii et al presented a more general model including the GTE and adatom diffusion [44]. In this work, at low group III partial pressure, we observe a lower growth rate for thick GaAs NWs than the thinner ones under a growth condition where the adatom diffusion is negligible and therefore our observed diameter-dependent growth rate behaviour cannot be explained by the mass transport model of Johansson et *al.* [43]. At high group III partial pressures, the thicker NWs grow faster than the thinner ones. In the following we present a model including the GTE and an incubation effect to explain the experimentally observed data. The presence of incubation periods was recently revealed in Si NWs by in situ TEM study of Wen et *al.* [45].

The GaAs NWs studied here were grown using Au nanoparticles (NPs) with sizes ranging from 15 nm to 300 nm at a growth temperature of 400 ˚C. Gold NPs were formed by *ex situ* Au layer deposition (~3 nm) on (111)B GaAs substrates and annealing at 600 ˚C in the MOVPE reactor under $H_2$ and group V overpressure. Trimethylgallium (TMGa) and tertiarybutylarsine (TBAs) were used as the group III and V precursors, respectively. The TBAs flow was set to 130 μmol/min, while the TMGa flow was varied in the range of 2.8 to 42.3 μmol/min. Depending on the group III flow rate, the growth time was varied in the range of 100 s to 400 s to avoid bending of the thin NWs.

## 2.1 Nanowire growth model

Understanding the dependence of NW growth rate on diameter and precursor partial pressure requires the correct identification of the rate limiting step. The model that we consider here is based on an *in situ* study of the growth of Si NWs inside a TEM where it was shown that the Si NW growth proceeds through cyclic processes of stasis (so-called incubation period), nucleus formation and step flow growth of the nucleus at the liquid-solid interface [45]. A schematic of VLS growth of a GaAs NW is shown in Fig. 1.1. At low temperatures where the vapor-solid (VS) growth is negligible and the NW growth is controlled by surface reaction kinetics, VLS growth can be divided into 4 steps: (i) decomposition of the growth precursors in the vicinity of the catalyst NP, (ii) incorporation of the soluble growth species from the vapor phase into the liquid NP, (iii) subsequent elevation of the liquid-solid supersaturation of the NP to a critical value ($\Delta\mu_{ls}^{c} = \mu_l - \mu_s$) and formation of an initial nucleus with a size above a critical value at the alloyed NP/semiconductor interface and (iv) lateral growth of the nucleus by a step flow mechanism to form a complete bilayer of GaAs at the liquid-solid interface. The first step only depends on the growth temperature and is independent of the NW diameter. In addition, we grew all the samples at a single temperature. Therefore, the decomposition step cannot explain the dependence of the growth rate on NW diameters. Many authors have argued for a single growth rate limiting step, such as crystallization at the metal/NW interface or incorporation of cracked growth species into the metal catalyst, based on their growth conditions [42, 46]. In our model, we consider the nucleus formation (step

iii) and the growth of the nucleus to form a complete layer at the NW/NP interface (step iv) separately, unlike the previous studies which ignored the formation of an initial nucleus as a separate step to model the NW growth rate as a function of diameter [47]. We show that, under low group III flux, step (iii) is the rate limiting step which most significantly affects the growth of NWs with large diameters. Under high group III flux, step (iv) plays this role for NWs with small diameters due to the GTE. In our model, both nucleus formation and step flow rate are dependent on the liquid-solid supersaturation. However, in step (iii) the formation of the nucleus will be hindered until the liquid-solid supersaturation reaches a critical value (incubation period), and after the nucleus formation the step flow will immediately start for any positive liquid-solid supersaturation ($\mu_l > \mu_s$).

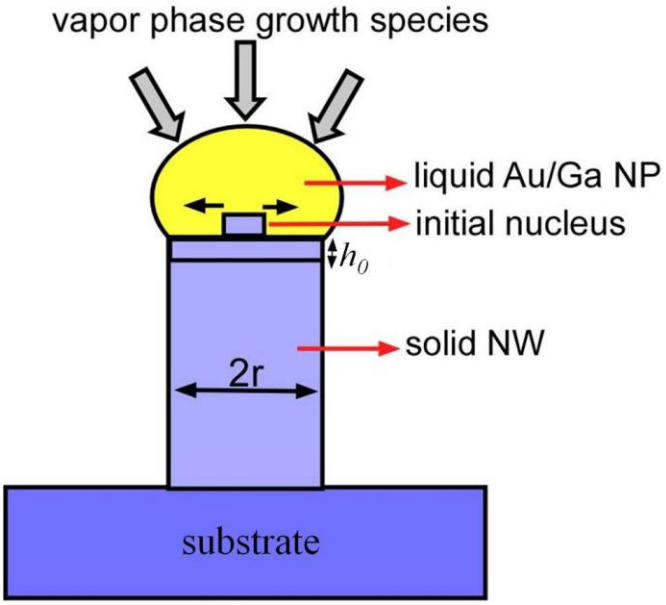


Figure 2.1. (a) Schematic of NW growth via the VLS mechanism.

The time required for the formation of a complete bilayer with height of $h_0$ at the NW/NP interface with radius of $r$ is equal to the sum of the incubation time ($\tau$) and crystallization time ($t_c$). Therefore, the NW growth rate ($v$) can be written as:

$$\frac{1}{v} = \frac{t_c+\tau}{h_0} = \frac{1}{v_c} + \frac{\tau}{h_0} \qquad (2.1)$$

where $v_c$ is the crystallization rate at the NP/NW interface given by [48]:

$$v_c = Ac_0(e^{\frac{\Delta\mu_{ls}}{k_BT}} - 1) \quad (2.2a)$$

where

$$A = f\Omega^{\frac{4}{3}}e^{-\frac{E_{desol}}{k_BT}} \quad (2.2b)$$

where $\Omega$ is the molar volume of the solute growth species and $E_{desol}$ is the energy required for the growth species dissolved in the NP to leave the solution and then crystallize at the NP/NW interface. $f$ is the crystallization attempt frequency of the growth species dissolved in the liquid NP. The rate at which growth species overcome $E_{desol}$ is given by $fe^{-\frac{E_{desol}}{k_BT}}$. $\Delta\mu_{ls} = \mu_l - \mu_s$ is the difference between the liquid and solid phase chemical potentials known as the supersaturation given by [48]:

$$\Delta\mu_{ls} = k_BTln(\frac{c}{c_0}) \quad (2.3)$$

where $c$ and $c_0$ are the instantaneous and equilibrium concentrations of the soluble growth species in the liquid phase. Combining Eq. 2.2(a) and 2.3, $v_c$ can be written in a simpler form:

$$v_c = A(c - c_0) \quad (2.4)$$

During the NW growth, crystallization depletes the growth species from the NP, while the impingement of the growth species from the vapor phase on the NP surface increases the concentration.

### 2.1.1 Incubation effect

Based on *in situ* TEM observations, Wen et *al.* [45] showed that the Au-catalyzed Si NW growth process includes incubation periods where during this time there is no solid phase growth. During the incubation period the NW growth ceases, while the concentration of the soluble growth species in the alloyed NP increases above the equilibrium value ($c_0$). This results in an increase in the chemical potential of the growth species in the NP according to $\mu_l = \mu_l^0 + k_BTln(\frac{c}{c_0})$, where $\mu_l^0$ is the equilibrium chemical potential of the NP which is also equal to the solid phase chemical potential ($\mu_l^0 = \mu_s$). Wen et al. pointed out that before step nucleation occurs, the chemical potential of the NP has to reach a characteristic value corresponding to a characteristic Si (in our case Ga) concentration ($c_c$) in the NP. The time taken for the NP to reach $c_c$ is called the

incubation time ($\tau$). The origin of the barrier for initial nucleus formation in NWs has not yet been discussed in the literature. One possible explanation of the nucleation barrier during the incubation period is as follows. During the nucleus formation, the growth species in the liquid phase with chemical potential of $\mu_l$ transfers to the solid phase with chemical potential $\mu_s$. Since $\mu_l > \mu_s$, the volume formation of the nucleus will lower the Gibbs free energy (at a constant pressure and temperature). Therefore, the change in Gibbs free energy due to the volume formation ($\Delta G_{vol}$) is negative. In addition, the formation of the nucleus results in a new surface at the edges of the nucleus which increases the Gibbs free energy of the system. Therefore, the change in Gibbs free energy due to surface formation at the edges ($\Delta G_{surf}$) of the nucleus is positive. The total change in Gibbs free energy ($\Delta G$) is:

$$\Delta G = \Delta G_{Vol} + \Delta G_{surf} = \frac{\pi r_n^2 h_0}{\Omega_{Ga-As}}(\mu_s - \mu_l) + 2\pi r_n h_0 \gamma_{ls} \quad (2.5)$$

where $r_n$ and $h_0$ are the radius and height of the nucleus and $\gamma_{ls}$ is the surface energy of the nucleus sides. The total change in Gibbs free energy and the change due to the volume and surface formation of a GaAs nucleus as a function of nucleus size are plotted in Fig. 2.2. To generate this graph, we used $\gamma_{ls}$ = 0.9 J/m$^2$ [49] and $h_0$ equal to the inter-plane spacing of GaAs NW along the [111] direction and $\Omega_{Ga\text{-}As}$ = 27.3 cm$^3$/mole. To calculate the change in chemical potential, as an example, we assumed the concentration of Ga in the alloyed NP to be twice the equilibrium concentration ($c = 2c_0$). From Fig. 2.2, it is clear that $\Delta G$ has a maximum known as the nucleation barrier ($\Delta G_b = \frac{\pi h_0 \Omega \sigma_{ls}^2}{\Delta \mu_{ls}}$) at $r_n^* \sim 7$ nm. Therefore, the chemical potential of the NP should be high enough to overcome this nucleation barrier to form the initial nucleus at the NW/NP interface.

Considering the steady increase of the Ga concentration of a NP to a critical value ($c_c$) due to the absorption of the growth species from vapor phase (ignoring the change of the radius of the NP during the incubation time), one can derive a relation between incubation time ($\tau$), the impingement rate of growth species from vapor phase on the NP surface per unit area ($j$) and the NP radius ($r$) for one cycle of the incubation time as:

$$2\pi r^2 j\alpha = \frac{2}{3}\pi r^3 \frac{dc}{dt} \quad (2.6a)$$

which gives

$$c = \frac{3j\alpha}{r}t + c_0 \tag{2.6b}$$

and therefore the incubation time is given by

$$\tau = \frac{r\Delta c_c}{3\alpha j} \quad . \tag{2.6c}$$

where $\Delta c_c = c_c - c_0$ and $\alpha$ is the fraction of precursor molecules which diffuse through the boundary layer and decompose in the vicinity of the NP and incorporate into the NP.

Treating the vapor phase as an ideal gas, which is a good approximation at low pressures, the velocity distribution ($P(v)$) of the precursor molecules follows the Maxwell distribution:

$$P(v)dv = (\frac{m}{2\pi k_\beta T})^{3/2} e^{-\frac{mv^2}{2k_\beta T}} dv \tag{2.7}$$

where $m$ and $v$ = ($v_x$, $v_y$, $v_z$) are the molecular mass and velocity of the gas phase molecule, respectively, and $T$ is temperature. $J$ can be calculated by [48]:

$$j = \int_{-\infty}^{+\infty} dv_x \int_{-\infty}^{+\infty} dv_y \int_0^{+\infty} dv_z |v_z| P(v) = \frac{P}{\sqrt{2\pi m k_\beta T}} \tag{2.8}$$

where $P$ is the input partial pressure of TMGa.

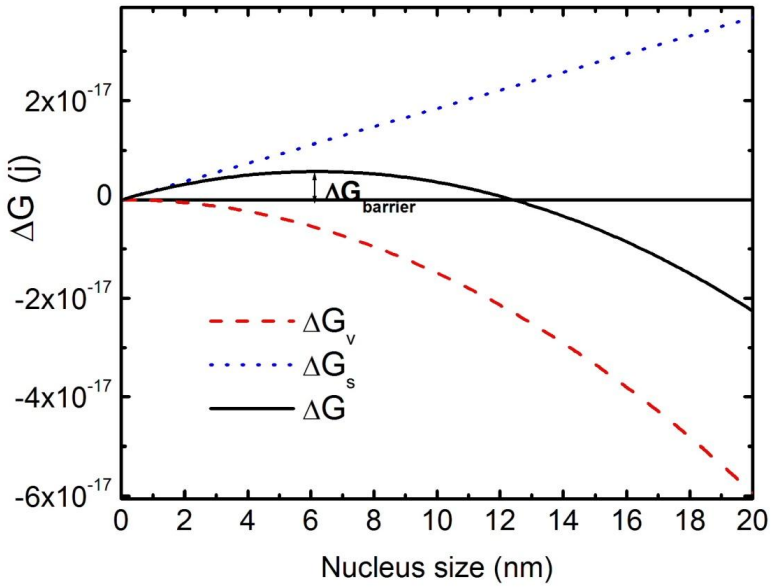


Figure 2.2. Plot of the change in Gibbs free energy ($\Delta G$) as a function of nucleus size. State step energy used in fig caption.

### 2.1.2 Gibbs Thomson effect

It's known that the size reduction of a droplet results in an increase of the chemical potential of the droplet due to the contribution of the surface energy in the Gibbs free energy [50] and this is known as the Gibbs-Thomson effect (GTE). The GTE can be relevant to NW growth because the incorporation rate from the vapor (liquid) phase to the liquid (solid) phase depends on the supersaturation $\Delta\mu_{vl} = \mu_v - \mu_l$ ($\Delta\mu_{ls} = \mu_l - \mu_s$) ($\mu_v$, $\mu_l$ and $\mu_s$ are the chemical potentials of the vapor, liquid and solid phases, respectively). The role of the GTE on the growth rate of the NWs has been discussed by many authors [42, 43, 47]. Johansson et *al*. [43] pointed out that the Gibbs-Thomson effect does not affect the incorporation of the growth species from the vapor phase into the liquid phase NP for GaAs NWs grown under typical growth conditions used in the MOVPE technique. Including the GTE, the effective impingement rate of growth species on the NP surface per unit area is [43, 51]:

$$j = \frac{P - P_0 e^{\frac{2\sigma_{lv}\Omega_{Ga}}{rk_\beta T}}}{\sqrt{2\pi m k_\beta T}} \tag{2.9}$$

where $P_0$ is the equilibrium partial pressure of vapor and liquid Ga with infinite size and can be calculated using the Clausius-Clapeyron equation [52]:

$$\ln\left(\frac{P*}{P_0}\right) = \frac{H_{vap}}{R}\left(\frac{1}{T_0} - \frac{1}{T*}\right) \tag{2.10}$$

where $P$* and $T$* are the reference pressure and temperature, equal to $9.3 \times 10^{-36}$ Pa and 302.9 K for Ga vapour respectively. $H_{vap}$ and $R$ are the enthalpy of vaporization (258.7 KJ/mole) and gas constant (8.31 $J.mole^{-1}.K^{-1}$), respectively. Considering the GTE effect in Eq. 2.9 for a NP with radius of 5 nm, the second term is $4.6 \times 10^{-10}$ Pa. This value is 9 orders of magnitude smaller than the smallest TMGa input partial pressure used in this work. Therefore, we ignore the GTE in the incorporation of Ga from vapor to liquid phase. The low solubility of As in Au implies that As mainly incorporates into GaAs NW via diffusion through the Au NP/NW interface. Therefore, the GTE does not play a significant role in the incorporation of As into GaAs NWs.

The solubility limit or equilibrium concentration ($c_0$) of Ga in Au/Ga alloy with infinite size ($c_\infty$) at 400 ˚C is about 38 atomic percent Ga. This value increases with size reduction according to [53, 54]:

$$c_0 = c_\infty e^{\frac{2\sigma_{ls}\Omega}{rk_\beta T}} \quad (2.11)$$

where $c_\infty$, $\sigma_{ls}$, $\Omega$ and $r$ are, respectively, the equilibrium concentration of the soluble growth species in an infinitely large particle, the surface energy of the liquid-solid interface, the molar volume of Ga, and the radius of the NP. Based on *in situ* TEM measurements, for the case of Ge NWs grown from Au NPs, Dayeh et *al*. [53], showed that the equilibrium Ge concentration in the Au NP ($c_0$) increases with decreasing diameter according Eq. 2.11. Combining Eq. 2.11 and 2.3, the liquid-solid supersaturation, including the GTE, can be written as:

$$\Delta\mu_{ls} = \Delta\mu_{ls}^{\infty} - \frac{2\sigma_{ls}\Omega_{Ga}}{rk_\beta T} \quad (2.12)$$

where $\Delta\mu_{ls}^{\infty} = k_\beta T ln(\frac{c}{c_\infty})$ is the difference in the chemical potentials of liquid and solid phases with infinite sizes. Therefore, the GTE is in operation in the crystallization step which is driven by liquid-solid supersaturation.

Combining Eq. 2.2a and 2.12 or Eq. 2.4 and 2.11, the crystallization rate, including the GTE, can be written as:

$$v_c = A\left(c - c_\infty e^{\frac{2\sigma_{ls}\Omega_{Ga}}{rk_\beta T}}\right) \approx A(c - c_\infty) - \left(\frac{2A\sigma_{ls}\Omega_{Ga}c_\infty}{k_\beta T}\right)\frac{1}{r} = v_c^{\infty} - \frac{\omega}{r} \quad (2.12a)$$

where

$$v_c^{\infty} = A(c - c_\infty) \quad (2.12b)$$

is the crystallization rate on an infinite surface and $\omega$ is:

$$\omega = \frac{2A\sigma_{ls}\Omega_{Ga}c_\infty}{k_\beta T}. \quad (2.12c)$$

In Eq. 2.12(a), the exponent is equal to ~0.2 for $r$ = 20 nm which justifies the final equation in Eq. 2.12(a). Substituting Eq. 2.6(c) and 2.12 in Eq. 2.1, the NW growth rate can be written as:

$$v = (\frac{1}{\left(v_c^{\infty} - \frac{\omega}{r}\right)} + \varphi r)^{-1} \quad (2.14a)$$

where

$$\varphi = \frac{\Delta c_c}{3h_0\alpha j}\,. \quad (2.14b)$$

The three parameters in Eq. (2.14a) ($v_c^{\infty}$, $\omega$ and $\varphi$) are treated as fitting parameters in the following analysis. Equation (2.14a) indicates that for high values of $j$, where the incubation time is small, the growth rate tends to a fixed value for NWs with large radius and drops for NWs with smaller radius due to the GTE. In the case of a low value of $j$, the second term dominates, resulting in a lower growth rate for NWs with larger radius.

## 2.2 Experimental results: Comparison to model

An SEM image of Au NPs prior to NW growth is shown in Fig. 2.3(a) indicating a large size dispersion (15-300 nm). Representative SEM images of the GaAs NWs grown using 2.28, 0.76 and 0.15 Pa TMGa input partial pressures are shown in Fig. 2.3(b), (c) and (d), respectively. It's clear that the thinner NWs grow more slowly than the thicker ones in the highest TMGa partial pressure (Fig. 2.3(b)). For intermediate TMGa partial pressure (Fig. 2.3(c)), there is much less dispersion in the length of the NWs. NWs grown with the lowest TMGa partial pressure (Fig. 2.3(d)) show a lower growth rate for the thicker ones.

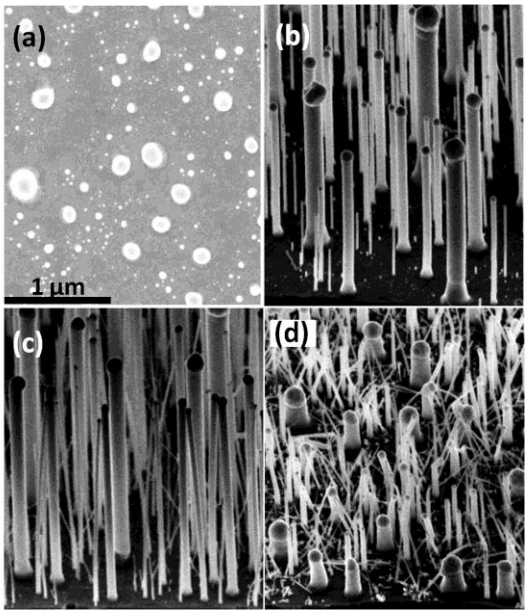


Figure 2.3. (a) Plan-view SEM image of the Au NPs prior to NW growth and 45˚ SEM images of GaAs NWs grown with TMGa input partial pressure of (b) 2.28 Pa for 100 s, (c) 0.76 Pa for 300 s and (d) 0.15 Pa for 400 s.

The results of statistical analyses of the SEM images of the NWs grown using different TMGa partial pressures are shown in Fig. 2.4. At high TMGa partial pressures (> 0.76 Pa), the growth rate is limited by the step flow growth rate which is lower for thinner NWs due to the GTE (step iii). The growth rate of the NWs increases with increasing diameter up to 70 nm and a diameter-independent growth rate was observed for larger NPs. A decrease in the TMGa partial pressure results in a decrease in the overall growth rate of the NWs as expected due to a decrease in the attachment rate of the growth species to the NP surface. In addition, a decrease of the TMGa partial pressure hinders the growth of the thicker NWs. At low TMGa partial pressures, the growth rate is limited by the incubation time due to low incorporation rate from the vapor phase into the liquid NP (step ii) which hinders the formation of the initial nucleus. The fits to the experimental data, shown in Fig. 2.4 by solid lines, indicate an excellent agreement with Eq. (2.14a).

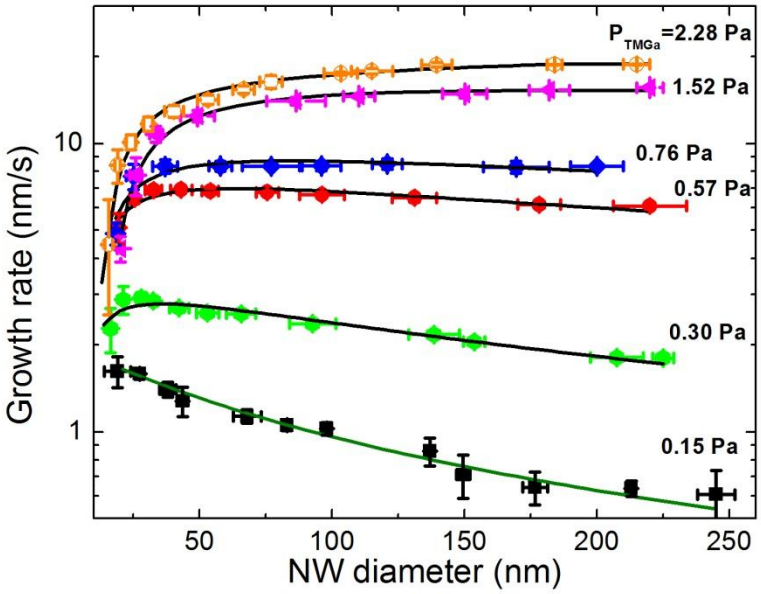


Figure 2.4. Plot of the growth rate of the GaAs NWs vs. their tip diameter for different TMGa input partial pressures.

In Fig. 2.5, the fitting parameters ($v_c^{\infty}$, $\omega$ and $\varphi$) in Eq. (2.14a) are plotted as a function of impingement rate of growth species per unit area of the NP ($j$). The crystallization rate in the absence of the GTE and incubation period, $v_c^{\infty}$ increases linearly with $j$ for $j > 1.5 \times 10^{22}$ atoms.m$^{-2}$s$^{-1}$. According to Eq. 2.4, this indicates an increase in the instantaneous concentration of Ga atoms dissolved in the NP with increasing flow rate of TMGa which subsequently, according to Eq. 2.3, enhances the liquid-solid supersaturation. In addition, the kinetic pre-factor in Eq. 2.4 might also increase with increasing Ga concentration which will be discussed later. For $j > 1.5 \times 10^{22}$ atoms.m$^{-2}$s$^{-1}$, $v_c^{\infty}$ starts to saturate. This suggests the presence of an upper limit for the concentration of Ga in the alloyed NP. For high values of $j$, the absorption sites on the NP surface may saturate and therefore a further increase of the TMGa partial pressure does not enhance the incorporation rate of the growth species from vapor phase into the liquid NP (step ii). This results in the saturation of the crystallization rate.

The incubation parameter ($\varphi$) is plotted in Fig. 2.5(b), and shows an inverse relation with $j$. The best fit to the results in Fig. 2.5(b) was obtained by $\varphi \propto \frac{1}{j^{1.25\pm0.15}}$ which is in agreement with our prediction in Eq. (2.14b).

Fig 2.5(c) shows fitting values obtained for $\omega = \frac{2\sigma_{ls}\Omega_{Ga}c_{\infty}f\Omega^{\frac{4}{3}}}{k_{\beta}T}e^{-\frac{E_{desol}}{k_{\beta}T}}$ as a function of $j$. $\omega$ increases with increasing $j$ up to $1.5 \times 10^{22}$ atoms.m$^{-2}$s$^{-1}$ and saturates for higher $j$. The bond dissociation energy ($E_{desol}$) is the only factor that can significantly affect $\omega$. The bond dissociation energy of Ga-Ga (<106.4 KJ/mole) is much lower than Au-Ga bond (290 KJ/mole). Increasing $j$ increases the Ga concentration in the alloyed NP which makes the Ga-Ga bonding more likely. Therefore, increasing the Ga concentration in the alloyed NP will increase the exponential factor $e^{-\frac{E_{desol}}{k_{\beta}T}}$ resulting in an increase in $\omega$. The saturation of $\omega$ for $j > 1.5 \times 10^{22}$ atoms.m$^{-2}$s$^{-1}$ might be due to the presence of an upper limit for the concentration of Ga in the alloyed NP as discussed earlier.

Finally, we should note that only a small fraction ($\alpha$) of the input precursor flux successfully diffuses through the gas phase boundary layer and reaches the NP surface and incorporates into the NP. An estimate of $\alpha$ can be obtained as follows. In the absence of any growth rate limiting step, where the number of incorporated atoms per unit time from vapor phase into the liquid NP ($2\pi r^2 j\alpha$) is equal to the number of atoms transferred from the liquid to solid phase ($\frac{\pi r^2 v_c^{\infty}}{\Omega_{GaAs}}$), $v_c^{\infty}$ can be calculated by [51]:

$$v_c^{\infty} = 2\Omega_{GaAs}\alpha j \tag{2.15}$$

Equation (2.15) predicts a linear increase of $v_c^{\infty}$ with increasing $j$ consistent with our results in Fig. 2.5(a). Fitting the linear region of the results shown in Fig. 2.5(a) to Eq. (2.15) gave $\alpha = 0.016 \pm 0.003$.

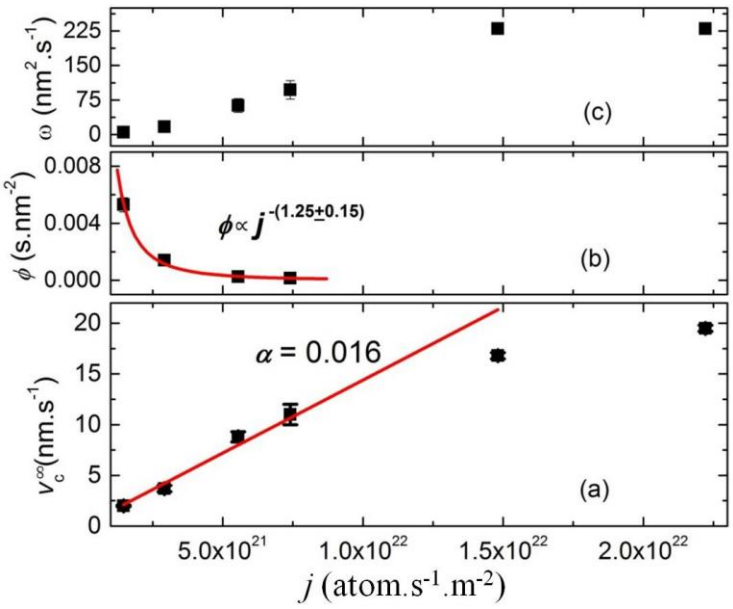


Figure 2.5. Plot of the fitting parameters in Eq. (2.14a), (a) $v_c^{\infty}$, (b) $\varphi$ and (c) $\omega$ as a function of impingement rate per unit area ($j$).

In summary, we presented a model for diameter-dependent growth rate behaviour of MOVPE-grown GaAs NWs by taking into account the Gibbs-Thomson and incubation effects. We showed that, at low TMGa partial pressures, the growth rate decreases for larger NWs due to the incubation period required for initial nucleus formation at the liquid-solid interface. At high TMGa partial pressures, the NP can reach the required supersaturation for nucleus formation quickly and the growth rate limiting step is the step flow growth of the nucleus, which is lower for narrow NWs due to the Gibbs-Thomson effect.

## 3: EFFECT OF GROUP III PRECURSOR CHEMISTRY ON THE MORPHOLOGY OF GAAS NANOWIRES

Investigation of the basic aspects of nanowire (NW) growth such as lateral vs. axial growth is essential for the fabrication of the devices based on core/shell NWs. The lateral size of the NWs grown via the vapor-liquid-solid (VLS) mechanism is usually restricted to the size of the nanoparticles (NP) used at the tip of the NWs. However, increased growth temperature can enhance lateral growth leading to tapered NWs with the base diameter much larger than the NP size at the tip of the NW [8]. There have been very few prior works on the role of precursor chemistry in controlling the growth characteristics of VLS-grown NWs. Most prior works on the growth of GaAs NWs by MOVPE have used trimethylgallium (TMGa) and tertiarybutylarsine/arsine (TBAs/$AsH_3$) as the group III and V precursors, respectively. However, the use of alternate precursors such as triethylgallium (TEGa) for the growth of GaAs NWs has been reported on very rare occasions only in $N_2$ ambient [55]. As mentioned in the previous chapter, TEGa has a much lower decomposition temperature than TMGa, which can significantly alter the reaction kinetics of NW growth. As a result, in thin GaAs films, gas phase diffusion limited growth is observed at much lower temperatures with TEGa than TMGa, and this should have important implications for NW growth.

In this chapter, we investigate the temperature dependence of the growth of GaAs NWs using TEGa and TBAs in $H_2$ ambient and compare it to the GaAs NWs grown using TMGa. We explore the kinetics of axial and planar growth using the two precursors, and show how the growth of axial and core shell heterostructures can be directly controlled by precursor chemistry. The work presented in this chapter forms the basis of a paper published in Journal of Crystal Growth [56].

To grow the GaAs NWs studied in this chapter, a 0.2 nm gold layer deposited on a (111)B GaAs substrate was annealed at 650 °C resulting in NPs with a fairly uniform size of 31 ± 6 nm. The growth temperature was in the range of 370 to 485 °C. TMGa and TEGa with a flow rate of 15 μmol/min were used as the group III precursors, and TBAs

with a flow of 63 μmol/min was used as group V precursor. The growth time was fixed at 100 sec unless otherwise mentioned. Temperature readings were calibrated by placing a thermocouple in contact with the top surface of the susceptor over the range of measurement temperatures. The use of an optical pyrometer for temperature control limited the minimum reliable growth temperature to 370 °C. In InAs/GaAs axial and radial heterostructures, the InAs segment was grown at 400 ˚C TMIn (flow rate of 10 μmol/min) and TBAs (flow rate of 63 μmol/min) as group III and V precursors, respectively. TMGa and TEGa (flow rate of 15 μmol/min) were used to grow axial and radial heterostructures, respectively, without changing the growth temperature.

High resolution x-ray diffraction (XRD) measurements were carried out to determine the thickness of the planar GaAs films grown on (001) GaAs substrates using a thin (~0.3 nm) InAs marker layer between the GaAs substrate and epilayer. In the case where the surface of the epilayer is rough (e.g. for epilayers grown on (111)B substrates), there is no constructive interference and consequently no thickness fringes are evident. The results of ref. [57] indicate relatively small differences in the growth rates for different substrate orientations below 550 °C, therefore we assumed that the (001) planar growth rates give a reasonable estimate of the growth rates on (111)B.

## 3.1 Kinetics of thin GaAs film growth using TMGs vs. TEGa

Figure 3.1 shows a comparison of the growth rates of planar GaAs films on (001) GaAs substrates grown using TMGa and TEGa as group III precursors in the absence of Au NPs. Nominally identical molar flows were used for both precursors. Both precursors show a similar growth rate of ~ 0.45 nm/s at 500°C where the growth rate is limited by gas phase diffusion. The growth rate of the TMGa-grown GaAs films decreases exponentially with growth temperature below 500 °C due to surface reaction kinetics with an activation energy of 135 ± 6 kJ/mol. In contrast the TEGa growth rate remains constant down to 420 °C, below which it decreases rapidly with temperature. As previously discussed, due to experimental limitations, growth rates below 370 °C were not accessible. Therefore we can only estimate an approximate value of ~102 kJ/mol for the activation energy of the TEGa growth rate based on the lowest two temperature

measurements in Fig. 3.1. Note that the growth rate of the TEGa-grown GaAs films is more than an order of magnitude higher than for TMGa at temperatures below 420 °C.

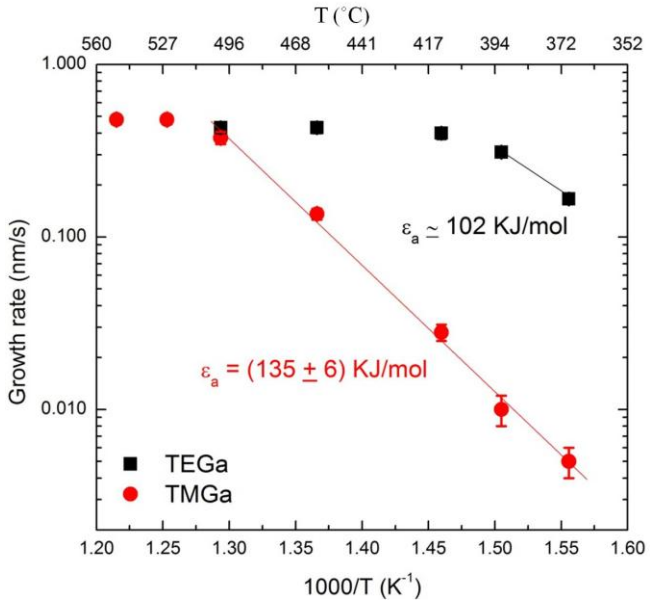


Figure 3.1. Plot of the growth rate vs. 1000/T of the GaAs planar film grown on (001) GaAs substrates using TEGa and TMGa.

## 3.2 GaAs nanowire growth using TMGa vs. TEGa

To investigate the growth of GaAs NWs using TMGa/TEGa, we fabricated GaAs NWs in the temperature range of 370 ºC to 485 ºC for 100 sec on (111)B GaAs substrates using a uniform distribution of Au NPs with an average diameter of 31nm, with a standard deviation of ±6 nm, and a surface density of $7\times10^9$ $cm^{-2}$, shown in Fig. 3.2(g). Figure 3.2 shows representative examples of SEM images of the NWs grown using TMGa and TEGa at 370, 410 and 485 °C.

For the case of TMGa (Fig. 3.2(a)-(c)), the NW growth rate increases with increasing temperature up to 420 ºC, and then decreases at higher temperatures. NWs grown at the lowest temperature exhibit negligible tapering (Fig. 3.2(a)), while higher temperature growth results in some tapering (Fig. 3.2(c)), coincident with the reduction of the axial growth rate. These results are qualitatively similar to those of other groups

who argued that this behavior is the result of competition between VLS and vapor-solid (VS) growth [8]. At low temperature, lateral growth is inhibited because VS growth is kinetically suppressed for TMGa growth (Fig. 3.1), while at high temperatures, lateral growth becomes significant.

In contrast, the axial growth rate of the TEGa-grown NWs decreases continuously with increasing temperature (Fig. 3.2(d)-(f)), while the base diameter of the NWs increases due to lateral growth, resulting in tapered NWs. Tapering of the TEGa-grown NWs is clearly evident even at temperatures as low as 410 °C (Fig. 3.2(e)) because of the more efficient decomposition of TEGa at low temperatures compared to TMGa (Fig. 3.1).

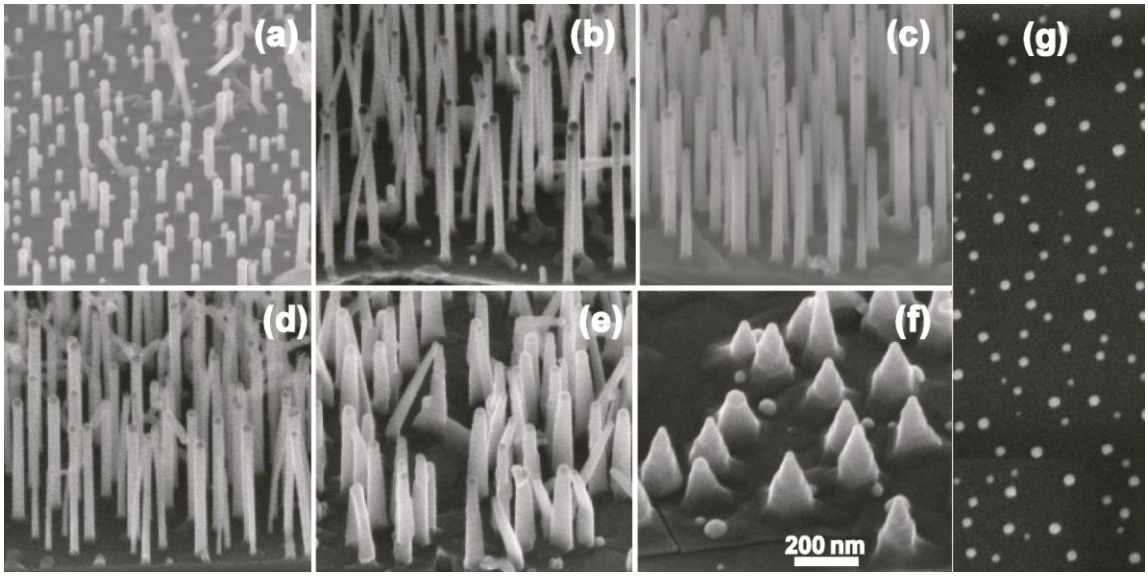


Figure 3.2. (a-f) 45° tilt angle SEM images of GaAs NWs grown on (111)B GaAs substrates for 100 sec using TMGa at (a) 370 ˚C, (b) 410 ˚C and c) 485 ˚C and using TEGa at (d) 370 ˚C, (e) 410 ˚C and (f) 485 ˚C. Plan-view SEM image of the Au NPs ($t_{Au}$ = 0.2 nm and $T_{anneal}$ = 650 °C) before growth is shown in (g).

The measured axial and lateral growth rates of the TMGa- and TEGa grown NWs vs. 1000/*T* are shown in Fig. 3.3. The lateral growth rate was based on measurements of half of the average difference between the NW base and tip diameters. Two distinct

regions are observed for the growth of TMGa-grown NWs. In the low temperature regime (T<440 °C), the axial growth of the TMGa-NWs is thermally activated with negligible lateral growth. The activation energy of the axial growth rate was 59 ± 7 KJ/mol, which is significantly below the activation energy that we measured for the planar (001) GaAs films (135 ± 6 kJ/mol). This clearly indicates that Au nanoparticles are acting as catalysts during the growth. In some cases, other groups have reported little difference between activation energies for NW and planar growth rates, however unlike the present work, the measurements were not generally reported for the same growth apparatus [58].

In the high temperature regime (T > 440 °C), direct VS growth on the NW sidewalls and substrate surface starts to compete with VLS growth due to the increasing decomposition of TMGa evident in Fig. 3.1. Lateral growth on the NW sidewalls increases strongly with growth temperature resulting in tapered NWs. The observed activation energy for the lateral growth rate is 127±18 kJ/mol, which is in agreement with the value of 135±6 kJ/mol observed for planar growth on (001) GaAs substrates using TMGa (Fig. 3.1). At the same time the axial growth rate decreases with increasing temperature due to increasing competition from VS growth. The lateral growth rate reaches 0.1 nm/s at 485 °C compared with 0.4 nm/s for planar growth on (001) GaAs substrates. This is due to the fact that most of the TMGa flux is still intercepted by VLS growth even at the highest temperature indicated.

For TEGa growth, Fig. 3.3 shows that there is no temperature regime where the axial growth rate is thermally activated. This is consistent with the much lower decomposition temperature for TEGa vs. TMGa. Limitations of the growth apparatus prevented us from growing NWs below 370 °C where we would expect to observe an exponential decrease in the axial growth rate. Fig. 3.3 confirms the much higher level of lateral growth of TEGa-grown NWs compared with TMGa-grown NWs, even at the lowest growth temperatures. Again we see a decrease in the axial growth rate with increasing temperature, which occurs concurrently with a strong increase in lateral growth. The lateral growth rate shows an activation energy of 96±6 kJ/mol which is comparable to the very rough estimate of 102 kJ/mol for planar growth with TEGa on (001) GaAs substrates (Fig. 3.1). At high temperatures (> 440 °C), the lateral growth rate

approaches the value found for planar growth on (001) GaAs substrates at the highest temperatures (Fig. 3.1). In addition we see that the lateral growth rate is much higher for TEGa than TMGa.

Table 3.1 shows a summary of the activation energies measured from this study. The final column shows the ratio between TMGa and TEGa activation energies for planar growth and lateral NW growth measurements. The value of 1.3 is in reasonable agreement with the ratio of decomposition energies of TMGa and TEGa inferred from various gas phase decomposition studies on (001) GaAs [59, 60].

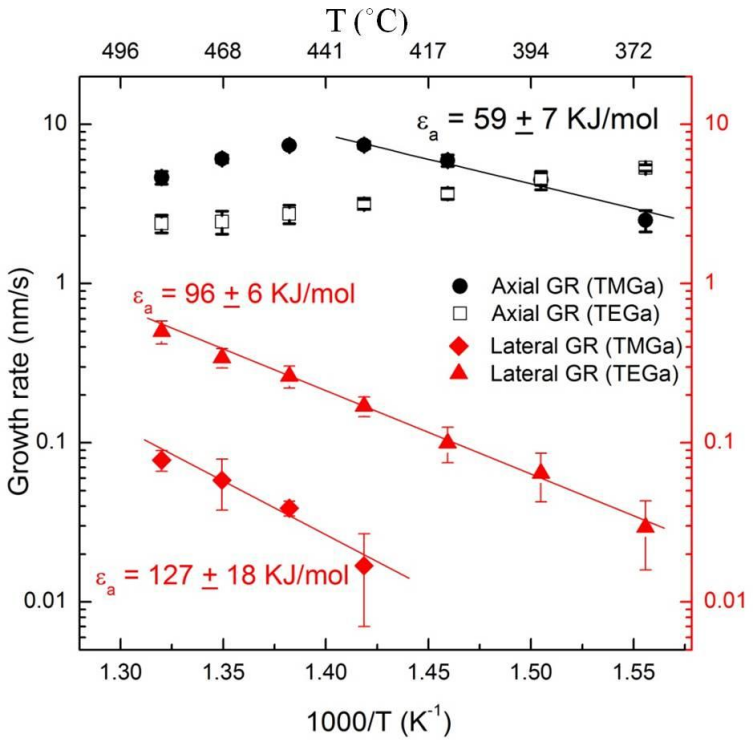


Figure 3.3. Plot of the axial growth rate and lateral growth rate vs. 1000/T of the TEGa- and TMGa-grown GaAs NWs grown on (111)B GaAs substrates.

Table 3.1. Activation energies for Au-free layers on GaAs (001), and for axial and lateral growth rates of NWs using different Ga precursors.* Au-free TEGa data is based on two data points and error limits are therefore not quoted.

| | TMGa | TEGa | Ratio TMGa/TEGa |
|---|---|---|---|
| $E_a$ (Au-free (001) planar) (kJ/mol) | 135 ± 6 | ~102 * | 1.32 |
| $E_a$ (axial NW growth) (kJ/mol) | 59 ± 7 | n/a | n/a |
| $E_a$ (lateral NW growth) (kJ/mol) | 127 ± 18 | 96±6 | 1.32 |

## 3.3 Comparison of the kinetics of thin film and nanowire growth

For a better comparison between thin film growth without Au NPs and NW growth, we should compare the thin film growth rate with the total equivalent planar growth rate of the NW sample. The total equivalent planar growth rate represents the planar growth rate that would be obtained if all the mass growth including axial (VLS), planar and lateral NW growth (VS) were incorporated in a planar layer, as shown schematically in Fig. 3.4. In the following, for simplicity, we assumed that the lateral growth at the base of the NW also applies to the planar growth on the (111)B substrate. The planar equivalent growth rate of the axial growth is equal to the average axial growth rate multiplied by the surface fraction coverage of the NPs. The planar equivalent growth rate of the lateral growth is equal to the lateral growth rate of a shell with thickness of $t/2$ (Fig 3.4(b)) multiplied by the ratio of the NW surface area ($2\pi rL$) and cross sectional area of the core ($\pi r^2$) then multiplied by the NP surface fraction coverage.

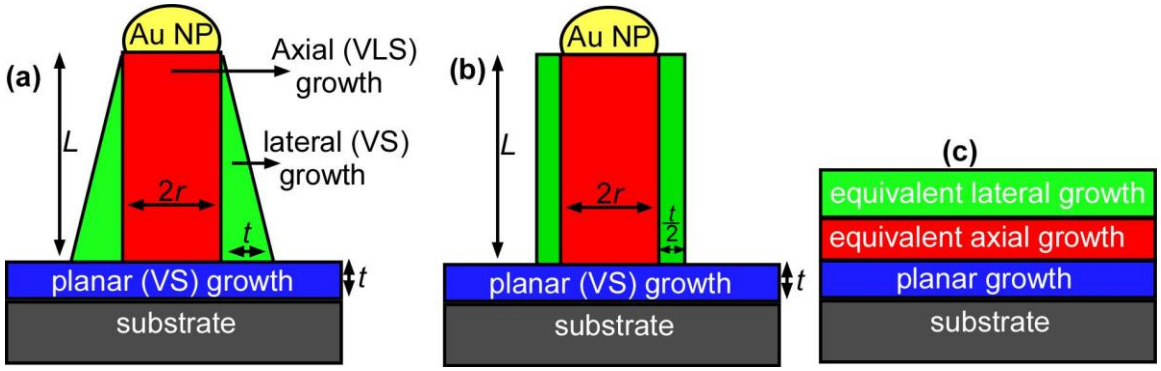


Figure 3.4. (a) Schematic of the growth modes involved in the growth of a NW with length of $L$ and shell thickness of $t$ at the base of the NW, (b) modelling the shell in (a) with a uniform shell with thickness of $t/2$ and (c) corresponding equivalent volume growth of each mode.

In Fig. 3.5 we plot the planar equivalent of axial growth rate (circular symbols) for the NWs grown using TMGa, which is equal to the average axial growth rate multiplied by the surface fraction coverage of the NPs. Also shown (square symbols) is the lateral growth rate for TMGa-grown NWs from Fig. 3.3. Next, we plot the sum of the total planar equivalent growth rate (open triangle symbols). For temperatures above 420 °C this is roughly constant at 0.4 nm/s and agrees approximately with the diffusion limited growth rate observed for TMGa above 500 °C, and for TEGa above 420 °C. The presence of gold NPs has shifted the plateau for gas phase diffusion-limited growth to approximately 420 °C, a reduction of approximately 80 °C. This clearly confirms the catalytic effect of the Au nanoparticles. For temperatures below 420 °C we see the onset of thermal activation of NW axial growth. At higher temperatures, the surface reaction rate for lateral growth becomes larger, resulting in increased competition for the incoming Ga flux. As a result the axial growth rate saturates.

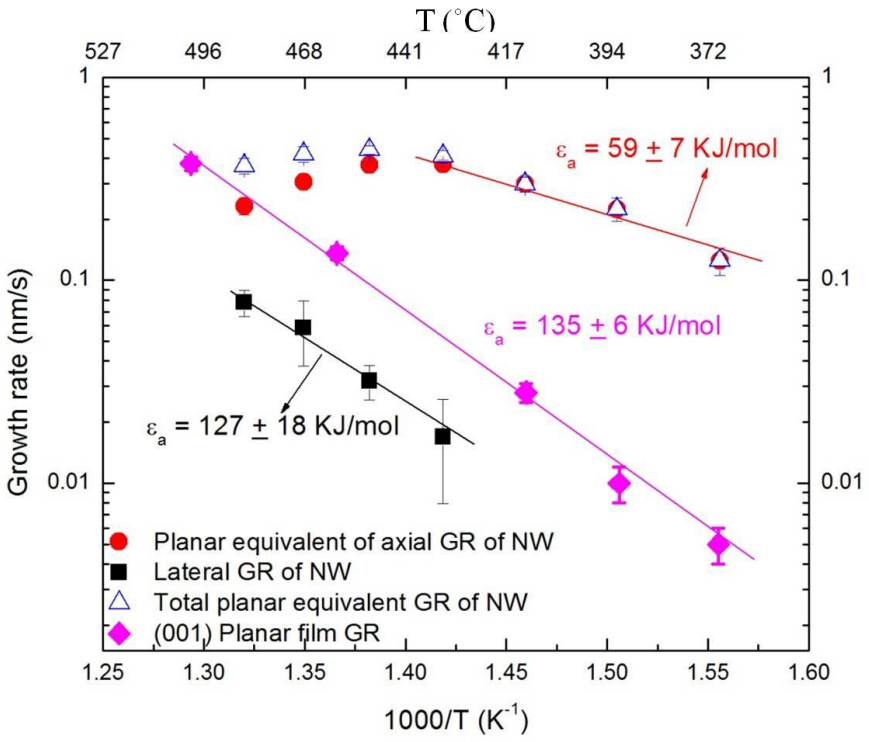


Figure 3.5. Temperature dependence of the NW effective planar growth rates and measured lateral growth rates compared to planar growth on a 001 Au-free planar (100) GaAs substrates. All data were obtained using TMGa.

For TEGa (Fig. 3.6), the data show similar trends, however shifted to much lower temperature. The effective planar growth rate contribution from axial growth decreases continuously with increasing temperature, accompanied by a corresponding increase of the lateral growth rate. As mentioned before, since the decomposition temperature of TEGa is so low we do not actually see a clear thermally activated axial growth rate within the range of temperatures accessible to our growth experiments. The total effective planar growth rate (triangles) is calculated as before and is seen to be roughly constant below 460 °C and increases somewhat at higher temperatures, but remains within ~20% of the diffusion limited growth rate for planar films on Au-free (001) GaAs substrates shown in Fig. 3.1. From this analysis we conclude the total effective planar growth rate is primarily controlled by gas phase diffusion for the case of TEGa over the entire temperature range of these experiments. Also, these data clearly confirm that it is the

thermal activation of the lateral growth that limits the axial growth in the high temperature regime for both precursors.

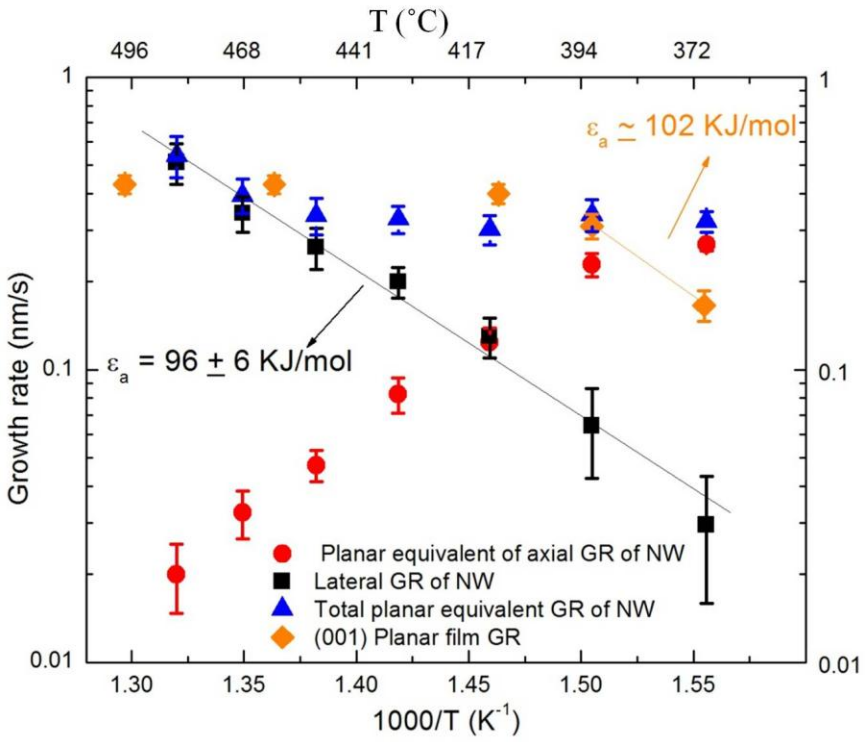


Figure 3.6. Temperature dependence of the NW effective planar growth rates and measured lateral growth rates compared to planar growth on Au-free (100) GaAs substrates. All data were obtained using TEGa.

In order to explore the implications of these results, it is interesting to consider the mean free path $\lambda_v$ for gas phase diffusion of the Ga precursor in hydrogen under the current experimental conditions. For simplicity we assume that the diffusing species near the NW/epilayer surface is TMGa. The mean free path $\lambda_c$ for collisions between TMGa and $H_2$ molecules can be estimated from the Einstein equation:

$$\lambda_c = \frac{3D}{\bar{v}} \tag{3.1}$$

where $\bar{v}$ is the mean thermal velocity ($\bar{v} = \sqrt{\frac{8RT}{\pi M}}$, where $R$ = 8.31 J.mol$^{-1}$.K$^{-1}$ and $M$ is the molar mass of TMGa equal to 114.7 g/mol). $D$ is the diffusion coefficient of TMGa through $H_2$ boundary layer and can be calculated by [61]:

$$D = \frac{2.23\times10^{-5}T^{1.73}}{P} \quad (3.2)$$

where $D$, $T$ and $P$ are in cm$^2$/s, K and atm. Assuming a hydrogen partial pressure of 50 Torr and T = 400 °C we obtain an estimate of $D$ = 26.5 cm$^2$/s. From the above value of $D$, we get $\lambda_c$ = 7.1 μm, assuming TMGa is the primary species near the surface at this temperature. This implies that on the length scales under investigation here the TMGa transport is essentially ballistic, i.e. the Ga concentration field is completely uniform over the scale of the NW length or inter-wire separation. The use of TEGa or smaller Ga-alkyl fragments will not substantially affect the estimate of $D$ above. Such a large mean free path implies that the vapor concentration of Ga species is constant over the substrate and NWs. The competition between lateral growth and NW growth is therefore determined simply by the ratio of the reaction rates for VS and VLS growth which vary according to the precursor used, as well as the growth temperature.

A question that arises is the discrepancy between the activation energy for the axial growth for TMGa observed in this work, 56 ± 6 kJ/mol, compared with that of others, e.g. Borgstrom et *al.* 67 - 75 kJ/mol [12] and Paiano et *al.* 87 ± 13 kJ/mol [8]. It is important to note that the NP densities of Paiano et *al.* were around 1 - 4×10$^8$ NP per cm$^2$ whereas ours are approximately 7×10$^9$ cm$^{-2}$ i.e. more than one order of magnitude higher. Borgström et *al.* have also observed a significant reduction in the activation energy of axial growth for GaP NWs at high Au NP density [ 12].

## 3.4 Benefits of precursor chemistry to grow radial and axial InAs-GaAs heterostructures

The significant effects of precursor chemistry on NW growth kinetics have interesting implications for control of NW heterostructures. NW device applications will require the ability to fabricate axial heterostructures in which the composition of the NW varies along the NW axis, as well as core-shell heterostructures. Figure 3.7 and 3.8 show some preliminary efforts to employ the differences in precursor chemistry to alternate

between axial and core-shell heterostructure growth. A similar method was used recently to switch between axial and lateral growth for catalyst free nanowire growth of GaAs/AlGaAs core shell structures [62].

In Fig. 3.7(a) an InAs core with diameter of 38 nm was grown using trimethylindium (TMIn) and TBAs at 400 ˚C. The TMIn was then switched off and radial growth was achieved by switching the TEGa source on for 100 s resulting in a GaAs shell with thickness of 18 nm. Note that unlike other reports [63, 64], shell growth was achieved without ramping to higher growth temperatures. Figure 3.7(a) shows a bright field (BF) TEM image of a typical InAs/GaAs core/shell NW. Figure 3.7(b) is a high resolution HRTEM image of a section of the NW shown in Fig 3.7(a). The presence of Moiré fringes with spacing of 6.5 ± 0.3 nm in the core region of the NW suggests the formation of a relaxed core/shell structure. The corresponding selected area diffraction (SAD) pattern is shown in Fig. 3.7(c) indicating the presence of double spots due to the relaxation of the heterostructure. An energy dispersive X-ray spectroscopy (EDS) K-shell line scan across the NW, shown in Fig. 3.7(d), shows a clear drop of the Ga count rate at the core region accompanied by an increase of In count rate which confirms the formation of the core-shell structure. The drop of the As counts in the core region is rather unexpected and might be due to the partial absorption of the emited photons in the core region by the shell material. The In Fig. 3.7(a), a tapered part indicated by an arrow is formed due to the VLS growth of the NW during GaAs shell growth. Hence the axial growth, while very small is not completely suppressed.

The strain relaxation in this heterostructure can be calculated from the SAD pattern and the Moiré fringe spacing. GaAs has a smaller lattice constant than InAs and therefore the outer spots correspond to GaAs and the inner ones to InAs. The relative average strain relaxation in a given direction can be calculated from the InAs-GaAs spot separation divided by the average spot position, normalized by the InAs-GaAs lattice mismatch (7.2%). From such analysis, we determined the relative radial relaxation to be (100 ± 5) %. The spot separation along the NW axis is not clear and therefore axial relaxation cannot be determined from the SAD pattern. The axial relaxation can be calculated from the Moiré fringe spacing. According to Eq. 1.7, in the case of 100% relaxation, the minimum translational Moiré fringe spacing along [111] direction of an

InAs/GaAs core/shell structure is 4.9 nm. From the measured Moiré fringe spacing we found the relative axial relaxation to be (75 ± 5) %. This result indicates higher degree of radial relaxation than the axial relaxation, consistent with a previous report on InAs/GaAs core/shell NWs and the reason is not yet clear [65].

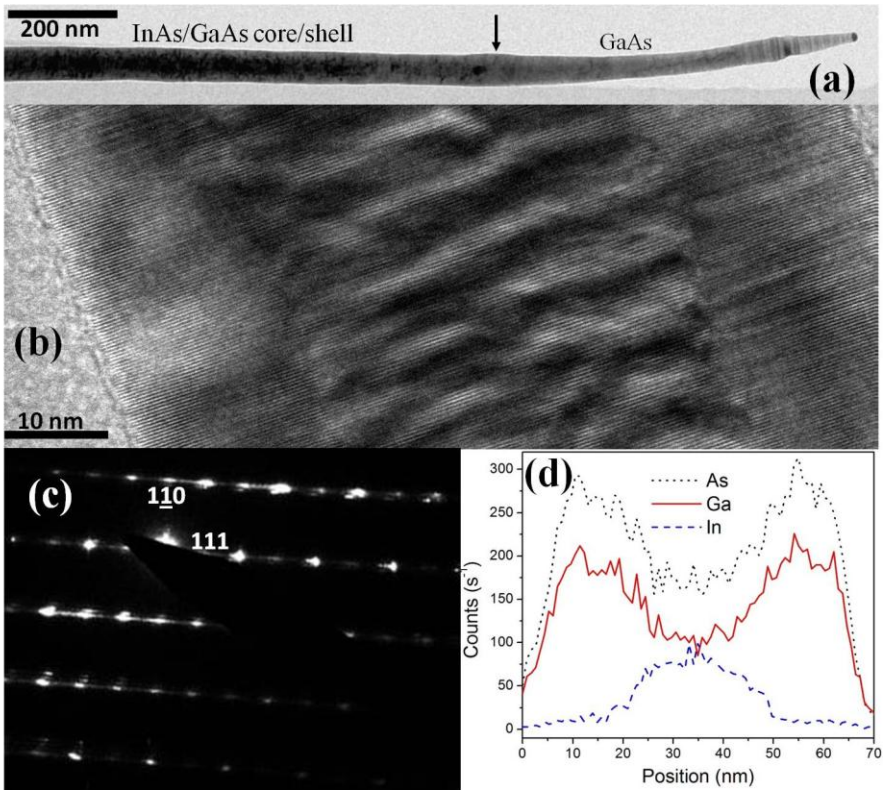


Figure 3.7. (a) BF, (b) HRTEM TEM images, c) corresponding SAD pattern and (d) EDS line scan across a core/shell InAs/GaAs NW. The black arrow in (a) shows where the VLS growth of GaAs started.

By using TMG instead of TEGa, it is possible to grow an axial heterostructure instead of a core shell structure. An InAs/GaAs axial heterostructure was achieved by growing InAs as described above and then switching off the TMIn flow and switching on the TMGa flow for 100 s. A BF and scanning-TEM images of such a structure is shown in Fig. 3.8(a) and (b), respectively. There is a clear change in the contrast along the arrow labelled 1 in Fig. 3.8(b) indicating the change in the composition along the arrow. An EDS line scan along this arrow, shown in Fig. 3.8(c), clearly confirms the formation of an axial heterostructure NWs. Figure 3.8(c) shows lower counts for In-K compared to

Ga-K which is similar to previous reports [66]. This is due to the much larger photon energy for K-shell of In (4.24 KeV) compared to the K-shell photon energy of Ga (1.30 KeV) which leads to the excitation of fewer photons for In than Ga for a given incident electron energy. Also, the EDS line scan across the Au NP, along the arrow labelled 2 in Fig. 3.8(b), is shown in Fig. 3.8(d). It is clear that In and Ga are both present in the Au NP. The presence of In in the Au NP might have resulted in the precipitation of graded InGaAs up to a length of 400 nm from the point we turned off the TMIn source (indicated by a vertical arrow in Fig. 3.8(b)) after which the growth of a pure GaAs segment was started. This might be responsible for the observed moduation in the contrast along the arrow labelled 1 in Fig. 3.8 (b). Also, during the cooling process which was performed under TBAs, both Ga and In stored in the Au NP should partially precipitate to form a small InGaAs segment right under the NP. A possible schematic structure of the axial InAs/GaAs heterostructure is shown in Fig. 3.8(e).

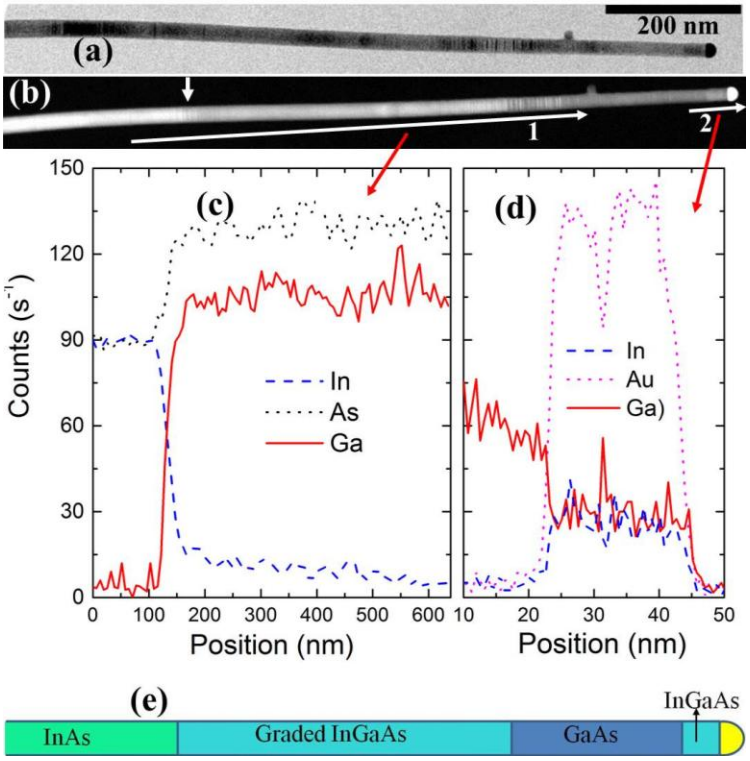


Figure 3.8. (a) BF, (b) STEM images of an axial InAs/GaAs NW and (c-d) EDS line scans along the white arrows shown in (b). (e) the expected schematic structure of the InAs/GaAs axial heterostructure.

In conclusion, we presented a systematic study of the VLS growth of GaAs NWs using two different Ga precursors, TMGa and TEGa with quite different decomposition kinetics. We observe that lateral growth and NW tapering is strongly enhanced for the case of growth with the low temperature precursor TEGa. We show that for the case of TMGa, the presence of Au NPs greatly lowers the temperature over which gas phase diffusion limited growth is observed providing strong evidence for the catalytic role of the Au NPs. Over a large range in growth temperatures, for both precursors, the observed growth rates are easily explained by a competition between VLS and VS growth with the temperature range determined by the particular Ga source kinetics. We have shown that by changing from TMGa to TEGa as the Ga precursors, we can switch the growth mode of InAs/GaAs NWs from axial to core/shell heterojunctions. In this way precursor chemistry can be employed as a useful means to control the NW growth.

# Chapter 3. Effect of group III precursor chemistry on the morphology of GaAs nanowires

## 4: EFFECTS OF $CBR_4$ ON THE MORPHOLOGY OF GAAS NANOWIRES

In addition to the effect of dopant atoms on the electrical properties of semiconductor nanowires (NWs), interesting structural changes in the NW morphology attributed to doping have been observed. For example, doping of InP, grown along [111] direction, using diethylzinc was reported to alter the crystal structure from wurtzite to zincblende [14]. Also, modulation doping of InP with diethylzinc resulted in a formation of periodic twinning planes (periodic change of side facets from {111}A to {111}B) which is predicted to induce a direct bandgap in normally indirect badgap materials [67]. Carbon is a well known and technologically important p-type dopant in planar GaAs due to its low diffusivity and high solubility in bulk GaAs; however its use as an intentional p-dopant in NW growth has been scarcely investigated [68]. Carbon halogen sources such as $CBr_4$ are extremely reactive at the surface of GaAs and other III-Vs, and it is of interest to investigate their effect on the growth of GaAs NWs as a potential means to control not only the conductivity, but also the wire shape and crystal structure. In this chapter, we investigate the effect of $CBr_4$ on the structural properties of GaAs NWs grown by MOVPE. We will discuss the electrical properties of C-doped GaAs NWs in chapter 6. The work presented in this chapter forms the basis of a paper published in Nanotechnology [69].

To grow the GaAs NWs studied in this chapter, a gold layer with a thickness of 2 nm was annealed at 400 °C resulting in NPs with sizes in the range of 30 to 150 nm. TEGa or TMGa (flow rate of 15 μmol/min), TBAs (flow rate of 63 μmol/min) and $CBr_4$ were used as the precursors. The ratio of $CBr_4$ to TEGa (IV/III) was varied in the range of 0 and 0.19. The growth temperature was 400 °C and the growth time was between 100 and 900 s.

## 4.1 Effect of initial NP size dispersion on GaAs NWs grown by TMGa/TEGa

In chapter 3, we compared the morphology of GaAs NWs grown by TMGa/TEGa using Au NPs with a fairly uniform size distribution which resulted in NWs with uniform length. In this section, first, we will compare the effect of initial Au NP size dispersion on the length dispersion of GaAs NWs grown by TMGa/TEGa, as shown in Fig. 4.1. In general, if the NW growth is dominated by direct impingement of adatoms on the Au NP, the growth rate of NWs (with NP size larger than 30 nm grown under high TMGa flow rate) with different diameter will be size-independent. This easily can be understood by considering the impingement area on the NP surface and crystallization area at the Au NP/NW interface where both are proportional to $r^2$, where $r$ is NP radius. If the NW growth is dominated by the diffusion of adatoms from the substrate and NW side facets toward the NW/NP interface, the growth rate will be inversely proportional to the NP radius [43]. In this case, the adatom incorporation will be limited by the circumference of the NW/NP which is proportional to $r$, while the crystallization area is proportional to $r^2$. Therefore, the NW growth rate will inversely depend on the NP size.

Figure 4.1 shows a very high degree of uniformity in the axial growth rates of the TMGa-grown NWs despite a large variation in initial NP diameter. This indicates that under the present conditions, the axial growth of TMGa-grown NWs is primarily determined by the direct incorporation of Ga from the vapor phase into the Au droplet. In contrast we see a much larger variation in the length of the TEGa grown NWs, and a greatly reduced growth rate overall due to competition from enhanced lateral growth. In this case, the axial growth rate is seen to be higher for small NPs, which suggests that surface diffusion of Ga adatoms is playing a rate limiting role in the incorporation of Ga in the Au NP [43].

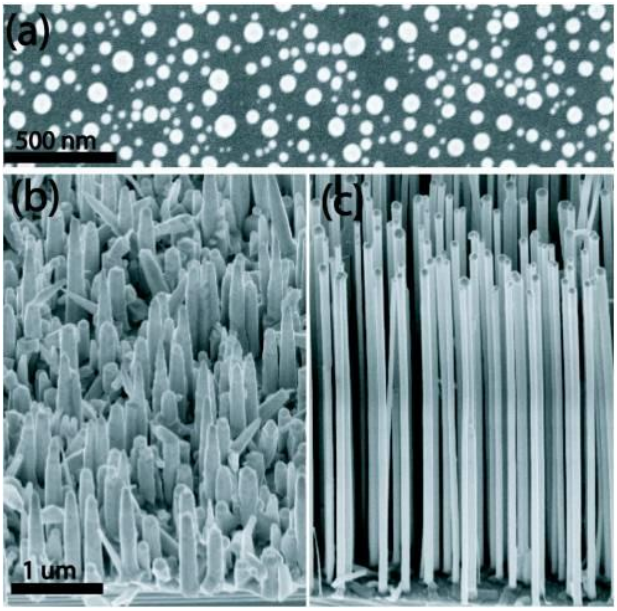


Figure 4.1. Comparison of NWs grown at 400°C using (b) TEGa, and (c) TMGa. (a) shows the initial NP distribution before growth.

## 4.2 Effects of $CBr_4$ on the morphology of TEGa-GaAs NWs

Figure 4.2 shows SEM images of GaAs NWs grown using TEGa, with and without $CBr_4$, for two different growth times. In the early stages of growth (first 100 s), there is no significant difference in the diameter at the base of the NWs grown with and without carbon. For longer growth times (900 s) it is clear that the NWs grown without $CBr_4$ are highly tapered and have a large dispersion in length. In addition, Fig. 4.2 shows that NWs grown without $CBr_4$ grow laterally over time, with base diameters significantly larger than the initial seed particle diameter. In contrast, the NWs grown with carbon show negligible tapering and lateral growth. The NWs grown in the presence of $CBr_4$ have significantly larger axial growth rates and greatly reduced dispersion in length similar to the case of the TMGa NWs in Fig. 4.1. We should note that the growth of GaAs NWs using TMGa in the presence of $CBr_4$ had no effect on the morphology and growth rate of the NWs.

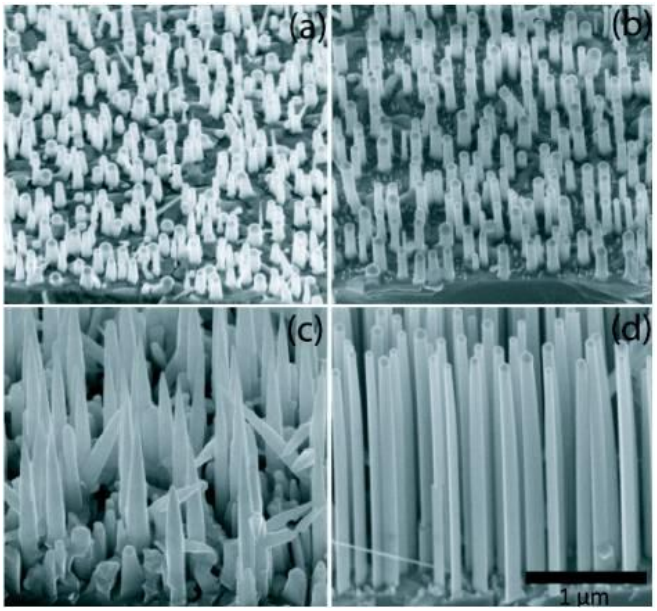


Figure 4.2. SEM images taken at 45˚ tilt angle of GaAs NWs grown using TEGa without $CBr_4$ (a) for 100 s and (c) 900 s, and with $CBr_4$ (IV/III=0.1) (b) 100 s and (d) 900 s.

Figure 4.3 shows plan-view SEM images of GaAs NWs grown with TEGa, with and without $CBr_4$ for different growth times. In both cases the NWs start growing with a triangular cross section. NWs grown without $CBr_4$ grow laterally over time and show a transition from triangular to hexagonal cross section, while NWs grown with $CBr_4$ keep their triangular cross section as well as a constant lateral dimension over the growth time. The facets correspond to the {112} planes in all cases, in agreement with previous reports for TMGa-grown NWs [8]. Plan view images for TMGa grown NWs grown with or without $CBr_4$ always showed hexagonal cross section with {112} planes. The origin of these differences in facet structure is unclear at present. One possibility is the difference in the surface chemistry of the NW facets grown by TMGa and TEGa. Considering the decomposition mechanisms of TMGa and TEGa, as discussed in chapter 1, the surface of TMGa-GaAs NW facets should by covered with methyl radicals, while the TEGa-GaAs NW facets should be clean.

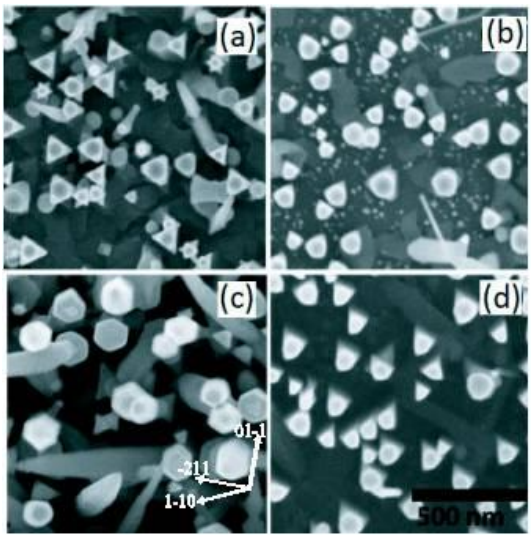


Figure 4.3. Plan-view SEM images of GaAs NWs grown without $CBr_4$ (a) for 200 s and (c) 900 s, and with $CBr_4$ (IV/III=0.1) (b) 200 s and (d) 900 s. All samples were grown with TEGa.

Figure 4.4 shows a statistical analysis of the SEM images of TEGa-grown NWs, with and without $CBr_4$ for different growth times. Figure 4.4(a) shows that the axial growth rate of the NWs grown with $CBr_4$ is constant over time, while the axial growth rate of the NWs grown without $CBr_4$ decreases over time. In addition, the axial growth rate of the NWs grown with $CBr_4$ is significantly higher and shows much lower dispersion than the growth rate of the NWs grown without $CBr_4$.

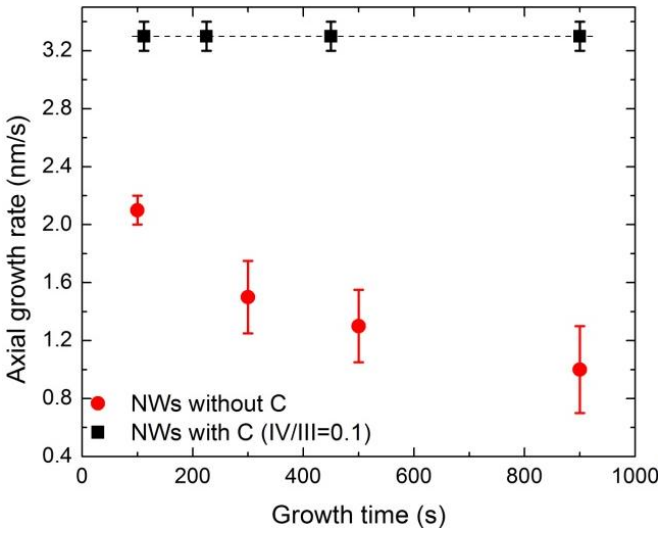


Figure 4.4. Plot of the axial growth rate of the NWs grown using TEGa with $CBr_4$ (IV/III= 0.1) and without $CBr_4$ vs. growth time.

To further investigate the effects of $CBr_4$ on the growth of GaAs NWs, we fabricated NWs with different IV/III ratios, keeping the TEGa flow constant (Fig. 4.5). The results show that the axial growth rate increases by a factor of three for the NWs grown with the highest $CBr_4$ flow (IV/III= 0.19) compared to the NWs grown without $CBr_4$ (Fig. 4.5(a)). In addition, the lateral growth rate measured at the NW base decreases from 0.052 nm/s for the NWs grown without carbon to 0.009 nm/s for those with the highest carbon flow (Fig. 4.5(b)). This trend closely mirrors the decreasing growth rate observed for planar layers using $CBr_4$ on (001) substrates in the absence of Au NPs (Fig. 4.5(c)). Note that we cannot directly compare the absolute lateral growth of the NWs with the planar growth rate on (001). First, the presence of Au NPs will reduce the available concentration of Ga adatoms for lateral growth due to competition from the VLS mechanism, and second the [001] surface is not chemically equivalent to the {112} facets of the NW sidewalls.

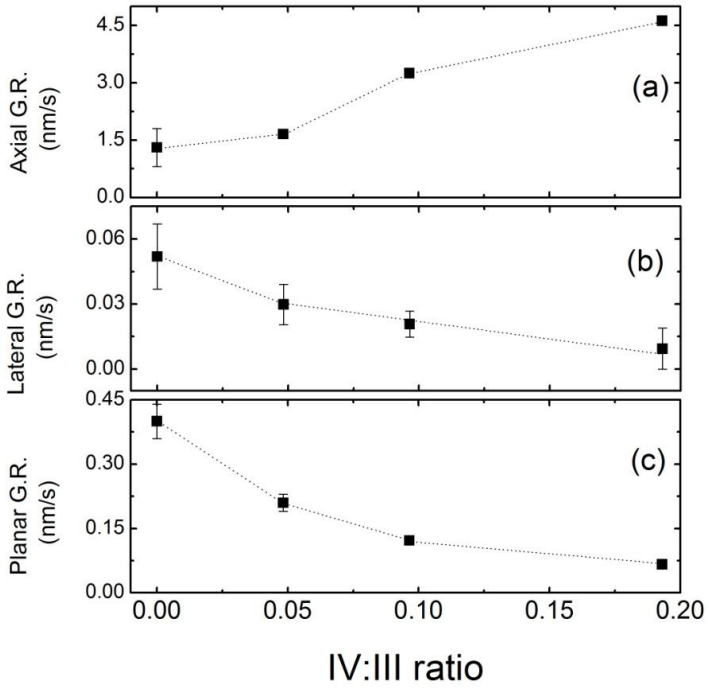


Figure 4.5. Comparison of the effect of $CBr_4$ exposure on (a) NW axial growth (b) NW lateral growth rate measured at NW base, and (c) planar growth rate on (001) substrates in the absence of Au NPs. All data are for growth with TEGa. Lines are a guide to the eye.

The data presented in section 4.1 indicate that the decomposition of TMGa is only efficient in the vicinity of the Au NP catalyst at a growth temperature of 400 ˚C. This gave rise to a lack of length dispersion with NP diameter. This is consistent with the fact that GaAs growth in the presence of Au NPs is limited by surface reaction kinetics as discussed in section 3.3. Therefore, direct impingement of cracked group III precursor from gas phase onto the Au NP is the primary incorporation mechanism to grow TMGa-GaAs NWs at 400 ˚C via VLS mechanism. The VS growth on NW facets and the substrate surface is kinetically suppressed (Fig. 4.6(a)). For TEGa growth in the presence of Au NPs, based on the results presented in section 1.4 and 3.3, precursor cracking and GaAs growth occurs on the substrate surface and NW side facets, in addition to the VLS growth at the NP/NW interface. The observed dispersion in the length of the TEGa-GaAs NWs in Fig. 4.1(b), indicates that the diffusion of Ga adatoms from the substrate and NW sidewall facets toward the NW/NP boundary is a significant incorporation

pathway of Ga for the growth of GaAs NWs using TEGa. In addition, direct incorporation of cracked precursors into the Au NPs should also be possible, although with a much lower incorporation rate compared to growth with TMGa (Fig. 4.6 (b)). The observed decrease in axial growth rate with time for the TEGa-GaAs NWs indicated in Fig. 4.4 further suggests that surface diffusion limits the incorporation of Ga in the Au NPs for NWs grown with TEGa in the absence of $CBr_4$. With increasing growth time, the diffusion of Ga adatoms from the substrate to the Au NPs becomes less and less likely.

As shown in Fig. 4.5(a) the addition of $CBr_4$ results in a dramatic enhancement in the growth rate and a suppression of tapering for NWs grown using TEGa. This is primarily due to the suppression of the VS growth by the $CBr_4$ precursor. Suppression of planar III-V growth rates using carbon halogen precursors such as $CBr_4$ or $CCl_4$ is well known and is believed to be due to parasitic surface reactions between the group III precursor and the halogen precursors [70]. It is believed that bromine attacks the Ga adatoms on the GaAs surface and desorbs as GaBr or $GaBr_3$. Therefore, the cracked TEGa primarily incorporates via direct impingement from gas phase onto the Au NP to grow TEGa-GaAs NWs via the VLS mechanism similar to TMGa-GaAs NWs. In other words, the effect of the $CBr_4$ is to suppress the lateral growth rate, which allows the NP to collect the available Ga flux. Therefore, the growth rate of TEGa-GaAs NWs in the presence of $CBr_4$ is independent of the size of the Au NP similar to the case of NWs grown using TMGa.

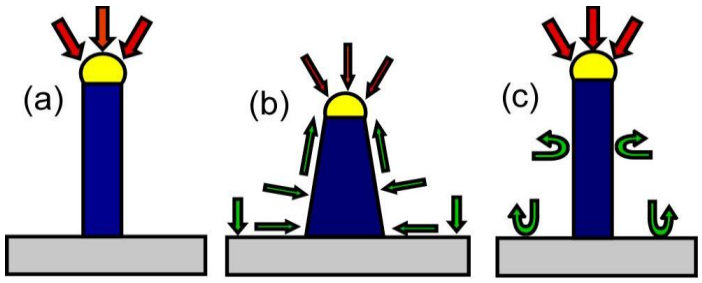


Figure 4.6. Schematic incorporation pathway of group III in GaAs NWs grown at 400 ˚C using (a) TMGa, (b) TEGa and (c) TEGa in the presence of $CBr_4$.

### 4.3 Effect of $CBr_4$ on the crystal structure of GaAs NWs grown with TEGa

A bright field (BF) TEM image of a TEGa-GaAs NW is shown in Fig. 4.7 which shows the presence of a small Au NP at the tip. High resolution TEM (HRTEM) image of the Au NP is shown in Fig. 4.7(b). In addition, the presence of alternating regions with zincblende (ZB) and wurtzite (WZ) structures is clear in Fig. 4.7(c). Another example of a TEGa-GaAs NW is shown in Fig. 4.8(a1-3). The corresponding HRTEM image (Fig. 4.8(a2)) shows overall ZB structure with a high density of twin boundaries and stacking faults (indicated by arrows in Fig. 4.8(a2)). The streaky pattern observed in the selected area diffraction (SAD) pattern shown in Fig. 4.8(a3), along a <1$\underline{1}$0> pole, is due to the existence of twin boundaries and stacking faults. We should note that, in some cases the Au NP was missing from the tip of the highly tapered NWs likely due to breakage while transferring the NWs into the TEM grid. NWs were transferred to a TEM grid by scratching the TEM grid on the NW sample. Also, we should note that the difference between ZB and WZ structures is only due to the stacking sequence of Ga-As bilayers which is ABCABC... for ZB and ABAB... for WZ structures.

Figure 4.8(b1-b3) show the corresponding <1-10> pole images of a NW grown under the presence of $CBr_4$ vapor (IV/III= 0.19), showing a strong reduction in tapering as previously discussed. In addition, there is no evidence of stacking faults, and the crystal structure indicated by the SAD image is exclusively ZB. Both sets of NWs, discussed here, were grown for identical growth times.

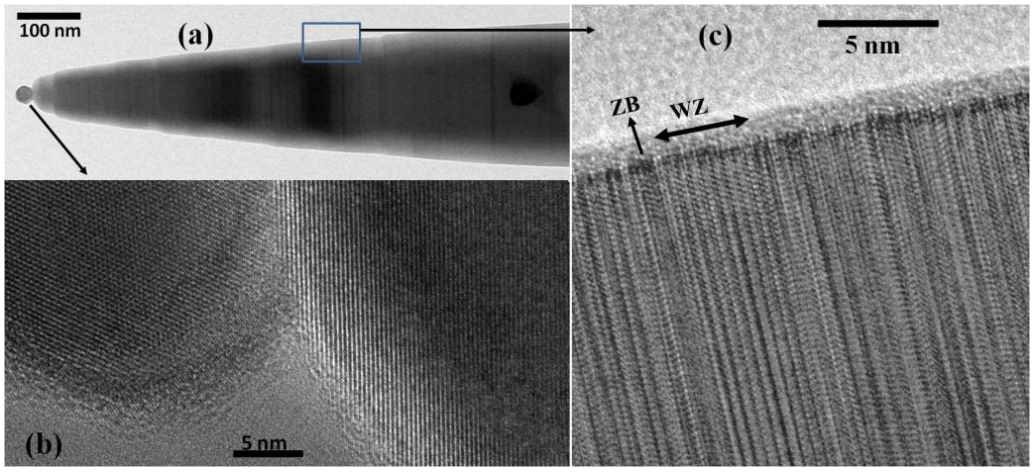


Figure 4.7. (a) BF TEM image of a TEGa-GaAs NW, (b) HRTEM image of the Au NP at the tip of the NW and (c) HRTEM of the region indicated by a box in (a).

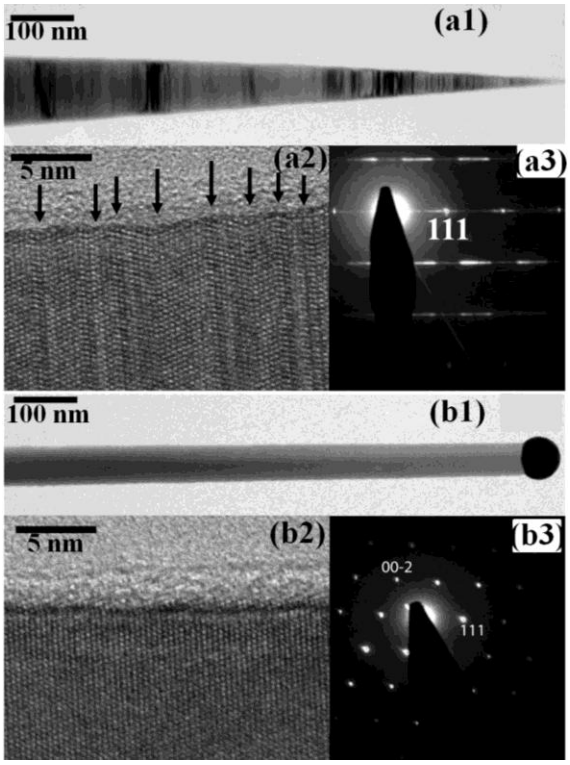


Figure 4.8. BF TEM and HRTEM and SAD pattern of the GaAs NWs along the (1-10) pole (a1-a3) grown without carbon and (b1-b3) with carbon (IV/III= 0.19), respectively. The arrows in (a2) indicate the position of twin boundaries and stacking faults.

The role of $CBr_4$ in reducing stacking fault density is not yet fully understood. Joyce et al. have observed a significant reduction in stacking fault density in GaAs NWs grown using TMGa by increasing the growth rate. They speculated that stacking faults form to relieve the tension at the NW/NP interface. They argued that increasing the growth rate results in an increase in the Ga composition of the NP which reduces interfacial tensions resulting in a decrease in the stacking fault density [71]. Similar mechanisms may apply in the current situation, where the increased axial growth rate of TEGa-GaAs NWs was observed in the presence of $CBr_4$. We should note that, at high vapor phase Ga supplies, as is the case in our work and in ref. [71], the chemical potential of the NP is high and therefore the liquid-solid supersaturation is high. Therefore, we can conclude that high liquid-solid supersaturation may favour the nucleation with ZB structure.

It is generally believed that stacking fault formation cannot be explained only by thermodynamic considerations and that kinetic effects have to be considered as well [73, 72]. A possible explanation, based on the position of the initial nucleus at the NW/NP interface, is as follows. The incorporation pathway of the group III precursor determines the position of the initial nucleus at the NW/NP interface. In TEGa-GaAs NWs grown with $CBr_4$, (or in NWs grown with TMGa) direct impingement is the primary incorporation pathway of Ga. Therefore, it is possible to assume that the initial nucleus forms inside the NP at the NW/NP interface as shown in Fig. 4.9(a). In TEGa-GaAs NWs grown without $CBr_4$, adatom diffusion and direct attachment to the NW sidewalls is the primary incorporation pathway of Ga. Therefore, in this case, it is possible to assume that the initial nucleus mainly forms at the edge of the NW/NP interface as shown in Fig. 4.9(b). In the latter case, part of the nucleus is in contact with the vapor phase, while in the former case it is only in contact with the liquid NP. Since the surface energy of the NW side facets in contact with vapor phase and with WZ structure is lower than that of the ZB structure, the nucleus formed at the edge of the NW/NP interface may adopt the WZ structure to lower its surface energy [74, 75]. The lower surface energy of the NW with WZ structure than that with a zincblende structure is due to a lower number of surface dangling bonds in the WZ structure compared with the ZB structure [74]. For the

nucleus formed entirely inside the NP, all the dangling bonds are saturated and the nucleus will follow the zincblende crystal structure which is more stable than WZ structure. We should note that the position of the initial nucleus may depend on many factors including the pathway of growth species [73], droplet volume [136] and faceting of the growth interface [137] and, in general, is a matter of controversy in the literature [45].

A similar change in crystal structure has been reported for InAs NWs grown axially on top of GaAs NWs. It was shown that if the length of the GaAs base is longer than the indium adatom diffusion length, InAs grows with pure zincblende structure. In this case, the direct impingement of the vapor phase growth species on the NP is the dominant incorporation pathway and therefore the initial nucleus likely forms inside the NP and therefore zincblende structure is preferred, as discussed earlier. For GaAs base shorter than the indium adatom diffusion length, in addition to direct impingement of growth species from vapor phase onto the NP, indium adatoms are able to reach the triple boundary via diffusion through the side facets. Therefore in this case, the initial nucleus may form inside the NP or at the edge of the NW/NP interface and therefore stacking faults formation was observed [73].

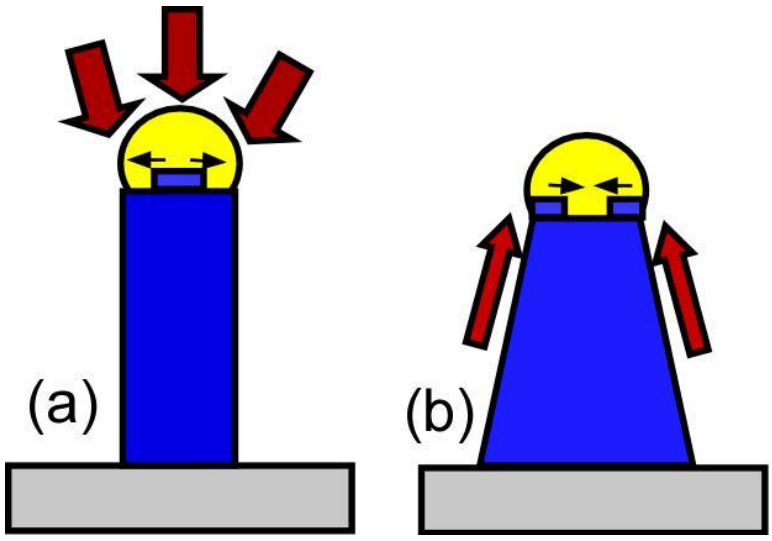


Figure 4.9. Schematic of the initial nucleation position in TEGa-GaAs NWs grown (a) with and (b) without $CBr_4$.

In summary, we have observed a striking effect on the morphology of GaAs NWs grown using TEGa by addition of $CBr_4$ dopant. A dramatic increase in the axial growth rate and a corresponding reduction in tapering have been observed for NWs grown in the presence of $CBr_4$. This is attributed to the suppression of planar and lateral growth by the $CBr_4$ source, resulting in an enhanced axial growth rate of the NWs. In addition, GaAs NWs grown in the presence of $CBr_4$ are free of stacking faults with zincblende structure, while NWs grown in the absence of $CBr_4$ are highly tapered and contain a high density of stacking faults. This was argued to arise from differences in the position of the initial nucleus depending on whether direct impingent from vapor phase onto the NP or surface adatom diffusion predominates. These results show the remarkable effect of precursor chemistry on nanowire morphology.

## 5: GEOMETRIC LIMITS OF COHERENT III-V CORE/SHELL NANOWIRES

The NW geometry allows the strain partitioning in both core and shell regions facilitating the growth of dislocation free axial and radial heterostructures with dimensions above the critical thicknesses known for thin films. This characteristic of the semiconductor NWs has opened a broader window to employ strain engineering [76, 77] and quantum confinement effects [78] to design and fabricate core/shell NW based-devices [79, 80]. The rational design of these devices requires the knowledge of the coherency limits in core/shell NWs. Otherwise, the formation of dislocations will degrade the device performance [65]. Several groups have attempted to determine the coherency limit and/or strain distribution in core/shell NWs using elasticity theory via finite-element analysis [81], variational methods [17] or an analytical approach [18, 19]. Using the variational approach, Raychaudhuri et al. [17] determined the total strain energy of a core/shell structure ***numerically*** with the assumption that the strain components are ***position-independent*** in the core and shell regions. Then, they estimated the critical dimensions by numerically determining the shell thickness, for a given core radius, for which it became energetically favourable to include a dislocation. Haapamaki et al. determined the total strain energy ***analytically*** considering the strain components to be ***position-dependent*** [18]. Then, they obtained the critical dimension of InAs/$Al_xIn_{1-x}As$ core/shell NWs by determining the geometric limits at which the total strain energy exceeded the dislocation energy. Both of these models predicted an increase of the critical shell thickness with decreasing core radius and the presence of a critical core radius under which the critical shell thickness tended to infinity [17-19]. However, comparison of predicted results with experimental data for core/shell NWs is rather limited to a specific material system and a limited geometric range [18, 82].

In this chapter, we report the growth of zincblende and wurtzite III-V core/shell NWs and calculate the expected strain distribution and the geometric limits of the coherent radial heterostructure NWs. We considered the strain components to be ***position-dependent***, similar to ref [18] and determined the total strain energy and strain

components ***numerically***, similar to ref [17]. Our numerical results are in agreement with our experimental results found for wurtzite InAs/InP and zincblende GaAs/GaP core/shell NWs and results reported in the literature. The work presented in this chapter forms the basis of two papers (J. Appl. Phys. [97]) and another paper submitted to J. Appl. Phys.).

To grow the samples studied in this chapter, a gold layer with a thickness of 0.5 nm was annealed at 460 °C resulting in NPs with sizes in the range of 15 nm to 110 nm. Trimethylindium (TMIn) (flow rate 9.9 μmol/min) and TBAs (flow rate 66 μmol/min) were used as the group III and V precursors to grow the InAs core NWs for 400 s. The growth of the InP shell was achieved by switching off the TBAs and switching on the tertiarybutylphosphine (TBP) (flow rate 960 μmol/min) for 250 s. The V/III ratio was 6.6 and 97 for the growth of the InAs core and InP shell, respectively. The sample was then cooled under TBP/$H_2$. Both InAs core and InP shell materials were grown at 460 °C. To grow GaAs/GaP core/shell NWs, the GaAs core was grown using trimethylgallium (TMGa, flow rate of 21.4 μmol/min) and TBAs (flow rate 164 μmol/min). The growth of the GaP shell was achieved by switching off the TMGa and TBAs and switching on the TEGa (flow rate 15.1 μmol/min) and TBP (flowrate 960 μmol/min) for 200-400 s. The V/III ratio was 7.6 and 63.7 for the growth of the GaAs core and GaP shell, respectively. The sample was then cooled under TBP/$H_2$. Both the GaAs core and GaP shell materials were grown at 410 °C.

The growth of the GaSb shell on GaAs and GaP cores was achieved by switching off the TMGa and TBAs and switching on the TEGa with a flow rate of 7.5 μmol/min, and trimethylantimony (TMSb) with a flow rate of 24 μmol/min, for a growth time of 100-600 s. The sample was then cooled by switching off all the sources under $H_2$. Both core and shell materials were grown at 410 °C. To grow GaP shell, TMGa with a flow rate of 15 μmol/min and tertiarybutylphosphine (TBP) with a flow rate of 960 μmol/min were used at growth temperature of 410 ˚C. The total growth time was 200 s in each case.

## 5.1 Model

### 5.1.1 Wurtzite core/shell NWs

In this model, we ignored the faceting of the NW and considered two coaxial cylinders with a core radius of $r_c$ and a shell thickness of $t$ as shown in Fig. 5.1. A cylindrical coordinate system was defined at the core/shell interface (defined by unit vectors $\mathbf{e_r}$, $\mathbf{e_\theta}$, $\mathbf{e_z}$). The magnitude and distribution of the strain components ($\varepsilon^i_k(r)$, where $i$ stands for either core (c) or shell (s) and $k = r, \theta, z$) in the core and shell regions are mainly determined by 1) the coherency has to be maintained at the core/shell interface and 2) the total strain energy in the system has to be a minimum. The interfacial strain components at the hetero-interface are defined as follows:

$$\varepsilon_z^c(r = r_c) = f_z^c = \frac{a_z - a_z^c}{a_z^c} \tag{5.1a}$$

$$\varepsilon_\theta^c(r = r_c) = f_\theta^c = \frac{a_\theta - a_\theta^c}{a_\theta^c} \tag{5.1b}$$

$$\varepsilon_z^s(r = r_c) = f_z^s = \frac{a_z - a_z^s}{a_z^s} \tag{5.1c}$$

$$\varepsilon_\theta^s(r = r_c) = f_\theta^s = \frac{a_\theta - a_\theta^s}{a_\theta^s} \tag{5.1d}$$

where $a_k$ and $a^i_k$ are, respectively, the strained and relaxed lattice constants in $k = z, \theta$ directions ($i = c, s$ which stand for core or shell, respectively).

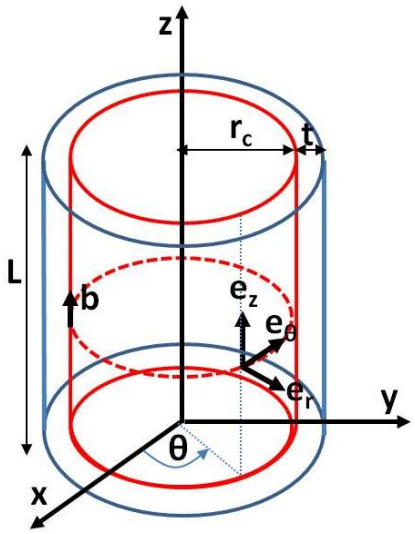


Figure 5.1. Schematic of the core/shell NW geometry with a core radius of $r_c$, shell thickness of $t$ and length of $L$. The dashed loop represents an edge dislocation loop with Burger's vector along the NW growth direction.

In general, strain components can be determined from the components of the displacement vector ($\vec{u}(r,z) = u_r(r)\mathbf{e_r} + u_z(z)\mathbf{e_z}$) as follows:

$$\varepsilon_r^i = \frac{\partial u_r^i(r)}{\partial r} \tag{5.2a}$$

$$\varepsilon_\theta^i = \frac{u_r^i(r)}{r} \tag{5.2b}$$

$$\varepsilon_z^i = \frac{\partial u_z^i(z)}{\partial z} \tag{5.2c}$$

where $u_r$ and $u_z$ are the components of the displacement vector along $\mathbf{e_r}$ and $\mathbf{e_z}$ directions, respectively. We should note that the NW symmetry in the azimuthal direction results in $u_\theta(\theta) = 0$ ($u_\theta(0) = u_\theta(2\pi) = 0$). The displacement components can be determined using the *equilibrium equations of elasticity* [83]*:*

$$\frac{\partial \sigma_r^i}{\partial r} + \frac{\sigma_r^i - \sigma_\theta^i}{r} = 0 \tag{5.3a}$$

$$\frac{\partial \sigma_z^i}{\partial z} = 0 \tag{5.3b}$$

where $\sigma^i_k$ is the stress along the $k^{\text{th}}$ direction and normal to a plane whose outward normal is along the $k^{\text{th}}$ direction ($i = c,s$ stands for core and shell). The values of $\sigma^i_k$ are related to the stiffness constants ($c_{nm}$) by:

$$\sigma_r^i = c_{11}\varepsilon_r^i + c_{12}\varepsilon_\theta^i + c_{13}\varepsilon_z^i \quad (5.4a)$$

$$\sigma_\theta^i = c_{12}\varepsilon_r^i + c_{11}\varepsilon_\theta^i + c_{13}\varepsilon_z^i \quad (5.4b)$$

$$\sigma_z^i = c_{13}\varepsilon_r^i + c_{13}\varepsilon_\theta^i + c_{33}\varepsilon_z^i \quad (5.4c)$$

Substituting Eq. (5.4a-c) in Eq. (5.3a) and (5.3b) leads to the following partial differential equations:

$$\frac{\partial^2 u_r^i}{\partial r^2} + \frac{\partial u_r^i}{r\partial r} - \frac{u_r^i}{r} = 0 \quad (5.5a)$$

$$\frac{\partial^2 u_z^i}{\partial z^2} = 0 \quad (5.5b)$$

Equations (5.5a) and (5.5b) have the following general solutions:

$$u_r^i = \alpha_i r + \frac{\beta_i}{r} \quad (5.6a)$$

$$u_z^i = \gamma_i z + \varphi_i \quad (5.6b)$$

The coefficients in Eq. (5.6a) and (5.6b) can be determined by imposing the following boundary conditions:

1. $u^c{}_r$ is finite as $r$ approaches zero. Therefore, $\beta_c = 0$.

2. $u^i{}_z$ (z = 0) = 0 which results in $\varphi_i = 0$.

3. $\varepsilon_z^c(r = r_c) = f_z^c$.

4. $\varepsilon_\theta^c(r = r_c) = f_\theta^c$.

5. Coherency at the core/shell interface results in:

$$\varepsilon_z^s(r = r_c) = \frac{a_z^c}{a_z^s}(f_z^c + 1) - 1 \quad (5.7a)$$

$$\varepsilon_\theta^s(r = r_c) = \frac{a_\theta^c}{a_\theta^s}(f_\theta^c + 1) - 1 \quad (5.7b)$$

6. Stress normal to the free surface is zero ($\sigma_r^s(r_c + t) = 0$).

Using these boundary conditions, we determined the coefficients in Eq. (6a) and (6b) as a function of $c^i{}_{nm}$, $f^c{}_z$, $f^c{}_\theta$, $r_c$ and $t$. For a given $r_c$ and $t$, the values of $f^c{}_z$, $f^c{}_\theta$ will be determined numerically by minimizing the total strain energy in the core/shell structure which is given by:

$$\frac{U^{strain}(r_c,t,f_z^c,f_\theta^c)}{L} = \frac{1}{2}\int_0^{r_c}\int_0^{2\pi}\sigma_k^c\varepsilon_k^c r dr d\theta + \frac{1}{2}\int_{r_c}^{r_c+t}\int_0^{2\pi}\sigma_k^s\varepsilon_k^s r dr d\theta \quad (5.8)$$

where $L$ is the length of the NW and sums over the repeated indices were assumed.

Partial relaxation of the heterostructure can happen by insertion of a dislocation at the interface. The actual misfit dislocation formation mechanism and configuration for

core-shell NWs may be complicated and, in general, depends on the NW dimensions and the misfit between the core and shell material [84, 85]. Here, we only consider the case of a pure edge dislocation loop of radius $r_c$ with a Burger's vector of magnitude $b$ along the NW growth direction (Fig. 5.1). Similar to other reports we found only dislocations with such an edge component experimentally and their formation mechanism whether by a glide or climb processes [82, 84, 85, 86] remains to be confirmed. In wurtzite semiconductors, a dislocation loop around the core has energy equal to [87]:

$$\frac{U^{dis}}{L} = \frac{1}{2} K b^2 r_c (\ln\left(\frac{32 r_c}{b}\right) - 2) \quad (5.9)$$

where

$$K = (\bar{c}_{13} + c_{13}) \sqrt{\frac{c_{44}(\bar{c}_{13} - c_{13})}{c_{11}(\bar{c}_{13} + c_{13} + 2c_{44})}} \ , \ \bar{c}_{13} = \sqrt{c_{11} c_{33}}$$

The critical dimensions can be estimated for a given core radius by numerically determining the critical shell thickness at which $U^{strain}$ (Eq. 8) exceeds $U^{dis}$(Eq. 9), under the assumption that there is no energy barrier for dislocation nucleation.

### 5.1.2 Zincblende core/shell NWs

The above approach should be modified for zincblende core/shell NWs. Equation 4.5(a-c) changes to:

$$\sigma_r^i = c_{11}\varepsilon_r^i + c_{12}\varepsilon_\theta^i + c_{12}\varepsilon_z^i \quad (5.4a)$$

$$\sigma_\theta^i = c_{12}\varepsilon_r^i + c_{11}\varepsilon_\theta^i + c_{12}\varepsilon_z^i \quad (5.4b)$$

$$\sigma_z^i = c_{12}\varepsilon_r^i + c_{12}\varepsilon_\theta^i + c_{11}\varepsilon_z^i \quad (5.4c)$$

Also, the dislocation loop energy changes to [88]:

$$\frac{U^{dis}}{L} = \frac{b^2 \mu}{2(1-\nu)} r_c (\ln\left(\frac{32 r_c}{b}\right) - 2) \quad (5.9)$$

where $\mu$ and $\nu$ are the shear modulus and Poisson's ratio, respectively. The values of $\mu$, $\nu$ and $c_{ij}$ are summarized in Table 5.1. To determine the stiffness constants for the wurtzite structure, Martin's transformations were employed [89].

Table 5.1. Summary of reported values of the shear modulus, $\mu$, the Poisson's ratio, $\nu$ and the stiffness constants, $c_{ij}$ for selected compound semiconductors with zincblende (ZB) structure and calculated $c_{ij}$ for wurtzite (WZ) structure.

| | $C_{11}$ (GPa) | $C_{12}$ (GPa) | $C_{44}$ (GPa) | $\mu$ (GPa) | $\nu$ |
|---|---|---|---|---|---|
| GaAs (ZB)* | 119 | 53.8 | 59.5 | 32.8 | 0.31 |
| GaP (ZB)* | 140.5 | 62.1 | 70.3 | 39.2 | 0.31 |
| GaSb (ZB)** | 88.3 | 40.2 | 43.2 | 24.0 | 0.31 |
| InAs (ZB)* | 83.3 | 45.3 | 39.6 | 19.0 | 0.35 |
| InP (ZB)* | 101.1 | 56.1 | 45.6 | 22.5 | 0.36 |
| InSb (ZB)*** | 66.0 | 38.0 | 30.0 | 15.1 | 0.35 |
| | $C_{11}$ | $C_{12}$ | $C_{13}$ | $C_{33}$ | $C_{44}$ |
| GaAs (WZ) | 142.0 | 48.7 | 35.9 | 154.9 | 38.4 |
| InAs (WZ) | 100.3 | 42.1 | 31.6 | 110.8 | 23.0 |
| InP (WZ) | 120.3 | 52.3 | 40.7 | 131.9 | 27.1 |

*[90], **[91], ***[92]

### 5.1.3 Predictions of the model

Figure 5.2 shows the strain components as a function of radial distance from the center of a wurtzite InAs/InP core/shell NW (solid lines) with core radius of 20 nm and shell thickness of 10 nm. This graph was generated numerically by minimizing the total strain energy in Eq. 5.8 and using Eq. 5.2(a-c) and 5.7(a-b). The InAs core, which has a larger lattice constant than the InP shell, is under compressive strain (negative value) in all directions and the strain components are position independent. Also, the radial and tangential strains are equal in the core regions, similar to the case of thin film heterostructures, as expected due to symmetry considerations. The shell region is under tensile strain in the $\mathbf{e_z}$ and $\mathbf{e_\theta}$ directions, while it is compressed in the radial direction. The radial compression in the shell is a direct result of the 6$^{th}$ boundary condition listed above. In the shell region, the strain components in the $\mathbf{e_\theta}$ and $\mathbf{e_r}$ directions are position dependent, while the strain is position independent in the $\mathbf{e_z}$ direction. In the case of a

wurtzite InP/InAs core/shell NW (dashed lines), the signs of the strain components are opposite to the ones in the InAs/InP core/shell NW. The strain accommodation in the InP core (InAs shell) of the InP/InAs NW is slightly lower (higher) than the strain in the InAs core (InP shell) of the InAs/InP NW. Qualitatively, similar results were obtained for zincblende NWs. These results are in qualitative agreement with the results reported in ref. [19] for Si/Ge NWs; however there is a clear discrepancy between our results and those of ref. [18] where it was reported that the core with the larger lattice constant is under tensile strain and the shell with the smaller lattice constant is under compressive strain in $\mathbf{e}_z$ and $\mathbf{e}_\theta$ directions.

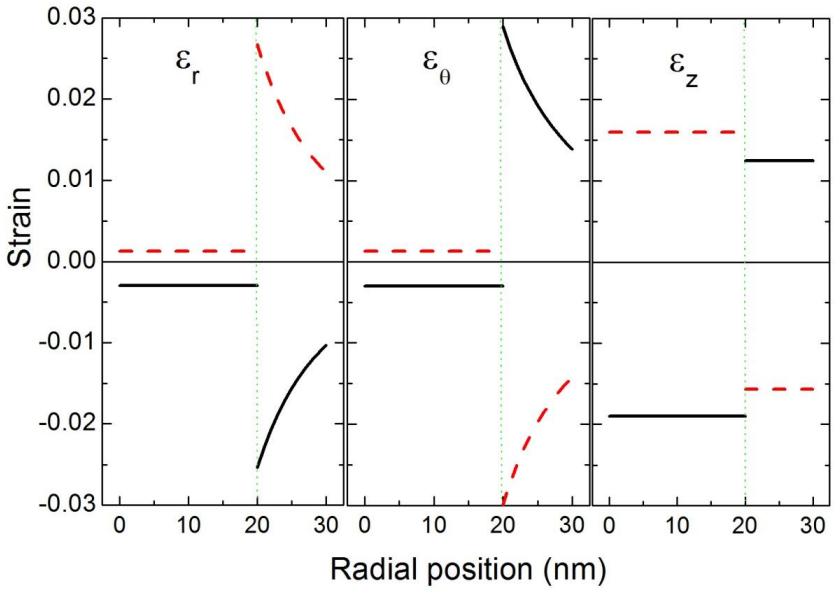


Figure 5.2. Plot of the strain components as a function of radial distance from the center of the core. Solid lines and dashed lines correspond to wurtzite InAs/InP and InP/InAs core/shell NWs, respectively, with core radius of 20 nm and shell thickness of 10 nm. The vertical dotted line represents the core/shell interface.

Figure 5.3(a) shows the calculated interfacial axial and tangential strain components (at $r = r_c$) of an InAs core with a radius of 20 nm and an InP shell with a thickness varying in the range of 1 nm to 50 nm. With increasing shell thickness, the interfacial axial strain in the InP shell decreases continuously from 0.029 to 0.002, while

the interfacial axial strain in the InAs core increases from -0.004 to -0.029. A similar trend with much smaller gradient was observed in the case of the tangential strains in the core/shell interface. However, it is clear that the interfacial tangential strain in the shell remains substantially larger than that in the core region. These numerical results indicate that, for thick shells, the interfacial tangential strain concentrates in the shell region, while the axial strain concentrates in the core. The tangential strain in the shell is position-dependent and drops quickly away from the core/shell interface, while it is position-independent in the core. Therefore, energetically, it is more favourable for the shell to accommodate the tangential strain to minimize the total strain energy. On the other hand, the axial strain is position-independent in both core and shell regions. For thin shells, axial strain can be accommodated by the shell, while for thicker shells, axial strain must be accommodated by the core in order to lower the total strain energy. This partitioning of the strain fields in core/shell NWs should therefore result in critical shell thicknesses above the known values for thin films.

The total strain energy of the core/shell NW and the dislocation energy per unit length are plotted as a function of shell thickness in Fig. 5.3(b). Strain energy increases with increasing shell thickness and exceeds the dislocation energy for shell thicknesses larger than 45 nm. Therefore, the critical shell thickness for a NW with radius of 20 nm is 45 nm. The saturation of strain energy for thick shells is due to the fact that tangential strain in the shell drops away from the interface (see Fig. 5.2) and the axial strain in the core reaches its maximum limit (see Fig. 5.3). In the core region, axial strain is the dominant component and therefore the formation of dislocation loops with line direction perpendicular to the NW axis can most effectively relieve the axial strain, significantly lowering the total strain energy.

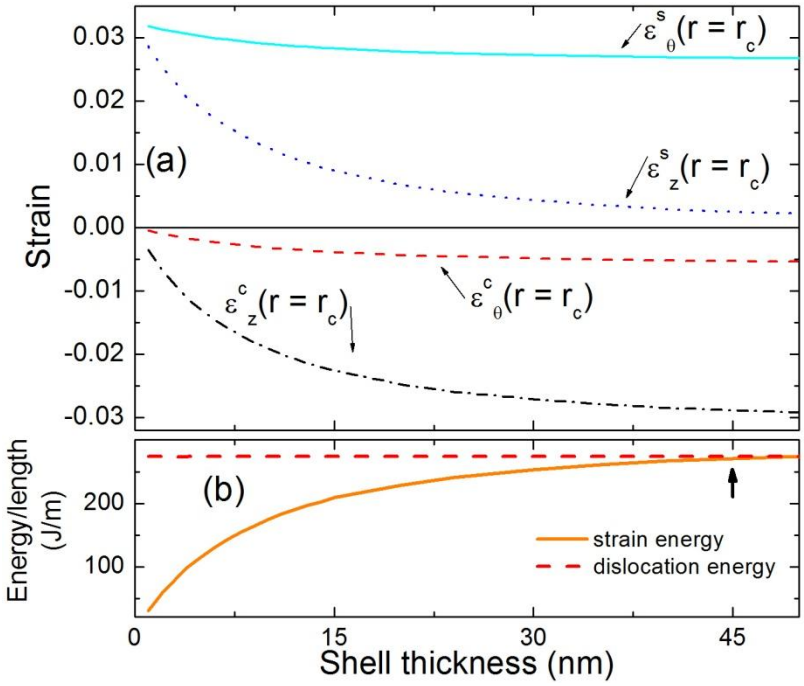


Figure 5.3. (a) Plot of the change in the interfacial strain components (at $r = r_c$) and (b) elastic stain and dislocation energies per unit length as a function of shell thickness of wurtzite InAs/InP core/shell NWs with a fixed core radius of 20 nm.

Figure 5.4(a) shows the change in the axial and tangential strain components at the interface of a core/shell NW with a fixed shell thickness of 14 nm and varying core radius in the range of 5 nm to 85 nm. The axial strain in the core decreases with increasing core radius, while it increases in the shell region. Weaker effects were observed for tangential strains. These results confirm that a thinner core can accommodate a higher degree of strain compared to a thicker one and therefore the critical shell thickness should be larger for a thinner core. The strain and dislocation energies are plotted in Fig. 5.4(b) as a function of shell thickness which intersect at $r_c$ = 63 nm, meaning that the critical shell thickness of an InAs/InP core/shell NW with radius of 63 nm is 14 nm.

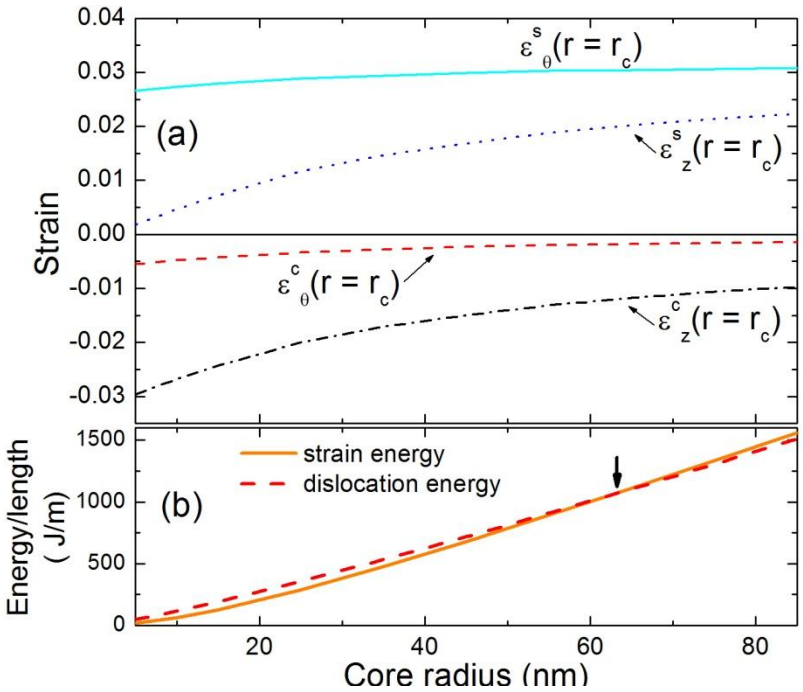


Figure 5.4. (a) Plot of the change in the interfacial strain components (at $r = r_c$) and (b) elastic strain and dislocation energies per unit length as a function of shell thickness of InAs/InP core/shell NWs with fixed shell thickness of 14 nm.

Figure 5.5 shows the dependence of the critical shell thickness on the core radius of different III-V core/shell NWs. Consistent with previous reports [17-19], the critical shell thickness tends to infinity for NWs with core radii smaller than a critical core radius. For NWs with core radii larger than the critical core radius, the shell thickness must be below a certain value to maintain coherency at the hetero-interface. The square and circle data points are experimental results which will be discussed later. For NWs with core radii larger than 100 nm, the critical shell thickness is independent of the core radius. The plot of the critical core radius ($r_{c0}$) and critical shell thickness for zincblende core/shell NWs with a particular core radius of 100 nm ($t_{c0}$) as a function of lattice mismatch between core and shell materials ($f_0$) is shown in Fig. 5.6. $r_{c0}$ is 21 nm for zincblende InAs/InP core/shell NWs (mismatch of 3.2 %) and drops to 2.9 nm for zincblende InAs/GaAs core/shell NWs (mismatch of 7.2 %). Similarly, $t_{c0}$ drops from 15.1 nm to 2.4 nm by increasing the mismatch from 3.2 % to 7.2 %. The graphs in Fig. 5.6 are fairly linear indicating the power law dependence of $r_{c0}$ and $t_{c0}$ on $f_0$. The fits to

the data were obtained by $r_{co} = 310 f_0^{-2.5}$ and $t_{co} = 130 f_0^{-2.0}$. We should note that $r_{c0}$ and $t_{c0}$ of a wurtzite InAs/InP core/shell NWs are 18.2 nm and 13.4 nm, respectively, which are smaller than the values obtained for zincblende ($r_{c0}$ = 21 nm and $t_{c0}$ = 15.2 nm) InAs/InP core/shell NWs. Similarly, in the case of wurtzite InAs/GaAs NWs, $r_{c0}$ and $t_{c0}$ are 2.3 nm and 2.2 nm, respectively, which are smaller than the corresponding values for zincblende structures.

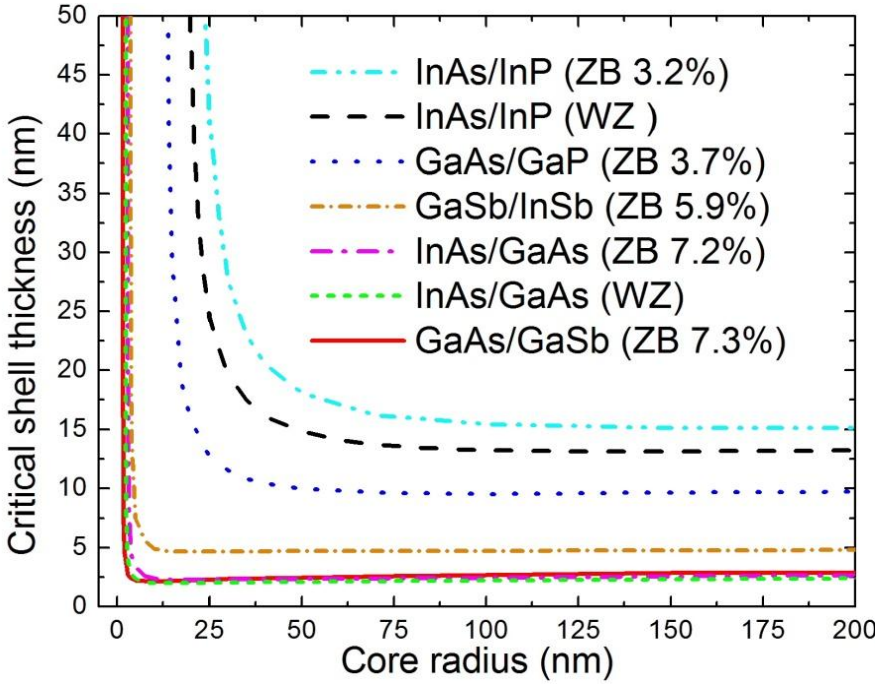


Figure 5.5. Plot of the calculated critical shell thickness as a function of core radius for different III-V core/shell NWs. Coherency is maintained for thicknesses below the curves.

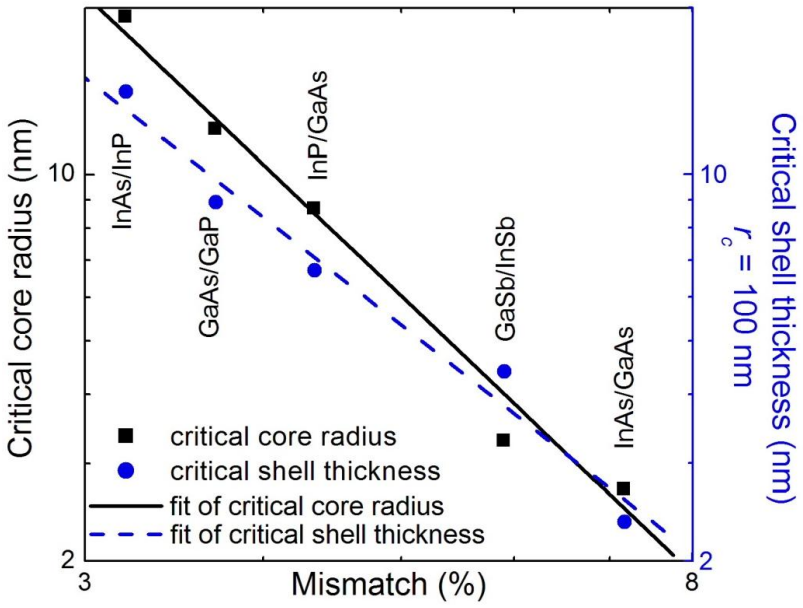


Figure 5.6. Plot of the critical core radius as a function of lattice mismatch between core and shell materials with zincblende structure (left). The critical shell thicknesses of core/shell NWs with a particular core radius of 100 nm are plotted on the right.

## 5.2 Experimental results: comparison with model

### 5.2.1 GaAs/GaSb and InAs/GaAs core/shell nanowires

Figure 5.7(a) shows an SEM image of GaAs/GaSb core/shell NWs (600 s shell growth time) taken at a 30° tilt angle from the NW growth direction. As expected, the GaAs core NWs grew along the [111]B direction, perpendicular to the substrate, and have hexagonal cross sections with {112} oriented facets. In all cases, GaSb forms islands on the core GaAs rather than a uniform, continuous shell. The thicknesses of the GaSb islands are 5-12 nm with lengths varying in the range of 20 to 80 nm. SEM images indicated the deposition of GaSb on all six facets of the core GaAs NWs. These islands are dome-shaped and do not show a well-defined periodicity.

Surface roughening of Ge/Si and Si/Ge core/shell NWs (4% mismatch) [86, 93] and the formation of InAs quantum dots on GaAs NWs have previously been reported

[94, 95]. The Stranski-Krastanov (S-K) mechanism is believed to be responsible for the observed surface roughening. In the S-K growth mechanism, the growth initiates by a 2-dimensional layer-by-layer mode and then switches to a 3-dimensional island growth mode driven by strain energy. A highly strained flat surface can relieve its energy by rearranging atoms via diffusion along the growing surfaces. This stress-driven mass transport is believed to be responsible for the surface roughening of highly mismatched hetero-interfaces [96]. More details on the GaAs/GaSb core/shell NW morphology can be found in ref. [97].

A bright field (BF) TEM image of a GaAs/GaSb core/shell NW with corresponding selected area diffraction pattern (SADP) viewed along a <12̲3> zone axis is shown in Fig. 5.7(b-c). Both core and shell are free of stacking faults and have zincblende crystal structure. The GaAs core has a diameter of 32 nm and the maximum GaSb shell thickness is 7 nm. Periodic Moiré fringes along the [111] growth direction with a 5.1 ± 0.4 nm spacing, are visible at the core region indicating the relaxation of the NW. The diffraction pattern (Fig. 5.7(c)) shows double spots in both the axial and radial directions. GaAs has a smaller lattice constant than GaSb and therefore the outer spots correspond to GaAs and the inner ones to GaSb. The relative average strain relaxation in a given direction can be calculated from the GaAs-GaSb spot separation divided by the average spot position, normalized by the GaAs-GaSb lattice mismatch (7.3%). From such analysis, we determined the relative axial and radial relaxation to be (94 ± 5) % and (92 ± 5) %, respectively. Also, the axial relaxation can be calculated from the Moiré fringe spacing. In the case of 100% relaxation, the minimum translational Moiré fringe spacing along an *hkl* direction ($D^{m}_{hkl}$) can be calculated by [41]:

$$D^{m}_{hkl} = \frac{d_{GaAs} d_{GaAs}}{d_{GaSb} - d_{GaAs}} \tag{5.10}$$

where $d$ is the planar spacing for a given *hkl* direction. In this case, $D^{m}_{111}$ is 4.5 nm. From the measured Moiré fringe spacing we found the axial relaxation to be (90 ± 5) % which is in good agreement with the value calculated from the diffraction spot spacing. The close agreement between the axial relaxation calculated from the diffraction patterns and Eq. (5.10) suggests that the Moiré fringes are translational. The periodic spots observed in the BF TEM image at the GaAs/GaSb interface correspond to edge dislocations along the {112} facets and perpendicular to the growth direction. Figure

5.7(d) shows a high resolution TEM image of the GaAs-GaSb interface. Periodic dislocations (indicated by dotted lines) with a Burger's vector along the growth direction with 5.1 ± 0.2 nm spacing ($D_e$) are visible. These edge dislocations relax the axial strain by a percentage given by $\frac{1}{0.073}\frac{b}{D_e}$ equivalent to (91 ± 2) %, in agreement with the value calculated from the diffraction pattern.

The degree of strain relaxation can also be calculated by measuring the GaAs and GaSb crystal plane spacing directly from the lattice image for a given direction. The (111) planar spacing for GaSb and GaAs (from Fig. 5.7(d)) are 0.350 ± 0.004 nm and 0.325 ± 0.004 nm, respectively, which also indicates 93 ± 3% axial relaxation for this NW.

Our observation of equal axial and radial relaxation indicates the presence of tangential (in the azimuthal direction) relaxation. The observed periodic edge dislocations with line directions perpendicular to the NW growth direction relax the axial strain but not the tangential strain. Tangential relaxation can occur by forming edge dislocations having a line direction with components parallel to the NW growth direction which we did not detect them in side-view TEM images. Tangential strain relaxation might also have occurred due to island formation. The curvature of these islands is larger in azimuthal directions compared to the axial direction suggesting an effective azimuthal strain relaxation via lateral expansion.

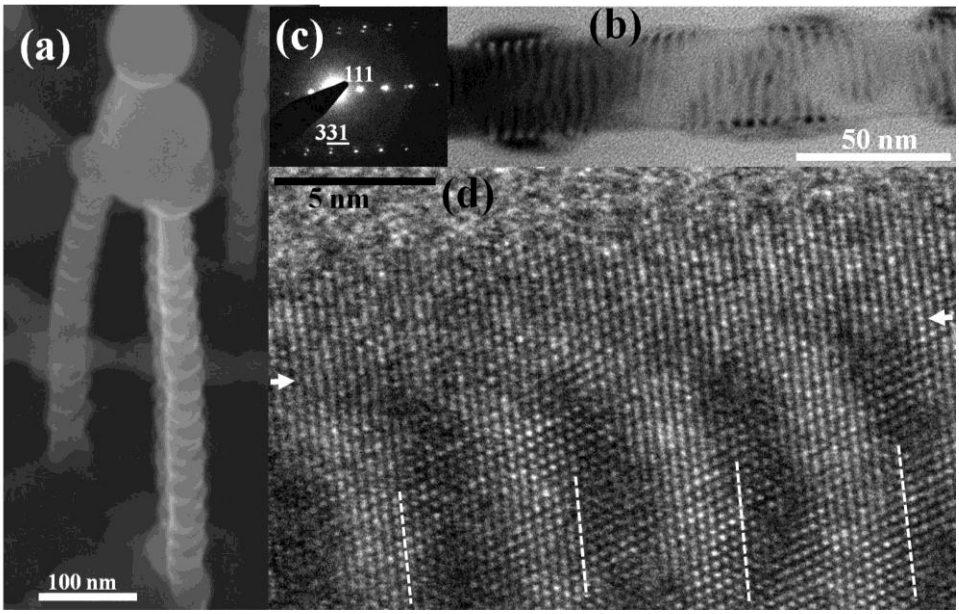


Figure 5.7. (a) SEM image (30° tilt angle) of GaAs/GaSb core/shell NWs, (b) BF TEM image of a GaAs/GaSb core/shell NW (c) with corresponding SADP along <12̲3> zone axis. (d) HRTEM image of the GaAs/GaSb interface. Arrows on both side of the HRTEM image indicates the GaAs/GaSb interface. The dotted lines indicate the extra planes in the GaAs region terminating at the interface.

To achieve a coherently strained GaAs/GaSb core/shell NW, we fabricated GaSb shells with a lower thickness (100 s growth time) compared to the NWs discussed above. Fig. 5.8(a) shows a NW with a core diameter of 31 nm and a maximum shell thickness of 1.8 nm. Modulations on the shell surface are clearly visible in the BF image. A corresponding SADP (Fig. 5.8(b)) along a <11̲2> zone axis shows a single set of spots indicating coherent material in both the axial and radial directions. The HRTEM image (Fig. 5.8(c)) clearly shows the formation of a fully strained GaSb QDs with a 1.8 nm thickness on a GaAs core.

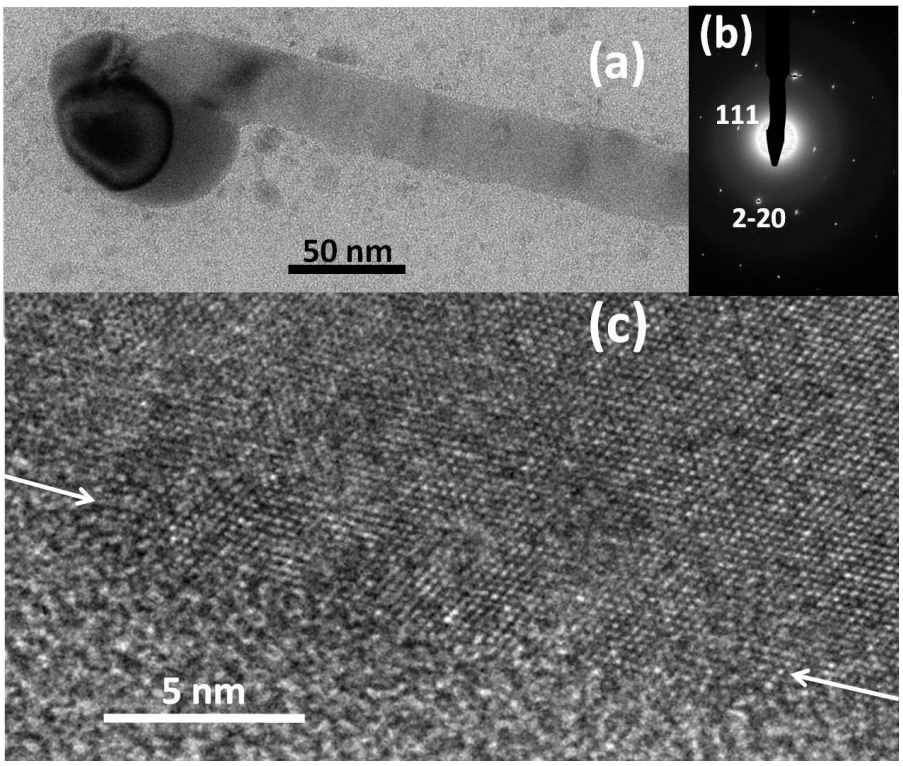


Figure 5.8. (a) BF TEM image, (b) associated SAD pattern along a <11$\underline{2}$> zone axis (b) and (c) HRTEM image of a GaAs/GaSb core/shell interface. The arrows in (c) indicate the approximate location of the GaAs/GaSb interface.

The TEM results obtained in this work for GaAs/GaSb core/shell NWs and the results previously reported for zincblende and wurtzite InAs/GaAs core/shell NWs [65] along with our theoretical predictions are plotted in Fig. 5.9. There is a close agreement between experimental results and our theoretical predictions. Our model predicts a slightly larger critical thickness for materials with zincblende structure than wurtzite structure. This is due to the smaller average values of the elastic constants, involved in the expression for the strain energy in zincblende materials compared with wurtzite materials.

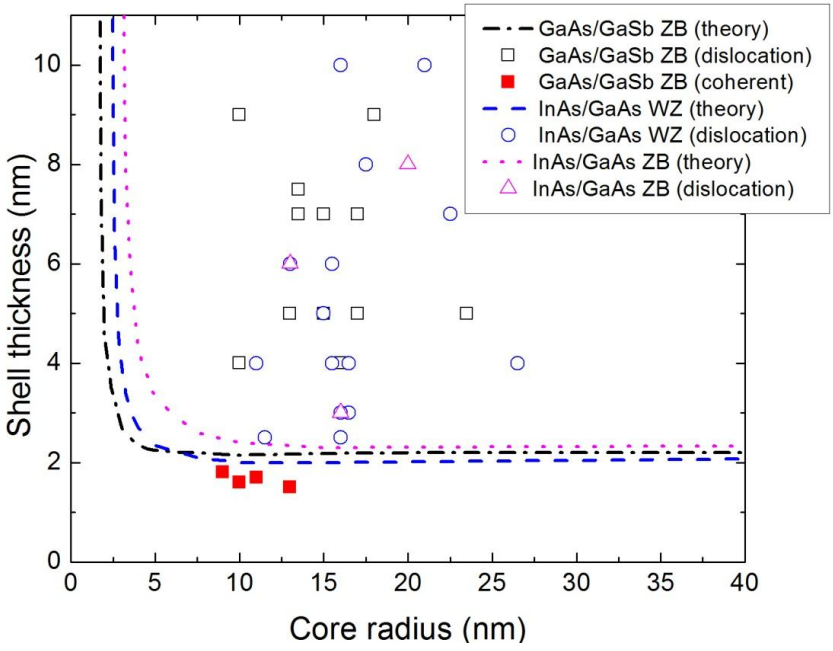


Figure 5.9. Plot of the calculated critical shell thickness as a function of core radius for zincblende GaAs/GaSb (dashed-dotted curve), zincblende InAs/GaAs (dotted curve) and wurtzite InAs/GaAs (dashed curve) core/shell NWs. The open and solid data points are the experimental results for NWs with and without dislocations detected, respectively. The experimental results for InAs/GaAs core/shell NWs are from ref [65].

### 5.2.2 GaAs/GaP core/shell nanowires

Figures 5.10(a) and (b) show a BF TEM image and corresponding SAD pattern (<11$\underline{2}$> sample orientation) of a zincblende GaAs/GaP core/shell NW with a core radius of 25 nm and s shell thickness of 13 nm. The shell thickness of 13 nm is larger than the predicted critical shell thickness (10 nm) for a NW with this core radius (see Fig. 5.5). The HRTEM image shown in Fig. 5.10(c) clearly indicates the insertion of an extra plane in the GaP shell. The observed dislocations have Burger's vectors along the NW growth direction and line directions perpendicular to the [111] growth direction. The average spacing of the observed edge dislocations is $D_e$ = 45 ± 4 nm giving an average relaxation

of $\frac{1}{0.037}\frac{b}{D_e}$, where $b$ is the size of the Burger's vector equal to $\frac{a_{GaP}}{\sqrt{3}}$, or 0.32 nm equevalent to 23 ± 2 %.

The solid and open circle data points plotted in Fig. 5.11 correspond to NWs free of dislocations and with dislocations, respectively, as a function of their shell thickness and core radius. According to the TEM analysis, the GaAs/GaP core/shell NWs with core radii in the range of 25 nm to 45 nm and shell thicknesses larger than 10 nm were relaxed. The thinner shells of 5-6 nm were found to grow coherently on GaAs NWs with radii of 22-25 nm. These experimental results are consistent with our numerical predictions. The previously reported GaAs/GaP core/shell NWs with core radius of 25 nm and shell thickness of 25 nm [77] should have relaxed according to our numerical predictions. Even though detailed TEM investigations were not carried out on the reported GaAs/GaP core/shell NWs, the presence of Moiré fringes in their BF TEM image [77] clearly indicates that the structure was partially relaxed.

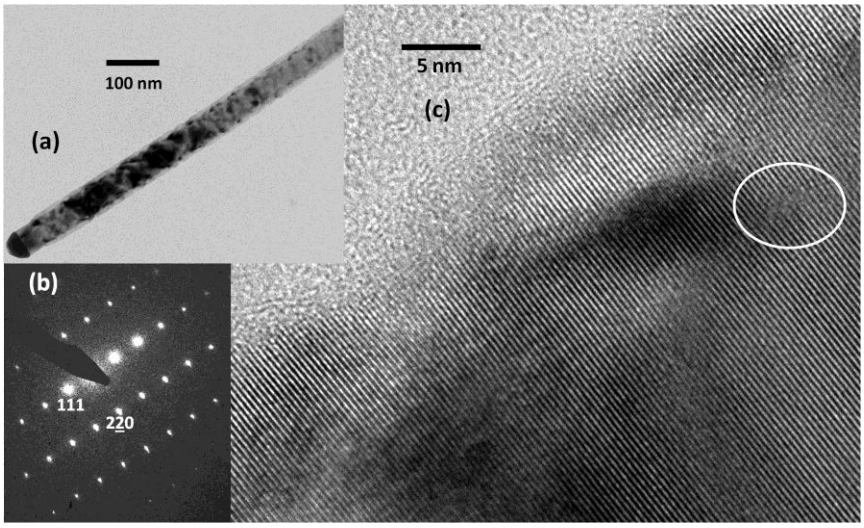


Figure 5.10. (a) BF TEM image and (b) corresponding SAD pattern of a GaAs/GaP core/shell NW with a core radius of 25 nm and shell thickness of 13 nm. (c) HRTEM image of the core/shell interface indicating the presence of an edge dislocation inside the white circle.

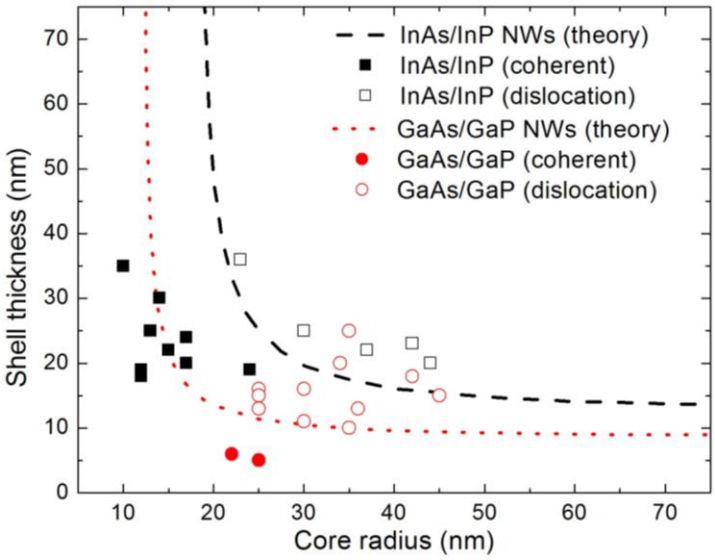


Figure 5.11. Plot of the calculated critical shell thickness as a function of core radius for wurtzite InAs/InP (solid line) and zincblende GaAs/GaP (dashed line) core/shell NWs. The open and solid data points are the experimental results for NWs with and without dislocations detected, respectively. The squares are for InAs/InP core/shell NWs while the circles are for GaAs/GaP NWs.

### 5.2.3 InAs/InP core/shell nanowires

Figure 5.12(a) shows a bright field (BF) TEM image of an InAs/InP core/shell NW with a core radius of 17 nm and shell thickness of 20 nm. Energy dispersive X-ray spectroscopy analysis was performed on these NWs and the formation of the shell and its thickness was confirmed (not shown here). The shell thickness is uniform along the NW growth direction, except for the tapered neck region which consists of InP formed during the shell growth via the VLS mechanism. Dark field (DF) TEM images taken using (0002) and ($\underline{2}$110) diffracted spots are shown in Fig. 5.12(b) and (c), respectively. These images clearly indicate that the NW is free of stacking faults and dislocations. The corresponding selected area diffraction (SAD) pattern, along the [0$\underline{1}$10] direction, from the middle part of the core/shell structure is shown in Fig. 5.12(d). The observed single set of spots indicate that the structure is coherent. A high resolution (HR) TEM image of

the InAs/InP interface is shown in Fig. 5.12(e) confirming that the structure is free of dislocations. The wurtzite structure of this NW can be inferred from the ABAB... stacking sequence along the [0001] growth direction. EDS analyses were performed (not shown here) and the formation of InP shell around InAs core NWs was confirmed.

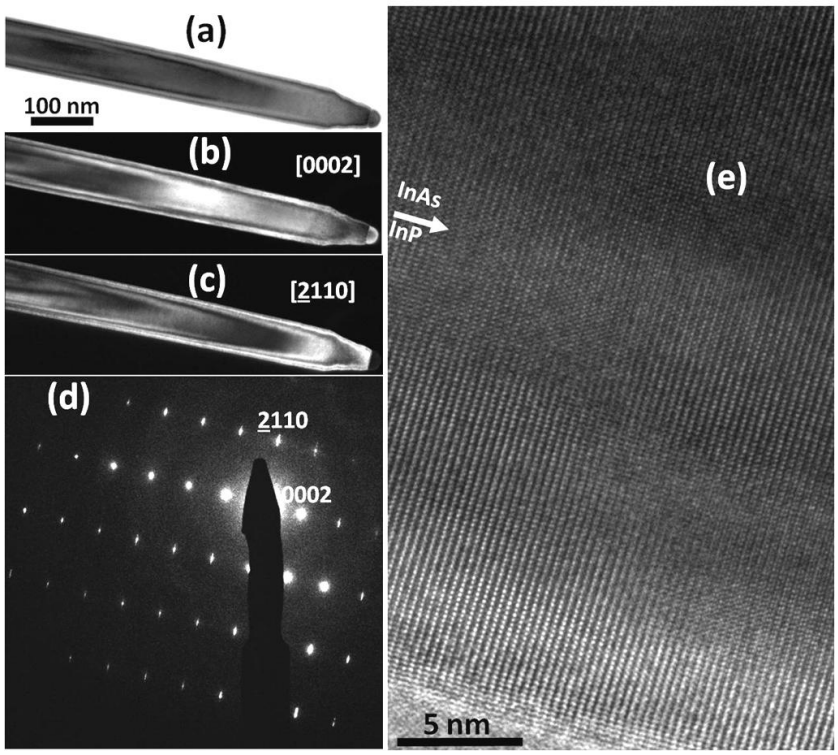


Figure 5.12. (a) Bright field and dark field TEM images of an InAs/InP core/shell NW taken by (b) (0002) and (c) ($\bar{2}$110) diffracted spots, (d) selected area diffraction pattern of the middle of the core/shell NW and (e) a high resolution TEM image of the InAs/InP interface. The arrow in (e) shows the approximate position of the InAs/InP interface.

Figure 5.13(a) and (b) show BF and (0002) DF TEM images of an InAs/InP core/shell NW with a core radius of 30 nm and shell thickness of 25 nm. The shell thickness of 25 nm is larger than the predicted critical shell thickness of 19 nm for a NW

with this core radius (see Fig. 5.5). The corresponding SAD pattern, indicating a (0$\underline{1}$10) sample orientation, is shown in Fig. 5.13(c). In all TEM images shown here, the incident electron beam was perpendicular to the NW growth axis. The observed contrast in Figs. 5.13(a) and (b) corresponds to the presence of edge dislocations at the core/shell interface perpendicular to the NW growth direction. Another example of a dislocation is shown in Fig. 5.13(d) for a NW with core radius of 37 nm and shell thickness of 22 nm and the corresponding SAD pattern is shown in Fig. 5.13(e). HRTEM image of the region indicated by a white square in Fig. 5.13(d) is shown in Fig. 5.13(f) indicating the insertion of an extra plane in the InP shell. The dislocations have Burger's vectors along the NW growth direction. The contrast observed between misfit dislocation pairs in these NWs may be related to a complete dislocation loop or other defect such as a stacking fault from partial dislocations. The observed contrast in Fig. 5.13 (a), (b) and (d) should not be confused with pre-exsiting basal plane {0001} stacking faults. In the case of a core/shell NW with stacking faults, the stacking faults propagate from the core into the shell. An example of a core/shell NW with stacking faults (core radius of 15 nm and shell thickness of 22 nm) is shown in Fig. 5.13(f). The strong parallel contrast is due to stacking faults that do not stop at the core/shell interface but propagate into the shell to the outer surface.

The observed dislocations in Fig. 5.13 have an average spacing ($D_e$) of 40 ± 7 nm. These edge dislocations relax the axial strain with respect to the lattice mismatch strain, 0.032, by a percentage given by $\frac{1}{0.032}\frac{b}{D_e}$, where $b$ is the size of the Burger's vector equal to $a/2$, or 0.35 nm, equivalent to (28 ± 4) %. This magnitude of axial strain relaxation, 0.009, is too small to be detectable in SAD patterns. No evidence of relaxation in other directions was detected either from images or SAD patterns.

The solid and open square data points plotted in Fig. 5.11 correspond to NWs free of dislocations and with dislocations respectively, as a function of their shell thickness and core radius. These experimental results are consistent with our numerical predictions for the critical geometries (solid and dotted lines). Our TEM results indicate that an InP shell with a thickness of 35 nm could be grown coherently on an InAs NW with a radius of 10 nm. Recently reported coherent InAs/InP core/shell NWs with core radius of 20 nm and shell thickness of 20 nm are consistent with our numerical predictions [98].

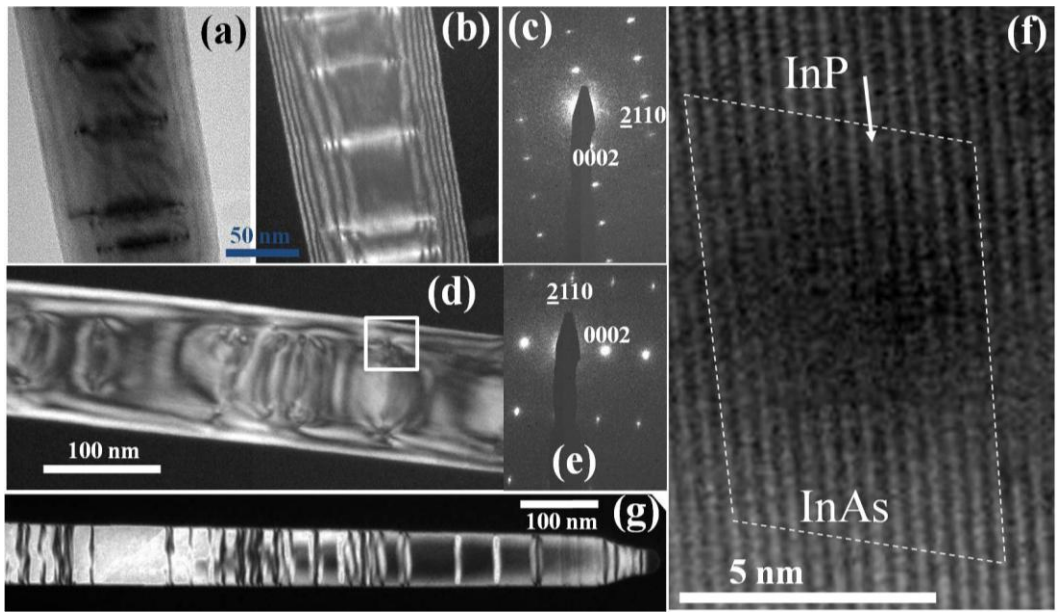


Figure 5.13. Examples of TEM investigations of strain relaxed wurtzite InAs/InP core/shell NWs (a) BF and (0002) DF TEM images for a NW with a core radius of 30 nm and shell thickness of 25 nm with corresponding SAD pattern in (c). (d) (2110) DF TEM image of another NW with a core radius of 37 nm and shell thickness of 22 nm with corresponding SAD pattern in (e) and HRTEM in (f). (g) (0002) DF TEM image of a NW with a core radius of 15 nm and a shell thickness of 22 nm. The observed contrasts in (a), (b) and (d) are perhaps due to the formation of loop dislocations, while the contrast in (g) is due to the formation of stacking faults.

Finally, the level of agreement between theory and experiment is remarkable considering that we have assumed no energy barrier for dislocation nucleation and motion via glide or climb processes. In addition, we have neglected any effect of facets on the strain distribution. The effects of these factors appear to be too small to be detectable. However, they may play an important role in the dislocation formation

mechanism [99]. We should note that, dislocation pairs or loops were not observed in zincblende GaAs/GaP and GaAs/GaSb core/shell NWs where dislocation formation by glide processes on oblique {111} planes have been reported in Si/Ge NWs with dimensions above the coherency limits [82].

In conclusion, a model to estimate the critical dimensions of core/shell NWs based on elasticity theory was presented. The numerical calculations were carried out for various III-V core/shell NWs. The theory was found to be consistent with experimental results previously reported for zincblende and wurtzite InAs/GaAs core/shell NWs and to the TEM results found in this work for wurtzite InAs/InP and zincblende GaAs/GaP and GaAs/GaSb core/shell NWs. All core/shell NWs studied here with dimensions above the coherency limits, predicted by the model, relax axially via the formation of edge dislocations at the core/shell interface with line direction perpendicular to the NW growth direction. Numerical results indicate that a uniform axial strain is the dominant component in the core region, while tangential strain that decreases quickly away from the heterointerface is the dominant component in the shell. This distribution of strain in a cylindrical geometry favours relaxation via edge dislocations (line directions perpendicular to the growth direction) for NWs of large core radius, relieving axial strain first.

## 6: NANOWIRE DOPING

Despite extensive progress in controlling morphology and improving crystal quality of semiconductor NWs [100, 101], control of their conductivity remains a challenging area for crystal growers. The VLS mechanism is the most commonly used approach for NW growth requiring a deposition of NPs, usually Au, onto the substrate prior to the NW growth to catalytically enhance the local growth rate. Dopant atoms may incorporate into the NWs via (1) diffusion through the dopant-NP solution into the NW and/or (2) diffusion along the NP/NW interface from the vapor phase into the NW. Also, dopant atoms may incorporate from the vapor phase into the layer grown on the facets of the NWs to form a doped shell around the core [102, 103].

For planar films, *n*-type doping of GaAs grown by MOVPE or molecular beam epitaxy (MBE) has commonly been achieved using silicon (Si) [104, 105]. However, Si doping of VLS-grown NW has only been feasible using MBE and the resulting wires had *p*-type conductivity [106, 107]. *n*-type doping of MOVPE grown GaAs nanowires using tetraethyl tin was demonstrated recently via a gold catalyzed VLS process [108]. Tellurium was only investigated as an *n*-type dopant for MBE-grown GaAs NWs [109] and was found to segregate at the surface of MBE-grown NWs resulting in tapered NWs.

P-type doping of Au-catalyzed GaAs NWs was only reported using Zn so far. Carbon is a desirable p-type dopant in GaAs films grown by MOVPE due to its low diffusion coefficient and high solubility in GaAs, which allows heavy doping above $10^{20}$ $cm^{-3}$ on (100) substrates [110], and the fabrication of sharp interfaces [111]. In the case of Au-catalyzed GaAs NWs, in addition to the low diffusion coefficient of carbon in GaAs, the immiscibility of carbon in Au [112] may also result in abrupt doping profiles. Carbon-halogens, such as carbon tetrabromide ($CBr_4$), are commonly used precursors to achieve C-doping in films grown by MOVPE. Carbon incorporates on the arsenic lattice site ($C_{As}$) as a shallow acceptor in GaAs with negligible $C_{Ga}$ incorporation. This low self-compensation is reported to lead to a higher Hall mobility for C-doped GaAs films compared to Zn-doped GaAs [113]. C-doping of GaAs NWs grown via the Au-catalyzed

VLS mechanism seems challenging due to the immiscibility of C in Au [112] as well as the very low diffusion coefficient of C in GaAs. Both factors would limit the incorporation pathway of C to its diffusion via the Au/NW interface (triple boundary) into the NW.

In this chapter, we present a detailed study of the effect of growth temperature, dopant precursor flow rate and NW diameter on GaAs NW conductivity and Au-NW diode characteristics. The work focuses on the use of two dopants, Te and C for *n*- and *p*-type doping, respectively. From these data we can infer information about the radial distribution of dopant in the nanowires, as well as estimates of the carrier concentration and the extent of surface depletion effects. We also demonstrate the fabrication of undoped-core/doped-shell GaAs NWs. The data presented in this chapter forms the basis for three papers published in Journal of Applied Physics [114, 115] and Applied Physics Letters [116].

To grow the samples studied in this chapter, a gold layer with a thickness of 3 nm was annealed at 600 °C resulting in NPs with sizes in the range of 50 nm to 1000 nm. Te-doped GaAs NWs were grown at a growth temperature, $T_g$, in the range of 380 ˚C to 480 ˚C with growth times of 300 s. TMGa and TBAs with molar flows of 15 μmol/min and 130 μmol/min were used as the group III and V. Te-doping was achieved during the NW growth by introducing DETe diluted in $H_2$ resulting in a total molar flow of 0.009 μmol/min and 0.08 μmol/min. The termination of the growth process, after switching off the group III and DETe sources, was carried out under TBAs flow (type A NWs) or without TBAs flow (type B NWs) to cool the samples to room temperature. The growth of core-shell GaAs NWs was achieved by growing the undoped core using TMGa for 300 s, and then using triethylgallium (TEGa) to grow the shell for 200 s with a DETe flow of 0.08 μmol/min. The sample was then cooled by switching off all the sources (type B termination).

C-doped GaAs NWs were fabricated on Zn-doped (111)B GaAs substrates ($p$ = $1.6 \times 10^{19}$ $cm^{-3}$) Trimethylgallium (TMGa) at a molar flow of 15 μmol/min and tertiarybutylarsine (TBAs) at a molar flow range of 16.5 to 165 μmol/min were used as the group III and V precursors, respectively, resulting in a V/III ratio of 1.1 to 11.0. C-doping was achieved by introducing $CBr_4$ during the growth with IV/III ratio of 0.015 to

0.15. Depending on the V/III ratio, the growth time was varied to achieve NWs with a minimum length of 1 μm, longer growth time is need for a lower V/III ratio.

## 6.1 Te-doping of GaAs nanowires

### 6.1.1 Core doping via VLS growth

In our electrical measurement configuration (see section 1.2), the contact between tungsten nanoprobe and Au alloyed NP was assumed to be ohmic with a negligible contact resistance. Therefore, the observed current-voltage (*I*-*V*) should depend on the interface properties of the NP/NW such as doping level of the NW and the composition of the NP (i.e. level of alloying of the Au NP with Ga). Figures 6.1(a) and (b) show high resolution TEM images of the top part of two Te-doped GaAs NWs ($T_g$ = 410 ˚C), one cooled under TBAs/$H_2$ ((type A) and the other under $H_2$ (type B), respectively. The type A NW has a neck region under the NP which is formed during the cooling down-period. According to the Au-Ga phase diagram, during the cool-down period, the equilibrium Ga concentration in Au/Ga alloyed NP decreases. Therefore, during cool-down the Ga present in the alloyed NP precipitates from the alloyed solution and reacts with TBAs at the NP/NW interface, which leads to the formation of the neck region[117] under the NP and also results in a partial depletion of Ga from the NP. NWs cooled under $H_2$ (type B) do not have a visible neck region under the NPs (Fig. 6.1(b)). Energy dispersive X-ray spectroscopy (EDS) line-scans taken across the middle of the NP into GaAs for the case of type A and type B NWs are shown in Fig. 6.1(c) and (d), respectively. It is clear that the ratio of the Ga to Au counts for type B NWs (0.27) is higher than that for type A NWs (0.14).

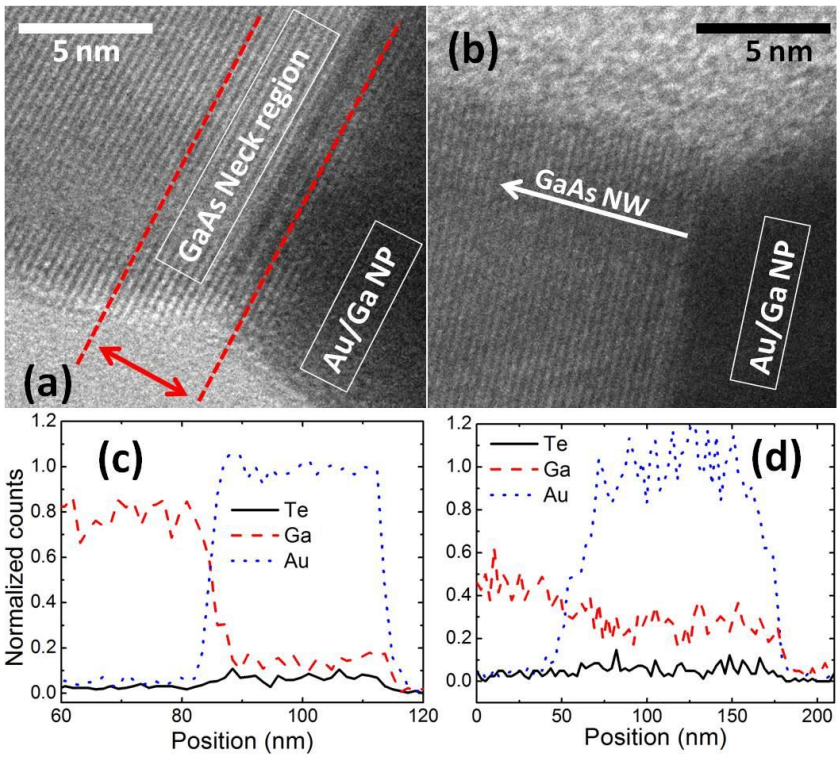


Figure 6.1. High resolution TEM images of the interface formed between the NP and a Te-doped NW for the case of postgrowth cooling under (a) TBAs/$H_2$ (Type A) and (b) $H_2$ (Type B). The DETe flow was 0.08 μmol/min with $T_G$ = 410 ˚C. (c) and (d) show EDS line-scans.

Figure 6.2 shows representative current density vs. applied voltage (*J-V*) characteristics of the type A and B NWs with the same doping level as well as a type B NW grown with a lower Te flow. Six to eight decades of linearity are observed in the forward bias semi-log curves. The reverse bias current density at -1 V is 100 mA/cm$^2$ corresponding to a reverse bias current of 8 pA at -1 V which was found to be independent of wire diameter. The reverse bias current is dominated by a shunt leakage resistor from our measurement circuit ($R_{lk}$ = 50-80 GΩ). Forward bias refers to applying a positive voltage to the Au electrode and thus the observed *J-V* curve indicates *n*-type NW conductivity. Both type A and B NWs grown with the same DETe flow tend to the same curve at high bias indicating a similar resistivity; however the slopes of the semi-log curves are different at low bias, indicating a difference in their ideality factors (*n*) and

barrier heights ($\varphi_{0b}$). The *J-V* curve of the NW grown with lower DETe flow saturates to a lower *J*, indicating a lower doping level.

The *I-V* characteristics of a metal-semiconductor diode, including the series ($R$) and shunt leakage resistance ($R_{lk}$), can be described by the following empirical equation [37], described in section 1.2:

$$I_{diode} = I_0\left(e^{\frac{q(V-IR)}{nk_\beta T}} - 1\right) + \frac{V}{R_{lk}} \tag{6.1}$$

with

$$I_0 = AA^*T^2 e^{\frac{-q\varphi_{b0}}{k_\beta T}} \tag{6.2}$$

where $I_0$ is the saturation current and is related to the cross-sectional area of the Au NP/NW interface ($A$), the Richardson's constant ($A^*$ = 8.16 A·cm$^{-2}$·K$^{-2}$ for *n*-GaAs and 74.4 A·cm$^{-2}$·K$^{-2}$ for *p*-GaAs) and the zero-bias barrier height ($\varphi_{b0}$). $R$ is dominated by the NW resistance in all cases studied here.

We obtained $n$, $\varphi_{b0}$ and the apparent NW resistivity ($\rho^* = \frac{R\pi r^2}{L}$, where $r$ and $L$ are the physical diameter and length of the NWs, respectively, and $R$ is determined as a fitting parameter) by fitting the semi-log *J-V* curves of at least 6 measurements of individual NWs for each sample with similar diameters ($d$ = 230 ± 20 nm) to Eq. 6.1. We should note that the true resistivity ($\rho$) is smaller than the $\rho^*$, due to sidewall depletion of the NWs. We determined the true resistivity from the analysis of $\rho^*$ as a function of NW diameter, as will be discussed later in this section. Typical fits are shown in Fig. 6.2 and the results are summarized in Table 6.1. We found a similar resistivity for the NWs grown with the same DETe flow (0.08 μmol/min), regardless of the difference in the cool-down procedure, corresponding to an estimated doping level ($n_d$) of 9 × 10$^{17}$cm$^{-3}$, based on published data for resistivity vs. electron concentration data for uncompensated GaAs films [118]. We neglected the effect of surface scattering on the carrier mobility as the NWs have large diameters. The resistivity of the NWs grown with lower DETe flow increased to (0.013 ± 0.001) Ω.cm corresponding to an estimated doping level of (1.5 ± 0.5) × 10$^{17}$ cm$^{-3}$. Based on the calculated true resistivity and the estimated carrier concentration, we estimate the carrier mobility to increase from (2800 ± 200) cm$^2$V$^{-1}$s$^{-1}$ to

(3200 ± 200) $cm^2V^{-1}s^{-1}$ by lowering the doping level from $9 \times 10^{17} cm^{-3}$ to $1.5 \times 10^{17} cm^{-3}$, assuming zero compensation ratio ($N_A/N_D$~0)

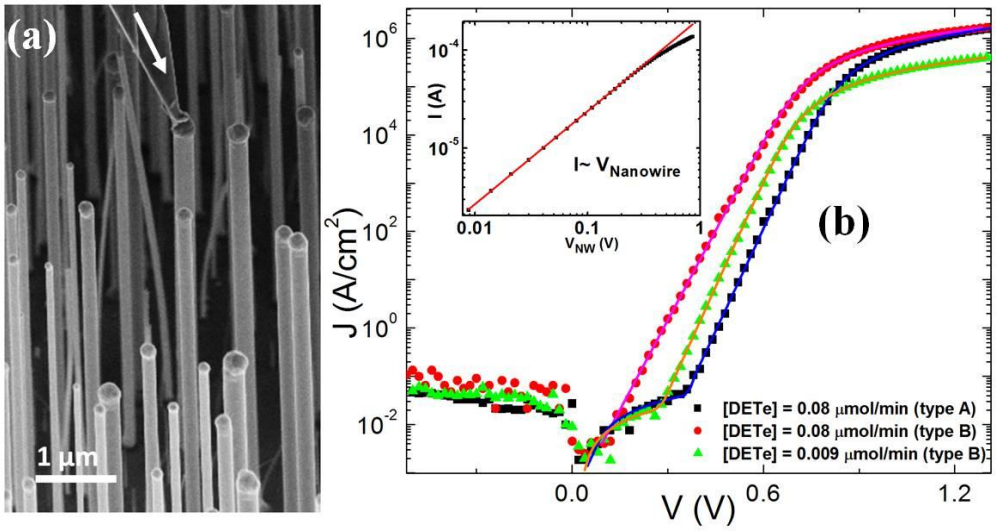


Figure 6.2. a) An SEM image of a nanoprobe (indicated by the arrow) contacting the Au end of a Te-doped GaAs NW grown at 410 ˚C. b) *J-V* characteristics of the type A (square data) and type B (circular and triangular data) Te-doped GaAs NWs (d = 230 ± 20 nm) with DETe flow of 0.08 μmol/min (square and circular markers) and a type B NW with the DETe flow of 0.009 μmol/min (triangular markers). Solid lines are the fit to Eq. 6.1. The inset shows current vs. NW voltage drop for a 220 nm NW after subtracting the fitted TFE voltage contribution due to the Au/n-GaAs junction voltage.

From Table 6.1, we see that cooling under $H_2$ (type B) results in a lower barrier height than cooling under TBAs (type A). The extracted barrier height of the type B NW with $n_d = 9 \times 10^{17}$ $cm^{-3}$ (0.63 ± 0.03 eV) is 0.16 eV lower than the barrier height of the type A NWs (0.79 ± 0.04 eV) with similar bulk doping level. The extracted barrier height of the type B ($n_d = 9 \times 10^{17}$ $cm^{-3}$) NW is in agreement with the reported value (~ 0.6 eV) for annealed planar Au/*n*-GaAs ($n_d = 2 \times 10^{18}$ $cm^{-3}$) [119], but lower than the reported values (0.89 eV with $n_d = 6 \times 10^{16}$ $cm^{-3}$) for evaporated planar Au/*n*-GaAs contacts [120]. There is evidence that alloying of Ga with Au can reduce the barrier height in planar

Schottky devices [119]. The higher extracted barrier height of the type A NWs is likely due to the lower Ga concentration of its NP with Ga compared to the type B NWs (see Fig. 6.1(c) & (d)). Another possibility is that the doping level in the neck region of the type A NWs is lower than the corresponding type B NWs, resulting in less thermally assisted tunnelling of the carriers through the junction, and an increase in the extracted value of the barrier height [121]. It is not clear however if the doping level of the neck region, which forms after switching off the DETe and TMGa sources, of the type A NW is similar to its bulk doping level or not. Even though the DETe is switched off during the cool-down step, Te stored in the NP can incorporate in the neck region.

The observed six-fold decrease of the doping level of the type B NWs from $9 \times 10^{17}$ $cm^{-3}$ to $1.5 \times 10^{17}$ $cm^{-3}$ with decreased DETe dopant results in an increase of the barrier height from 0.63 eV to 0.71 eV in agreement with a reduction in thermally assisted tunnelling at lower doping [121].

The observed *J-V* characteristic of the type B NW grown with the highest DETe flow (Fig. 6.2) fits to a single exponential curve, while the fitting of the other two *J-V* curves are the sum of both components in Eq. 6.1. Our measurement circuit has a shunt leakage resistance of ~ 50-80 GΩ. Type B NWs grown with the highest DETe flow have the lowest barrier height and thus the current passing through the interface (at low bias) is much higher than this leakage current. For NWs with higher barrier height at the NP/NW interface, at low bias, the current is limited by the leakage shunt resistance.

The observed deviation of $n$ from unity accompanied with $\varphi_{b0}$ lowering indicates that the thermally assisted carriers tunnel through the Au/*n*-GaAs interface near the top of the barrier, known as thermionic field emission (TFE) current ($I_{TFE}$). In *n*-GaAs with a doping concentration higher than $10^{17}$ $cm^{-3}$, TFE is known to be the common carrier transport mechanism.

The inset in Fig. 6.2 shows the log-log plot of the total current versus NW voltage drop for a 220 nm NW obtained by subtracting the voltage dropped at the Au/n-GaAs junction from the total applied voltage. The relationship is linear up to 0.4 V, confirming the absence of space charge limited current. At $V_{NW} > 0.4$ V, the differential resistance increases continuously to 6.5 kΩ at the highest applied voltage, indicating heating of the NW.

Table 6.1. Summary of the ideality factor, $n$, zero bias barrier height, $\varphi_{0b}$, true resistivity, $\rho$, and the estimated doping level, $n_d$, of the NWs discussed in Fig. 6.2. Type A NWs were cooled under TBAs vapor, while type B NWs were cooled under $H_2$ only.

| NW type | DETe flow (μmol/min) | $n$ | $\varphi_{0b}$ (eV) | $\rho$ (**Ω.c**m) | $n_d$ ( $cm^{-3}$) $\times 10^{17}$ |
|---|---|---|---|---|---|
| A | 0.08 | 1.20 ± 0.05 | 0.79 ± 0.04 | 0.0025 ± 0.0003 | 9 ± 1 |
| B | 0.08 | 1.34 ± 0.02 | 0.63 ± 0.03 | 0.0028 ± 0.0004 | 9 ± 1 |
| B | 0.009 | 1.18 ± 0.02 | 0.71 ± 0.02 | 0.013 ± 0.001 | 1.5 ± 0.5 |

We also investigated the effect of growth temperature on the Te-doping efficiency of the GaAs NWs. Figure 6.3 shows the *J-V* characteristics of Te-doped GaAs NWs at $T_g$ = 380 - 480 ˚C (type A NWs). We found that the ideality factor and barrier height are independent of the growth temperature. This indicates that the interface properties of the Au NP/NWs do not change with temperature. However, NWs grown at higher temperatures show a slightly higher conductivity. The true resistivity, determined from diameter-dependent analysis which will be discussed later, drops from 0.0034 ± 0.004 Ω.cm to 0.0018 ± 0.005 Ω.cm by increasing $T_g$ from 380 to 480 ˚C. The observed decreased in resistivity with temperature might be due to the increased solubility of Te in the Au/Ga alloy with increasing temperature [122]. However, we do not see a significant change in ideality factor and barrier height with temperature, which suggests that the Te-doping at the Au NP/NW interface is the same regardless of the temperature. Also, lateral growth increases with temperature and corresponds to 15 ± 4 nm at 480 ˚C. This can provide a conduction path parallel to the core region. This shell would be heavily doped and therefore would contribute to a slight reduction in the total resistance of the NWs. The thickness of this shell approaches zero close to the NP and is completely isolated from the NP by the neck region under the NP.

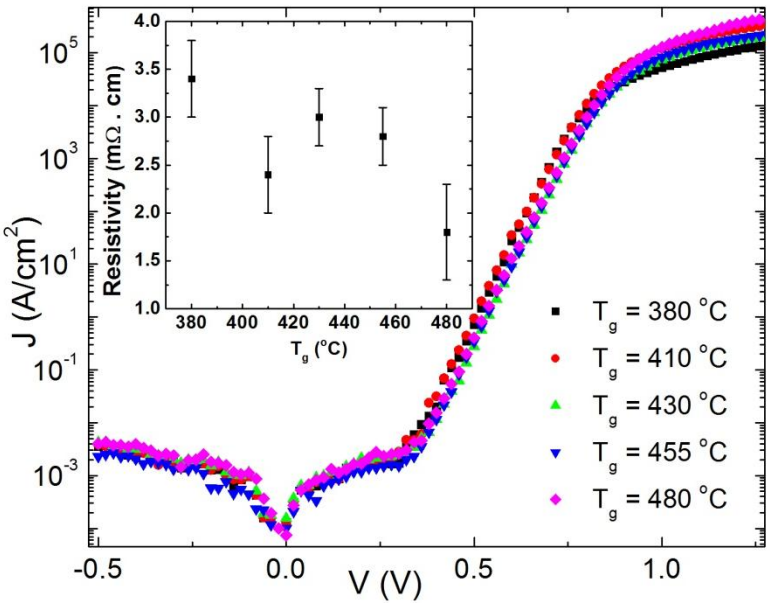


Figure 6.3. *J-V* characteristics of Te-doped GaAs NWs grown at different growth temperatures, $T_g$. Plot of true resistivity of the NWs as a function of $T_g$ is shown in the inset. The length of the NWs was between 4.5 μm to 5.2 μm.

Figure 6.4 shows representative current-density versus voltage (*J-V*) characteristics for 4 NWs grown at 410 ˚C and 2 NWs grown at 380 ˚C (type A with DETe flow of 0.08 μmol/min) with different diameters. All of the curves of the NWs grown at 410 ˚C collapse to the same curve at high forward bias indicating that they all have similar bulk conductivity. The results, obtained from fitting the curves for NWs grown at 410 ˚C to Eq. 6.1, give average $n$ and $\varphi_{b0}$ values of 1.26 ± 0.06 and 0.78 ± 0.04 eV, respectively. Similar values were obtained for NWs grown at 380 ˚C. However, the *J-V* curves of NWs grown at lower $T_g$ = 380 ˚C do not saturate at the same value indicating that the resistivity of the thinner NWs is higher than the thicker ones.

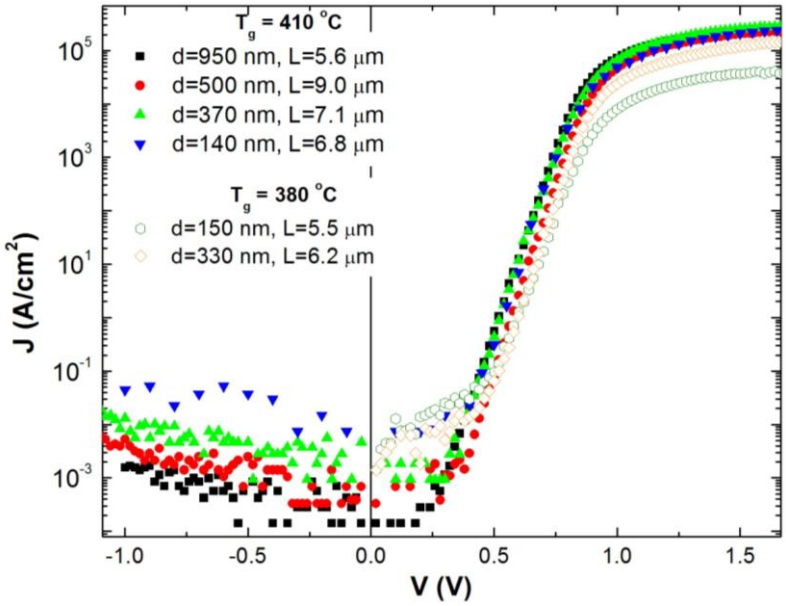


Figure 6.4. *J-V* characteristics of Te-doped GaAs NWs with different diameters grown at 410 ˚C and 380 ˚C with same DETe flow of 0.08 μmol/min.

We calculated the apparent NW resistivity, $\rho^*$, for a given NW diameter at different growth temperatures. Fig. 6.5 shows a plot of $\rho^*$ versus NW diameter for two growth temperatures, 380 ˚C and 410 ˚C. The data for growth at 410 ˚C shows that $\rho^*$ is independent of NW diameter. For the lower growth temperature at 380 ˚C, a dependence of $\rho^*$ on the diameter of the NWs is clearly detected. At higher growth temperatures, in addition to the VLS doping of the core, doping also occurs on the sidewalls through lateral growth, as discussed earlier, and this strongly suppresses the sidewall depletion of the NWs, leading to the observation of a diameter independent behaviour of the resistivity. We observed a similar independence for higher growth temperatures from 410 ˚C to 480 ˚C; but at 380 ˚C the absence of significant lateral growth should result in greater surface depletion of the NWs. The relationship between the calculated bulk resistivity ($\rho$) and $\rho^*$ of the NWs including the sidewall depletion (with length of $l_d$) of the NWs can be shown to be:

$$\rho^* = \frac{\rho}{1-2\left(\frac{l_d}{r}\right)+\left(\frac{l_d}{r}\right)^2} \tag{6.3}$$

The solid lines in Fig. 6.5 are fits to the data with $\rho$ = 0.0034 ± 0.004 and $l_d$ = 45 ± 5 nm for NWs grown at 380 ˚C and $\rho$ = 0.0025 ± 0.003 and $l_d$ = 8 ± 4 nm for NWs grown at

410 ˚C. The resistivity of the NWs grown at 380 ˚C corresponds to a doping level of (5.5 ± 1) × $10^{17}$cm$^{-3}$. Knowing the doping level of the NWs grown at 380 ˚C, the depletion width $l_d = \sqrt{\frac{2\varepsilon V_s}{qn_0}}$ where $q$, $\varepsilon$ and $V_s$ are the electron charge, permittivity and surface potential (~0.7 V) of the GaAs NW, respectively, was determined to be $l_d$ = 43 ± 4 nm in agreement with the fitting value. For the sample grown at 410 ˚C, the estimated carrier concentration is 9 × $10^{17}$ cm$^{-3}$ which should give a depletion thickness of $l_d$ ~ 30 nm, which is much larger than the fitted value of $l_d$ = 8 ± 4 nm. As previously discussed, we attribute this discrepancy to the formation of a very thin, highly doped surface layer. This layer should be heavily doped, as will be verified later, which can strongly suppress the depletion width.

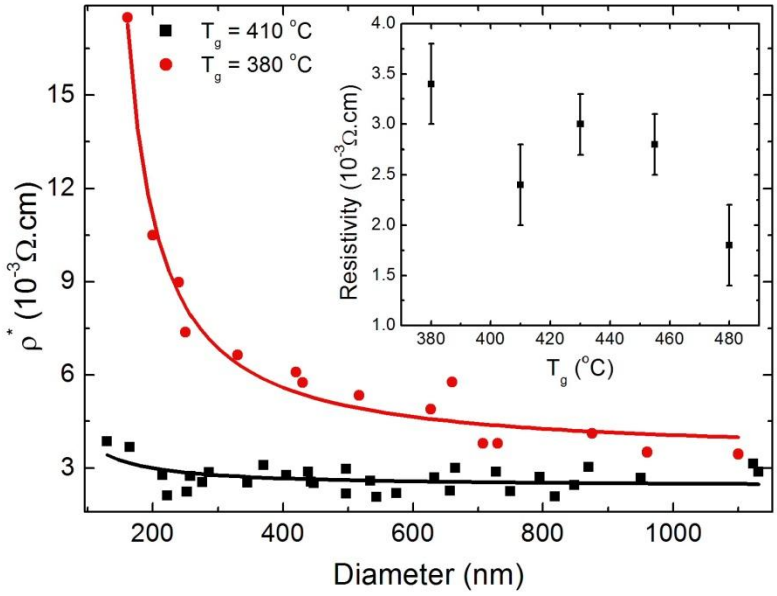


Figure 6.5. Plot of $\rho$* versus diameter (measured at the middle of each NW) of NWs grown at 410 ˚C and 380 ˚C. The inset shows the resistivity ($\rho$) of the NWs grown at different temperatures. The solid lines are fits based on Eq. 6.3.

### 6.1.2 Shell doping via VS growth

Figure 6.6 shows results for a core/shell, undoped/Te-doped (DETe = 0.08 μmol/min) GaAs NW. A bright field (BF) TEM image of such a NW (lower-right inset in Fig. 6.6) shows that it starts with a uniformly-thick and straight region followed by a long tapered section (1 micron) to the NP. The diameter of the NP is much smaller than the total width of the NW confirming the formation of a core-shell structure. The shell thickness of the NWs with a NP diameter of 280 ± 30 nm was determined to be 30 ± 5 nm. Also, a plan view SEM image of an undoped-core/Te-doped shell NW, shown in the lower right inset of Fig. 6.6, indicates the hexagonal cross section of the structure confirming that the shell growth occurs on all facets. A schematic structure of the NW is shown in the upper-left inset in Fig. 6.6. The undoped core (grown using TMGa) is surrounded by a Te-doped shell (grown by TEGa). The tapered section up to the NP is formed during the shell growth and its resistivity can be determined from the presented data in Table 6.1. After fitting the *J-V* curves of 8 NWs to Eq. 6.1 and subtracting the estimated resistance due to the tapered part, the apparent resistivity of the shell was determined to be 0.0005 ± 0.0002 Ω.cm with $\varphi_{0b}$ = 0.64 ± 0.03, and $n$ = 1.35 ± 0.04. This resistivity corresponds to a lower limit of the doping level of (6 ± 2) × $10^{18}$ $cm^{-3}$. The doping level of a thin Te-doped GaAs film with 300 nm thickness, grown on (001) GaAs substrate under similar conditions as the shell growth, was determined to be 1.8 × $10^{19}cm^{-3}$ according to Hall measurements. For a more accurate estimation of the doping level of the NW shell, the partial depletion of the shell should be considered. A doping level of 1.8 × $10^{19}cm^{-3}$ corresponds to a depletion width of 7.5 nm. Assuming a depletion width of 7.5 nm (from the sidewall surface and from the core/shell interface) for a NW shell, the resistivity is found to be (2.4 ± 0.8) × $10^{-4}$ Ω.cm, which corresponds to a doping level of (2 ± 1) × $10^{19}$ $cm^{-3}$. Planar Te-doping has a complex dependence on the growth orientation [123] which has been ignored in this work. Similar doping on {112}A and {112}B facts was assumed.

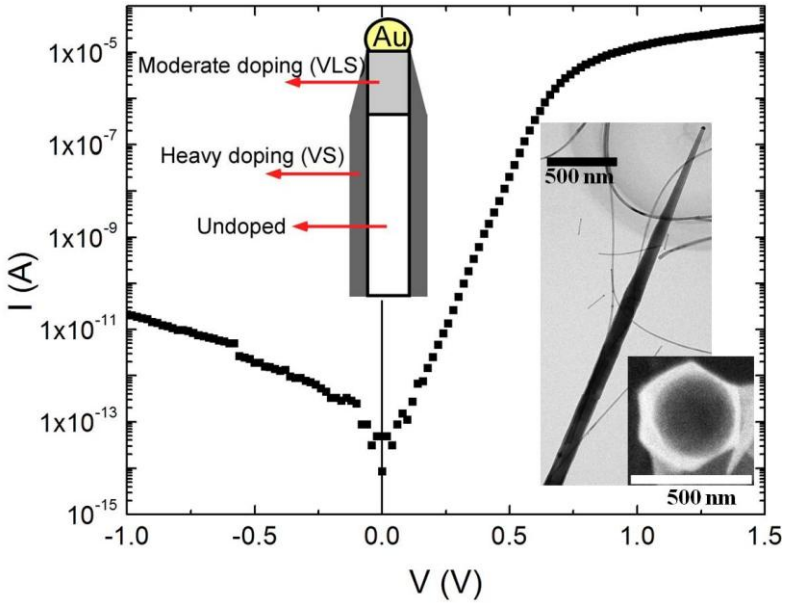


Figure 6.6. *J-V* characteristic of an undoped core/Te-doped shell GaAs NW. The lower right inset shows a BF TEM image and a planview SEM image and the upper left inset shows a schematic structure of an undoped-core/Te-doped shell GaAs NW.

## 6.2 C-doping of GaAs NWs

### 6.2.1 Core doping via VLS growth

The *I-V* characteristics of a C-doped GaAs NW (IV/III = 0.15) with a diameter of 490 nm grown with a V/III ratio of 11.0 is shown in Fig. 6.7. An SEM image of a nanoprobe contacting the Au tip of a C-doped GaAs NW is shown in the inset. The NWs are non-tapered and aligned perpendicular to the substrate surface along the (111)B direction. In contrast to the previous *n*-doped NWs, the *I-V* curve shows rectification at negative voltages (applied to the Au NP at the tip of the NW) indicating *p*-type conductivity of the NW. This can be easily understood by considering the band bending of p-GaAs forming an ideal Schottky contact with Au. In comparison, in the case of n-doped NWs, we previously observed rectification in positive bias. The observed

rectification here is due to the presence of a barrier at the Au NP/C-doped NW interface. The reverse bias current of the NW is in the range of 10 pA at 1 V.

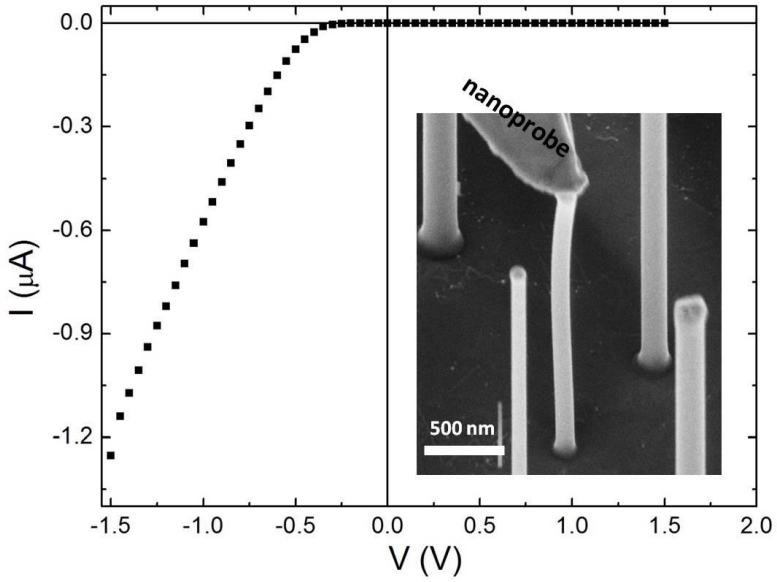


Figure 6.7. *I-V* characteristics of a C-doped GaAs NWs (IV/III= 0.15, d = 490 nm) grown at a V/III ratio of 11.0. The inset shows an SEM image of a nanoprobe contacting the Au tip of a C-doped GaAs NW.

The *J-V* curves of the NW discussed in Fig. 6.7 ($d$ = 490 nm) and a NW with $d$ = 170 nm (IV/III = 0.15, V/III = 11.0) are shown in Fig. 6.8. The data are plotted in both semi-log (Fig. 6.8(a)) and log-log (Fig. 6.8(b)) formats to emphasize the different transport mechanisms. The NW with $d$ = 490 nm shows excellent rectifying properties, with 4 decades of forward bias linearity in the semi-log plot, saturating at higher bias due to the resistance of the NW, while the NW with $d$ = 170 nm shows no linear region in the semi-log graph. However, in the log-log plot, the NW with $d$ = 170 nm shows 2 linear regions. At $V < 0.6$ V, $J$ is proportional to $V^2$, a characteristic of the space-charge-limited (SCL) current transport mechanism observed in fully depleted NWs [40]. At higher bias, $J$ is proportional to $V$, suggesting velocity saturation of the carriers; however the estimated field corresponding to the onset of a linear dependence is only ~2kV/cm. In high quality *p*-GaAs films, hole saturation velocity occurs at electric fields larger than

10 kV/cm [124]. Therefore, it remains an open question why we observe this linear behavior at a lower bias. The observed rectifying *I-V* characteristic for the NW with $d$ = 490 nm indicates that the NW is not fully depleted.

The solid line in Fig 6.8(a) shows a fit of the forward bias *J-V* curve to Eq. 6.1 which recovers the experimental data with an error less than 10%. Using Eq. 6.2 and the fitted value of $I_0$, we calculated $\varphi_{b0}$ to be 0.56 ± 0.04 eV. The ideality factor was determined to be 2.07 ± 0.06. An ideality factor of 2 typically indicates a generation recombination (GR) transport mechanism. The GR current depends on the distribution and energy levels of traps in the depletion region at the Au/NW interface and is known to be significant if the recombination centers are located close to the mid-gap. GR current is reported to be the dominant current transport mechanism in Au-based contacts to C-doped GaAs films with hole concentrations less than $5 \times 10^{18}$ cm$^{-3}$ [125]. From the extracted resistance of the NW, the *apparent* resistivity of the NWs ($\rho^* = \frac{R\pi r^2}{L}$, where $r$ and $L$ are the radius and the length of the NW) is calculated to be 3.9 ± 0.2 Ω.cm which corresponds to an estimated doping level of $5 \times 10^{15}$ cm$^{-3}$. This estimate is based on the published resistivity-carrier concentration data for bulk *p*-GaAs [118], neglecting carrier compensation and contribution of surface scattering to the resistance of the NWs, and ignoring sidewall depletion of the NWs. A better estimate of the actual doping level of the NWs requires knowledge of the dependence of the apparent resistivity on the NW diameter which will be presented later. From such an analysis, we estimated the actual doping level of this sample (IV/III = 0.15, V/III = 11.0) to be $N_A = (4 \pm 2) \times 10^{16}$ cm$^{-3}$ corresponding to a depletion width of $l_d = \sqrt{\frac{2\varepsilon V_s}{qN_A}}$ =130 nm, where $q$, $\varepsilon$ and $V_s$ are the electron charge, permittivity and surface potential (~0.45 V) [126] of the *p*-GaAs, respectively. Therefore, the NWs with diameter less than 260 nm should be completely depleted. This calculation is consistent with our observation of SCL current for NWs with $d$ < 290 ± 20 nm grown with IV/III = 0.15, V/III = 11.0.

In Fig. 6.8(b), we plotted the current versus voltage drop along the NW ($V_{NW}$), which was obtained by subtracting the voltage drop at the Au/NW interface from the applied voltage. The graph is linear in the entire range of measurements confirming the absence of SCL current.

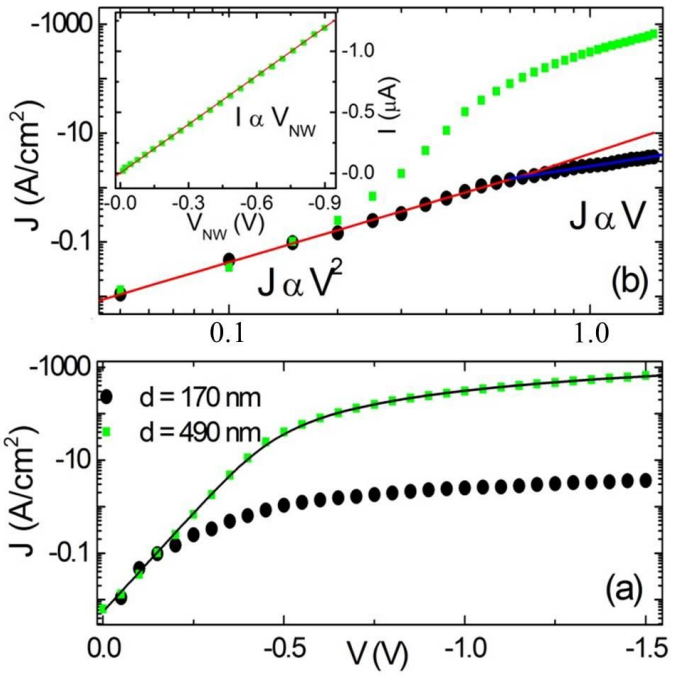


Figure 6.8. *J-V* characteristics of C-doped GaAs NWs (IV/III = 0.15, V/III = 11.0) with *d* of 170 nm (circle data points) and 490 nm (square data points) in semi-log scale (a) and log-log scale (b). The inset in (b) shows the $I$-$V_{NW}$ characteristic of the NW with *d* of 490 nm where $V_{NW}$ was obtained after subtracting the voltage drop at the Au NP/NW interface from the applied voltage.

Representative *I-V* characteristics of C-doped GaAs NWs (IV/III = 0.15) grown with a V/III ratio of 11.0, 3.3 and 1.1 are shown in Fig. 6.9. The conductivity of the NWs increases upon reducing the V/III ratio. At V/III ratios of 11.0 and 3.3, the *I-V* curves show rectification at negative voltage with a very low reverse bias current, while the NW at the lowest V/III ratio shows ohmic-like *I-V* characteristics evident the linear plot shown in the inset of Fig. 6.9. The switch from rectifying to ohmic-like *I-V* characteristic with decreasing V/III indicates a change in the carrier transport mechanism at the Au NP/NW junction.

The solid curves in Fig. 6.9 are fits of the forward bias *I-V* data to Eq. 6.1. The calculated $\varphi_{b0}$ and *n* are shown in Fig. 6.10(a) for V/III ratio in the range of 1.1 to 11.0.

The barrier height slightly drops from (0.56 ± 0.04) eV to (0.44 ± 0.04) eV by lowering the V/III ratio from 11.0 to 2.2 and then drops dramatically to (0.16 ± 0.02) eV at a V/III ratio of 1.1. The ideality factor remains at 2.05 ± 0.04 for NWs with V/III ratios in the range of 11.0 to 2.2 and then increases to 2.5 ± 0.3 for the lowest V/III ratio. An ideality factor of 2 indicates the dominance of the generation-recombination (GR) current transport mechanism for NWs with V/III ratio of 11.0 - 2.2. Di-carbon deep donor states are one possibility responsible for the observation of generation-recombination effects [127]. We attribute the observed barrier height lowering and increase in the ideality factor of the NW grown with a V/III ratio of 1.1 to the dominance of the field emission (FE) transport mechanism. FE current in Au-based contacts to C-doped GaAs films is reported to be the dominant transport mechanism at doping levels higher than $10^{19}$ $cm^{-3}$ [125]. At high doping levels, the depletion width at the metal-semiconductor becomes very narrow, which increases the direct tunnelling probability from semiconductor to metal. The tunnelling probability is determined by the parameter $E_{00} = 1.85 \times 10^{-11}[\frac{N_A(cm^{-3})}{(m^*/m_0)\varepsilon_r}]$ (eV) [118], where $N_A$ is the acceptor impurity concentration, $m^*$ (~0.072) is the hole effective mass, and $\varepsilon_r$ =13.2 is the relative permittivity of GaAs. As a fitting parameter, $E_{00}$ can be calculated from the value of $nk_\beta T$ obtained from the *I-V* curve fit, which gives a value of 0.065 eV. Therefore, the doping level of the NW with a III/V ratio of 1.1 is estimated to be $1.2 \times 10^{19}$ $cm^{-3}$. This value will be compared later to the doping level estimated from the resistivity of the NWs. From the extracted resistance of at least 5 NWs with $d$ = 200 ± 10 nm for NWs with V/III < 11 and $d$ = 380 ± 20 nm for V/III = 11, the apparent resistivity of the NWs is calculated and shown in Fig. 6.10(b). The apparent resistivity drops from (6 ± 1) Ω.cm to (0.010 ± 0.003) Ω.cm by lowering the V/III ratio from 11.0 to 1.1. Both arsenic and carbon compete to occupy the As lattice site during the growth process. Therefore, decreasing the TBAs flow will increase the C absorption rate and enhance the doping efficiency. Furthermore, reducing the TBAs flow results in a significant decrease in the axial growth rate of the NWs (Fig. 6.10 (c)) which in turn enhances the carbon incorporation efficiency.

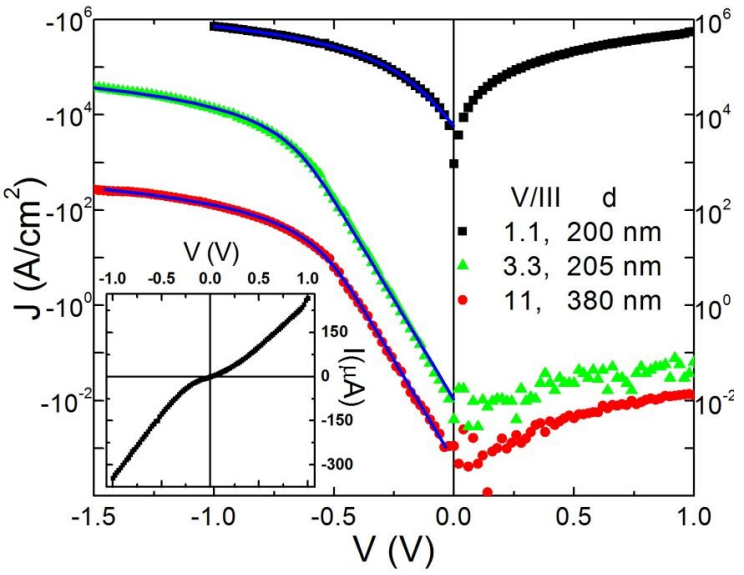


Figure 6.9. Semi-log *I-V* characteristics of C-doped GaAs NWs (IV/III = 0.15, length of 1 μm) as a function of V/III ratio. The inset represents the linear *I-V* curve of the C-doped GaAs NW grown with a V/III = 1.1 ratio.

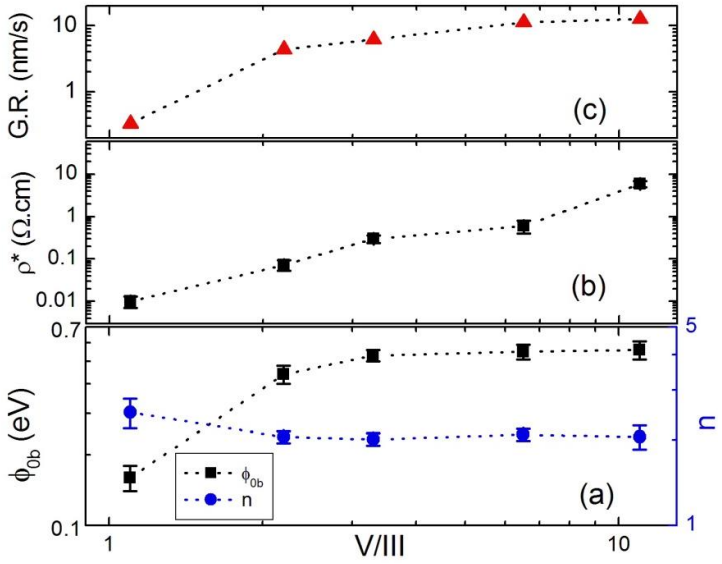


Figure 6.10. Plot of (a) the calculated barrier height and ideality factor, (b) the apparent resistivity and (c) axial growth rate of C-doped GaAs NWs (IV/III ratio = 0.15) as a function of V/III ratio. Diameters of the NWs were 200 ± 10 nm except that the NWs grown at a V/III ratio of 11.0 were $d$ =380 ± 20 nm.

Fig. 6.11 shows the dependence of the apparent resistivity on the diameter of the C-doped GaAs NWs grown with V/III of 1.1 and 6.5. Each of the $\rho^*$ values are an average of the measurements from at least 5 NWs in the related diameter range specified by the horizontal error bar. The apparent resistivity drops with increasing diameter up to 250 nm and then increases slightly for larger NWs. The initial drop in the apparent resistivity is due to the sidewall depletion of the NWs. The fit of the data (V/III = 6.5) to Eq. 6.3 is shown by a dashed curve in Fig. 6.11. The fitting curve agrees with the experimental data for NWs with diameters below 250 nm, but deviates for those with larger diameters. The observed diameter dependence of the apparent resistivity suggests non-uniform carbon incorporation for NWs with large diameters (d > 250 nm). Since carbon is not soluble in Au, carbon cannot incorporate into the GaAs NW via the Au NP. Also, carbon has a very low diffusion coefficient in GaAs and thus the incorporation of carbon by diffusion from the sidewalls into GaAs is unlikely. However, carbon may incorporate through the triple boundary at the Au/NW interface. To explain the $\rho^*$ vs $d$ behaviour observed in Fig. 6.11, we propose that carbon diffuses through the triple boundary (the boundary of the NP/NW interface) and incorporates uniformly into the GaAs NW up to a specific length (125 nm, inferred by comparing the fitting of the data to Eq. 6.3 and 6.4) from the sidewalls and then drops gradually in the regions close to the core of the NW. Diffusion through the triple boundary has been postulated to be one of the mechanisms for incorporation of As in GaAs NWs [128]. To fit the experimental data in Fig. 6.11, we add an empirical term ($\rho\alpha r$) to the numerator of Eq. 6.3 where $\alpha$ accounts for the lower incorporation of carbon in the regions close to the core:

$$\rho^* = \frac{\rho(1+\alpha r)}{1-2\frac{l_d}{r}+(\frac{l_d}{r})^2} \tag{6.4}$$

The solid curves in Fig. 6.11 show the best fits of the data using Eq. 6.4. The fitted curves recover the experimental data with $\rho$ = 0.10 ± 0.02 Ω.cm, $l_d$ = 58 ± 3 nm and $\alpha$ = (3 ± 0.3) × $10^{-3}$ $nm^{-1}$ for C-doped GaAs NWs with a V/III ratio of 6.5, and $\rho$ = 0.007 ± 0.002 Ω.cm, $l_d$ = 15 ± 3 nm and $\alpha$ = (1.4 ± 0.2) × $10^{-3}$ $nm^{-1}$ for C-doped GaAs NWs with a V/III ratio of 1.1. From this analysis, we estimated the doping level (of the uniformly doped region) of the C-doped GaAs NWs grown with V/III ratios of 1.1-11.0 from the extracted resistivity, and the data are shown in the inset of Fig. 6.11. The resistivity

drops from 0.6 ± 0.1 to 0.007 ± 0.002 Ω.cm by lowering the V/III ratio from 11.0 to 1.1 corresponding to an increase in the doping level from $(4 \pm 1) \times 10^{16}$ $cm^{-3}$ to $(1.0 \pm 0.3) \times 10^{19}$ $cm^{-3}$. The estimated doping level of the NW with a V/III ratio of 1.1 based on the extracted resistivity is in very good agreement with the estimated value based on the extracted value of the tunnelling probability. The increase of the C-doping level using $CBr_4$ with decreasing V/III ratio, keeping the group III flow constant, has commonly been observed in GaAs planar films [110]. This is due to the fact that both As and C compete for the same lattice site and reducing As flux would favour C incorporation in the As lattice site. Also, lowering the V/III ratio is reported to increase the unintentional C-doping of GaAs films via methyl radicals [129]. Our electrical measurements on undoped NWs grown with V/III of 11.0 and 1.1 all showed very low conductivity, indicating that unintentional carbon doping by methyl radicals is negligible in our case. Therefore, the observed increase of carbon incorporation in GaAs NWs by lowering the V/III ratio originates from the $CBr_4$ source.

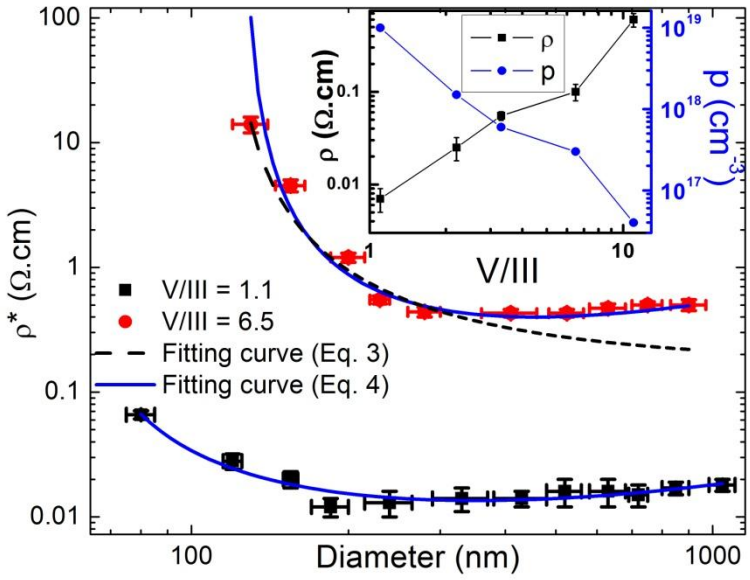


Figure 6.11. Plot of the apparent resistivity as a function of diameter of the C-doped GaAs NWs (IV/III = 0.15). The inset shows the resistivity and estimated hole concentration as a function of V/III (the lines in the inset are guide to the eyes).

The dependence of doping concentration on gas phase dopant supply is shown in Fig. 6.12. Increasing the IV/III ratio from 0.015 to 0.15 results in a decrease in the $\rho^*$ of the NWs ($d$ = 200 ± 10 nm) from 0.98 ± 0.09 to 0.010 ± 0.003 Ω.cm accompanied by a reduction of the barrier height from 0.53 ± 0.04 to 0.16 ± 0.02 eV. The calculated reduction in the resistivity with increasing dopant flow corresponds to an increase in the doping level from ~$2 \times 10^{17}$ cm$^{-3}$ to ~$1 \times 10^{19}$ cm$^{-3}$. The saturation of the doping level at IV/III > 0.075 is evident in Fig. 6.12, which might be due to the formation of deep level C-C dimers [130].

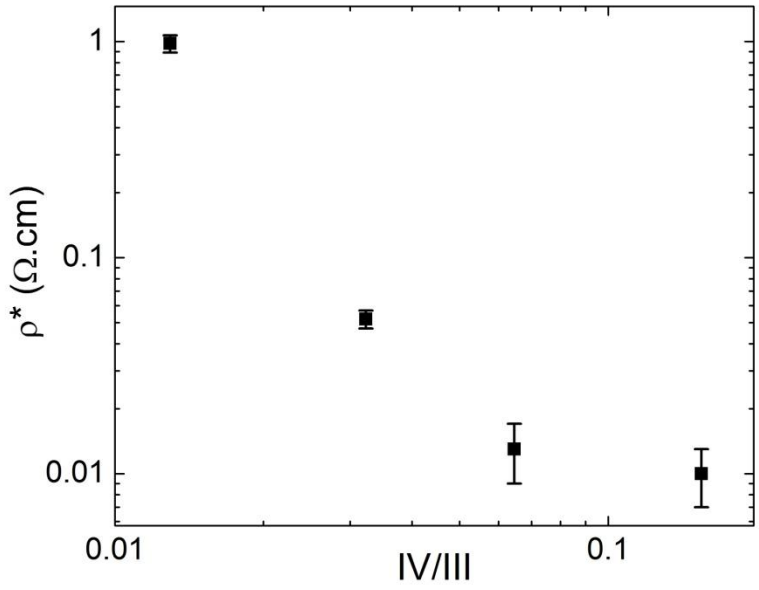


Figure 6.12. Plot of the apparent resistivity of C-doped GaAs NWs ($d$ = 200 ± 10 nm) as a function of IV/III ratio (constant group III precursor supply).

### 6.2.2 Shell doping via VS growth

Planview SEM images of undoped-core/C-doped shell GaAs NWs (IV/III of 0.015 and 0.075, V/III ratio of 7.0) are shown in Fig. 6.13(a-b). In most cases, the overall cross sections of the core/shell NWs are triangular or truncated triangular, while the cross section of the core region was hexagonal. This indicates that the shell growth only occurs on three facets of the core resulting in triangular or truncated triangular cross sections. The origin of triangular facet formation is not yet clear. The core has hexagonal cross section with {112}A (Ga-terminated) and {112}B (As-terminated) facets. $CBr_4$ might be more reactive on one type of facet than the other resulting in a stronger etching effect as was described in chaper 3. This could suppress the shell growth on three facets resulting in triangular cross sections. We should note that the outer facets are still {112} oriented and a rotation to {110} orientations was not observed.

A schematic structure and an SEM image of an undoped-core/C-doped shell NW are shown in Fig. 6.13(c) and (d), respectively. The undoped core (grown using TMGa) is surrounded by a C-doped shell (grown by TEGa). The tapered section up to the NP is formed during the shell growth and its resistivity was estimated to be 0.01 Ω.cm (IV/III ratio of 0.075) corresponding to an estimated doping level of ~ $10^{17}$ $cm^{-3}$. Electrical measurement on these NWs (by contacting the nanoprobe to the Au tip) was limited by the resistivity of the neck region. Therefore, to perform electrical measurements on the these NWs, the neck region (with lower conductivity) was removed using a Ga focussed ion beam inside the SEM chamber (Fig. 6.13(e)) and then the nanoprobe was contacted to the exposed new top of the NW (Fig. 6.13(f)).

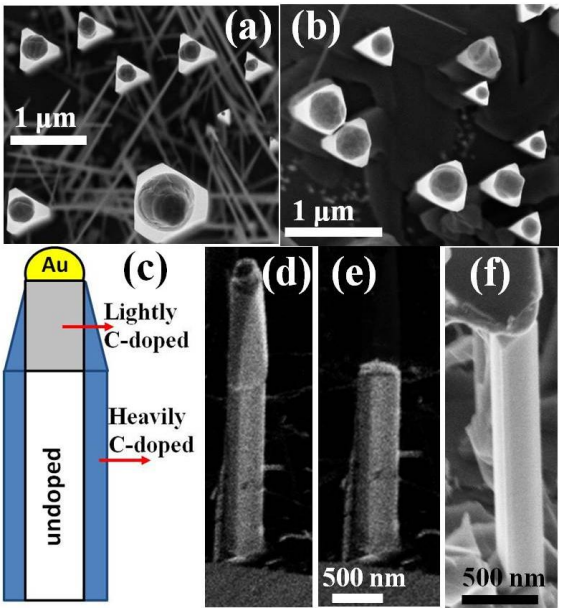


Figure 6.13. Planview SEM image of undoped-core/C-doped shell GaAs NWs grown using IV/III ratio of (a) 0.015 and (b) 0.075. (c) schematic structure and (d) SEM image (using gallium beam) of an undoped-core/C-doped shell GaAs NWs. e) SEM image after removing the neck region using focused ion beam (gallium beam) and (f) nanoprobe contacting the NW. TEGa flow was the same during the shell growth in Fig. (a) and (b).

Figure 6.14 shows *I-V* characteristics of an undoped-core/C-doped shell GaAs NW (core diameter of 100 nm and shell thickness of 30 nm) and a C-doped GaAs NW (diameter of 155 nm). For both these NWs, $CBr_4$ flow and V/III ratio were 0.075 μmol/min and 7.0, respectively. The *I-V* curve from a C-doped GaAs NW shows rectification at negative bias indicating *p*-type NW conductivity, while that of the core-shell NW showed ohmic behaviour. Rectification is due to the presence of a barrier at the Au NP/C-doped GaAs NW interface while an ohmic *I-V* curve for the core-shell NWs implies a very thin depletion width at the metal-semiconductor interface allowing tunneling of the carriers. Ohmic behaviour indicates a much higher doping level in the shell grown via direct vapor-solid growth compared to the C-doped NWs grown via VLS mechanism. Also, higher conductivity of the undoped-core/C-doped shell NWs than the C-doped core GaAs NWs could be inferred from the Cu electrodeposition experiments reported in ref. [131]. Since the contact area is not well defined in Fig. 6.13(e), we could not determine the resistivity of the undoped-core/C-shell NWs.

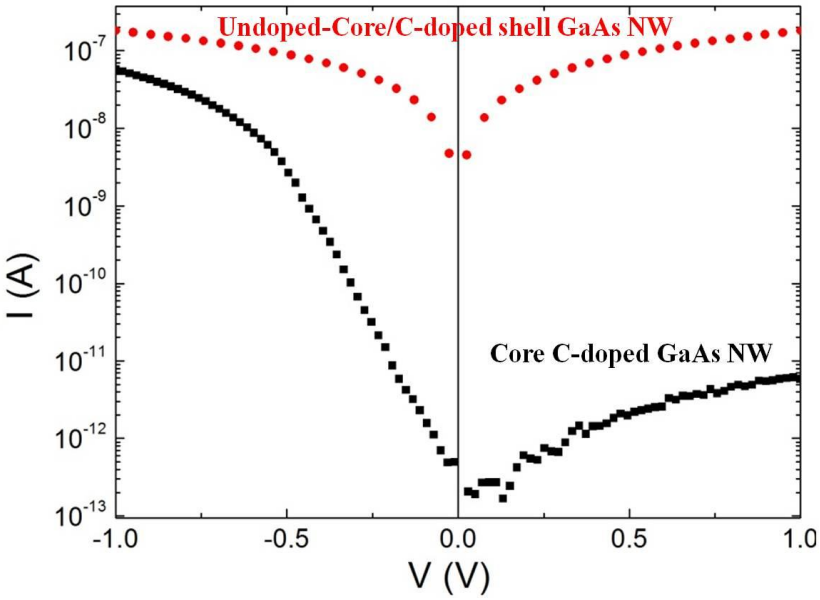


Figure 6.14. *I-V* characteristics of C-doped GaAs NWs with diameter of 155 nm (square data) and undoped-core/C-doped shell GaAs NWs (circle data), (undoped core (diameter 100 nm)/C-doped shell (thickness 30 nm)).

## 6.3 Undoped GaAs nanowires

In addition to the preceding doped NW results, we also fabricated undoped NWs at 410 ˚C for comparison with the doped NW properties. Figure 6.15 shows a *J-V* characteristic of an undoped GaAs NW on a log-log scale with a linear plot shown in the inset. The *J-V* curve shows power law characteristics, with ohmic behaviour at bias below 0.37 V, and quadratic behaviour at higher bias. This is typical of NWs depleted of carriers. At low bias, where the injected charge from the electrodes is insufficient, the current is dominated by thermally-generated free carriers within the NW in the depletion region of the Au NP/NW contact [132, 133]. By increasing the applied bias, the injected charge exceeds the thermally generated carrier concentration and space charge limited current (SCLC) becomes the dominant transport mechanism. The electrical measurements were performed on more than 30 NWs with diameter in the range of 120 nm to 400 nm. The apparent resistivity of the investigated undoped NWs, calculated from the ohmic region, varies widely from 1 Ω.cm to 200 Ω.cm, corresponding to an estimated residual doping level of $10^{14}$ to $10^{16}$ $cm^{-3}$, but in all cases is significantly higher than the resistivity of the doped NWs. We should note that higher order SCLC transport ($J \propto V^{\alpha}, \alpha > 2$) was also observed for some NWs, which is characteristic of the presence of traps in the depleted NWs [133], likely originating from the NW surface. This behaviour did not show any trend with NW diameter. It is important to note that the doped NWs showed consistent behaviour with a negligible dispersion on the measured resistivities.

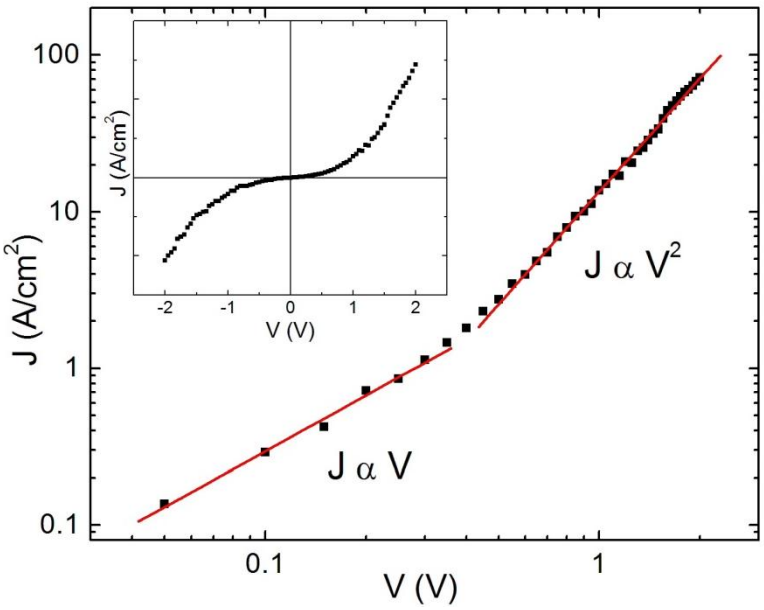


Figure 6.15. Log-log plot of a *J-V* characteristic (forward bias) of an undoped GaAs NW grown at 410 ˚C with $d$ = 180 nm and $L$ = 9 μm. The inset shows the corresponding linear *J-V* curve.

In summary, we demonstrated Te- (*n*-type) and C- (*p*-type) doping of Au-catalyzed GaAs NWs grown by MOVPE. Electrical measurements, using a nanoprobe within an SEM, showed rectifying *I-V* characteristics due to the formation of a junction at the NP/NW interface for moderate doping levels of $10^{17}$ - $10^{18}$ cm$^{-3}$. The polarity of the rectifying behaviour was consistent with the expectations for Au contacts on n- and p-type GaAs respectively. Increasing the growth temperature caused a slight decrease in the resistivity of the Te-doped NWs, as well as a strong effect on the dependence of the apparent resistivity on the diameter of the NWs. Te-doped NWs grown at $T_g$ > 410 ˚C show an independence of the apparent resistivity on the NW diameter, while those grown at 380 ˚C show an increase of the apparent resistivity with decreasing NW diameter. Lateral growth, with a doping level ~ $10^{19}$ cm$^{-3}$, and the consequent suppression of sidewall depletion of the NWs occur at higher $T_g$. Based on the diameter dependent analysis of the apparent resistivity and the observed solubility of the Te in Au alloyed NPs (via energy dispersive X-ray analysis), we conclude that Te incorporates into the NW by diffusing through the alloyed NP and the dopant distribution should be uniform

across the Au NP/NW. In addition, the Au NP/NW contacts show ideality factors close to unity indicating high quality of the Te-doped NW/metal contacts. Also, core/shell, undoped/Te-doped, GaAs NWs were demonstrated with very heavy doping of the shell region via direct VS growth.

In the case of C-doped NWs, control of carrier concentration was demonstrated by adjusting the gas phase dopant flow and V:III ratio. We showed that the transport mechanism switches from generation-recombination to field emission by increasing the doping level from $4 \times 10^{16}$ $cm^{-3}$ to $1 \times 10^{19}$ $cm^{-3}$. to field emission by increasing the doping level from $4 \times 10^{16}$ $cm^{-3}$ to $1 \times 10^{19}$ $cm^{-3}$. The observed dependence of the measured resistivity on NW diameter indicated a non-uniform dopant distribution across the NW. Based on the observed dependence of the apparent resistivity on the NW diameter and the immiscibility of C in Au, we propose that carbon is incorporated into NWs along the triple boundary at the Au NP/NW interface.

## 7: CONCLUSIONS AND FUTURE WORK

This thesis made several novel contributions to the understanding of III-V NW growth mechanisms as well as their structural and electrical properties. First, we explored the thermodynamic and kinetic aspects of the vapor-liquid-solid (VLS) growth mechanism. We presented a growth model to explain the dependence of the GaAs NW growth rate on diameter and group III partial pressure by accounting for incubation and Gibbs-Thomson effects. At low TMGa partial pressures, the incubation period is significant and longer for larger nanoparticles resulting in a lower overall growth rate for larger NWs. At high TMGa partial pressures, the incubation effect is negligible and thus the initial nucleus formation occurs quickly. Therefore, at high TMGa partial pressures, the overall growth rate is limited by the step flow growth rate of the initial nucleus which is lower for narrow NWs due to the Gibbs-Thomson effect.

We presented a systematic study to elucidate the role of Au nanoparticles (NPs) involved in the VLS growth of GaAs NWs. We observed a significant reduction in the activation energy of group III precursor decomposition in the presence of Au NPs indicating the catalytic role of the Au NPs. Furthermore, we showed that the presence of Au NPs greatly lowers the temperature over which gas phase diffusion limited growth is observed, providing strong evidence for the catalytic role of the Au NPs. Also, we investigated the kinetic aspects of GaAs NW growth using two different Ga precursors, TMGa and TEGa. We observed that lateral growth and NW tapering are strongly enhanced for the case of growth with the low temperature precursor TEGa. We showed that NW morphology is mainly determined by the competition between the VLS and VS growth mechanisms. We showed that by changing from TMGa to TEGa precursors, we can switch the growth mode of InAs/GaAs NWs from axial to core/shell heterojunctions. In this way precursor chemistry can be employed as a useful means to control the NW growth.

A dramatic reduction in tapering and lateral growth of TEGa-grown GaAs NWs was observed for NWs grown in the presence of $CBr_4$. This reduction in lateral growth

rate was accompanied by an increase in the axial growth of the NWs. This is mainly attributed to the parasitic reaction of $CBr_4$ on the free GaAs surfaces resulting in suppression of planar and lateral growth of the NWs. In addition, GaAs NWs grown in the presence of $CBr_4$ are free of stacking faults with zincblende structure, while NWs grown in the absence of $CBr_4$ are highly tapered and contain a high density of stacking faults. This work shows the remarkable effect of precursor chemistry on nanowire morphology.

A model to estimate the critical dimensions of core/shell NWs based on elasticity theory was presented. Numerical calculations were carried out for various III-V core/shell NWs. According to these calculations, in a coherent core/shell structure, tangential strain is the dominant component in the shell region and it decreases quickly away from the heterointerface, while axial strain is the dominant component in the core and is independent of the radial position. These strain distributions energetically favour the initial relief of axial strain in agreement with the experimental appearance of only edge dislocations with line directions perpendicular to the NW growth axis at the core/shell interfaces. Such dislocations were observed for wurtzite InAs/InP and zincblende GaAs/GaP and GaAs/GaSb core/shell NWs with dimensions above the calculated coherency limits. Good agreement with the model was also found for experimental results previously reported for zincblende and wurtzite InAs/GaAs core/shell NWs.

We demonstrated controlled Te- (*n*-type) and C- (*p*-type) doping, both core doping and shell doping, of Au-catalyzed GaAs NWs. Electrical measurements, using a nanoprobe within an SEM, showed rectifying *I-V* characteristics due to the formation of a junction at the NP/NW interface for moderate doping levels of $10^{17}$ - $10^{18}$ $cm^{-3}$. The ideality factors were slightly larger than unity indicating that thermionic field emission is the dominant transport mechanism through these contacts. Increasing the growth temperature from 380 to 480 ˚C caused a slight decrease in the resistivity of the Te-doped NWs, as well as a strong effect on the dependence of the apparent resistivity on the diameter of the NWs. Te-doped NWs grown at $T_g > 410$ ˚C show an independence of the apparent resistivity on the NW diameter, while those grown at 380 ˚C show an increase of the apparent resistivity with decreasing NW diameter which was attributed to depletion

by surface states. At higher $T_g$, there is a heavily doped shell on the core facets due to lateral growth which significantly suppresses the sidewall depletion of the NW sidewalls resulting in a lack of dependence of apparent resistivity on NW diameter. Based on the diameter dependent analysis of the apparent resistivity and the observed solubility of the Te in Au alloyed NP (via energy dispersive X-ray analysis), we conclude that Te incorporates into the NW by diffusion through the alloyed NP and the dopant distribution should therefore be uniform across the Au NP/NW interface during the growth. In addition, the Au NP/Te-doped NW contacts show ideality factors close to unity indicating high electrical quality of the Te-doped NWs. Also, undoped-core/Te-doped shell GaAs NWs, with a uniform shell growth on all facets of the core, were demonstrated with heavy doping of the shell region (~$10^{19}$ $cm^{-3}$) by direct VS growth. This indicates that the direct Te-doping efficiency for VS growth is more than an order of magnitude larger than Te-doping for VLS growth.

In the case of C-doped NWs, control of carrier concentration was demonstrated by adjusting the gas phase dopant flow in the range of $4 \times 10^{16}$ $cm^{-3}$ to $1 \times 10^{19}$ $cm^{-3}$. We showed that the Au/GaAs transport mechanism switches from the generation-recombination current mechanism to field emission by increasing the doping level from $4 \times 10^{16}$ $cm^{-3}$ to $1 \times 10^{19}$ $cm^{-3}$. Based on the observed dependence of the apparent resistivity on the NW diameter and the immiscibility of C in Au, we propose that carbon is incorporated into NWs along the Au NP/NW interface. We also investigated shell doping of GaAs NWs using $CBr_4$. We found that C-doped shell only grows on three facets of the core resulting in triangular or truncated triangular cross sections.

I suggest the following experiments in the future:

- Examine the optical quality of the NWs using photoluminescence (PL) measurements. By adjusting the V/III ratio and $T_g$ the growth conditions can be optimized to give NWs with high optical quality.
- Examine the optical and electrical properties of GaAs and InAs NWs passivated using GaP and InP, respectively. In addition to surface passivation, the presence of strain in these structures should result in interesting effects on the mobility and bandgap.

- Since carbon doping of the shell resulted in triangular cross sections, Zn should be investigated for p-type shell doping. However, carbon should be a good dopant to form axially abrupt p-n junctions. Zn has a memory effect in a MOVPE reactor and is soluble in the Au NPs and thus cannot give an abrupt doping profile.
- Perform electrical measurements (nanoprobe and ballistic electron emission microscopy (BEEM)) and possibly electron holography on radial and axial p-n junctions. From BEEM and holography measurements (the equipment is available in 4D labs at SFU), one should be able to determine the dopant distribution and interface abruptness in these structures.
- Use a $SiO_2$ layer with lithographically defined holes on a GaAs substrate to grow NWs using Au or Ga droplets. Deposition of Au can be performed using a mask after defining the holes. Ga droplet deposition can be achieved in an MOVPE reactor in Ga rich conditions. After growing the structure shown in Fig. 7.1, the measurement of the photovoltaic efficiency is possible by performing illuminated electrical measurements using a nanoprobe inside an SEM.

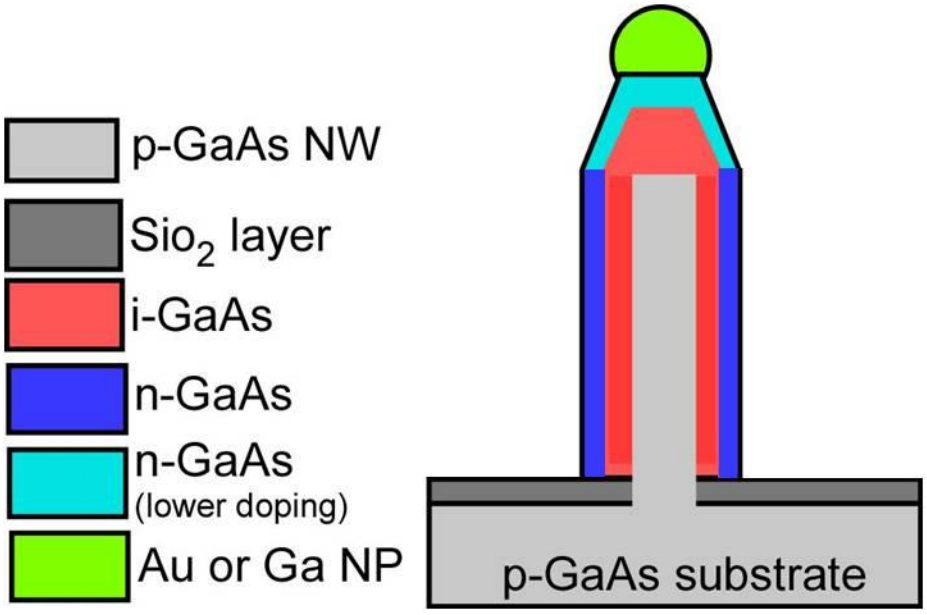


Figure 7.1. Schematic of a *p-i-n* structure for illuminated measurements inside an SEM using the W-nanoprobe.

**Bibliography**

[1] Y. Wu, Y. Cui, L. Huynh, C. J. Barrelet, D. C. Bell, and C. M. Lieber, *Nano Lett.*, 4:433, (2003).

[2] L. J. Lauhon, M. S. Gudiksen, D. Wang, and C. M. Lieber, *Nature*, 420:57, (2002).

[3] F. Qian, Y. Li, S. Gradecak, H.-G. Park, Y. Dong, Y. Ding, Z. L. Wang, and C. L. Lieber, *Nature Mater.*, 7:701, (2008).

[4] T. Martensson, C. P. T. Svensson, B. A. Wacaser, M. W. Larsson, W. Seifert, K. Deppert, A. Gustafsson, L. R. Wallenberg, and L. Samuelson, *Nano Lett.*, 4:1987, (2004).

[5] M. T. Björk, O. Hayden, H. Schmid, H. Reil, and W. Riess, *Appl. Phys. Lett.*, 90:142110, (2007).

[6] J. Wallentin et al., *Science*, 339:1057, (2013).

[7] G. Mariani, A. C. Scofield, C.-H. Hung, and D. L. Huffaker, *Nature Commun.*, 4:1497, (2013).

[8] P. Paiano, P. Prete, N. Lovergine, and A. M. Mancini, *J. Appl. Phys.*, 100:094305, (2006).

[9] S. A. Dayeh, Y. Eu, and D. Wang, *Nano Lett.*, 7:2486, (2007).

[10] S. Paiman, H. J. Joyce, Y. Kim, H. H. Tan, C. Jagadish, X. Zhang, Y. Guo, and J. Zou, *J. Phys. D*, 43:445402, (2010).

[11] K. Tomioka, J. Motohisa, S. Hara, and T. Fukui, *Nano Lett.*, 8:3475, (2008).

[12] M. T. Borgström, G. Immink, B. Ketelaars, R. Algra, and E. P. A. M. Bakkers, *Nature Nanotech.*, 2:541, (2007).

[13] K. Hillerich, K. A. Cick, M. E. Messing, K. Deppert, and J. Johansson, *Nano Res.*, 5:297, (2012).

[14] R. E. Algra, M. A. Verheijen, M. T. Borgstrom, L.-F. Feiner, G. Immink,W. J. P. van Enckevort, E. Vlieg and E. P. A. M. Bakkers, *Nature*, 456:369, (2008).

[15] J. W. Matthews, and A. E. Blakeslee, *J. Cryst. Growth*, 27:118, (1974).

[16] F. Glas, *Phys. Rev. B*, 74:121302, (2006).

[17] S. Raychaudhuri, and E. T. Yu, *J. Vac. Sci. Technol. B*, 24:2053, (2006).

[18] C. H. Haapamaki, J. Baugh, and R. R. LaPierre, *J. Appl. Phys.*, 112:124305, (2012).

[19] T. E. Trammell, X. Zhang, Y. Li, L.-Q. Chen, and E. Dickey, *J. Cryst. Growth*, 310:3084, (2008).

[20] J. G. Connell, K. Yoon, D. E. Perea, E. J. Schwalbach, P. W. Voorhees, and L. J. Lauhon, *Nano Lett.*, 13:199, (2012).

[21] M. I. D. Hertong, H. Schmid, D. Cooper, J.-L. Rouviere, M. T. Bjork, H. Reil, P. Rivallin, S. Karg, and W. Riess, *Nano Lett.*, 9:3837, (2009).

[22] G. B. Stringfellow, *Organometallic vapour-phase epitaxy: Theory and practice* , Academic Press, (1991).

[23] Q. Chen and P. D. Dapkus, *Electrochem. Soc.*, 138:2821, (1991).

[24] M. Tsuda, S. Oikawa, M. Morishita, and M. Mashita, *Jpn. J. Appl. Phys.*, 26**:**L564, (1987).

[25] C. A. Larsen, N. L Buchan, S. H. Li, and G. B. Stringfellow, *J. Cryst. Growth*, 102**:**103, (1990).

[26] M. G. Jacko and S. J. W. Price, *Can. J. Chem.*, 41**:**1560, (1963).

[27] M. Pristovsek, M. Zorn, and M. Weyers, *J. Cryst. Growth.*, 262:78, (2004).

[28] M. C. Paputa and S. J. W. Price, *Can. J. Chem.*, 57**:**3178, (1979).

[29] M. Yoshida, H. Watanabe, and F. Uesugi, *J. Electrochem. Soc.*, 132**:**677, (1985).

[30] G. Zimmermann, Z. Spika, T. Marschner, W. Stolz, E. O. Gobel, P. Gimmnich, R. Becker, J. Lorberth, A. Greiling, and A. Saltzmann, *Jpn. J. Appl. Phys.*, 35:2035, (1996).

[31] R. S. Wagner, W. C. Ellis, *Appl. Phys. Lett.*, 4:89, (1964).

[32] B. A. Wacaser, K. A. Dick, J. Johansson, M. T. Borgstrom, K. Deppert, and L. Samuelson, *Adv. Mater.*, 21:153, (2009).

[33] K.W. Kolasinski, *Curr. Opin. Solid State Mater. Sci.*, 10:182, (2006).

[34] C. T. Tsai, and R. S. Williams, *J. Mater. Res.*, 1:352, (1986).

[35] A. D. Kimberly, *Progress in Crystal Growth and Characterization of Materials*, 54:138, (2008).

[36] B. W. Dodson, *Appl. Phys. Lett.*, 53:394, (1988).

[37] M. Shur, *Physics of Semiconductor Devices*, Prentice Hall, New Jersey, (1990).

[38] N. F. Mott and R. W. Gurney, *Electronic processes in ionic crystals*, Oxford University press, (1940).

[39] A. Rose, *Phys. Rev.*, 97:1538, (1955).

[40] A. Alec Talin, F. Leonard, B. S. Swartzentruber, X. Wang, and S. D. Hersee, *Phys. Rev. Lett.*, 101:076802, (2008).

[41] D. B. Williams, and C. B. Carter, *Transmission Electron Microscopy*, Springer, New York, (2009).

[42] E. I. Givargizov, *J. Cryst. Growth*, 31**:**20, (1975).

[43] J. Johansson, C. P. T. Svensson, T. Mårtensson, L. Samuelson, and W. Seifert, *J. Phys. Chem. B*, 109:13567, (2005).

[44] Dubrovskii et al., *Phys. Rev. B*, 79:205316, (2009).

[45] C.-Y. Wen, J. Tersoff, M. C. Reuter, E. A. Stach, and F. M. Ross, *Phys. Rev. Lett.*, 105:195502, (2010).

[46] G. A. Bootsma, and H. J. Gassen, *J. Cryst. Growth*, 10:223, (1971).

[47] V. Schmidt, S. Sens, and U. Gösele, *Phys. Rev. B*, 75:045335, (2007).

[48] Y. Saito, *Statistical physics of crystal growth*, World Scientific, Singapore, (1996).

[49] C. Messmer, and J. C. Bilello, *Appl. Phys. Lett.*, 52:4623, (1981).

[50] I. V. Markov, *Crystal Growth for Beginners*, World Scientific, Singapore, (2003).

[51] Z. Chen, and C. Cao, *Appl. Phys. Lett.*, 88:143118, (2006).

[52] C. J. Adkins, *An Introduction to Thermal Physics*, Cambridge University Press, 2nd edition, (1987).

[53] S. A. Dayeh, and S. T. Picraux, *Nano Lett.*, 10:4032, (2010).

[54] M. Perez, *Scr. Mater.*, 52:709, (2005).

[55] V. Khorenko, I. Regolin, S. Neumann, W. Prost, and F.-J. Tegude, *Appl. Phys. Lett.*, 85:6407, (2004).

[56] O. Salehzadeh, and S. P. Watkins, *J. Cryst. Growth*, 325:5, (2011).

[57] D.H. Reep, S.K. Ghandi, *J. Electrochem. Soc.*, 130:675, (1983).

[58] M. Borgström, K. Deppert, L. Samuelson, W. Seifert, *J. Cryst. Growth*, 260:18, (2004).

[59] N. Viguier and F. Maury, *Appl. Phys. Lett*., 74:266, (1999).

[60] J. A. McCaulley, R. J. Shul, and V. M. Donnelly, *J. Vac. Sci. Technol. A*, 9:2872, (1991).

[61] H. K. Moffat and K. F. Jensen, *J. Cryst. Growth,* 77:108, (1986).

[62] K. Sladek, V.Klinger, J.Wensorra, M.Akabori, H.Hardtdegen, D.Grützmacher, *J. Cryst. Growth*, 312:635, (2010).

[63] P.Prete, F.Marzo, P.Paiano, N.Lovergine, G.Salviati, L.Lazzarini, T.Sekiguchi. *J. Cryst. Growth*, 310:5114, (2008).

[64] I. Regolin, D. Sudfeld, S. Lüttjohann, V. Khorenko, W. Prost, J. Kästner, G. Dumpich, C. Meier, A. Lorke, F.-J. Tegude, *J. Cryst. Growth*, 298:607, (2007).

[65] K. L. Kavanagh, I. Saveliev, M. Blumin, G. Swadener, and H. E. Ruda, *J. Appl. Phys.*, 111:044301, (2012).

[66] K. Hiruma, H. Murakoshi, M. Yazawa, T. Katsuyama, *J. Cryst. Growth*, 163:226, (1996).

[67] Z. Ikonic, G. P. Srivastava and J. C. Inkson, *Phys. Rev. B*, 48:17181, (1993).

[68] S. Vinaji, A. Lochthofen, W. Mertin, I. Regolin, C. Gutsche, W. Prost, F. J. Tegude, and G. Bacher, *Nanotech.*, 20:385702, (2009).

[69] O. Salehzadeh, and S. P. Watkins, *Nanotech.*, 22:165603, (2011).

[70] S. A. Stockman, A. W. Hanson, and G. E. Stillman, *Appl. Phys. Lett.*, 60:2903, (1992).

[71] H. J. Joyce, Q. Gao, H. H. Tan, C. Jagadish, Y. Kim, M. A. Fickenscher, S. Perera, T. B. Hoang, L. M. Smith, H. E. Jackson, J. M. Yarrison-Rice, X. Zhang and J. Zou, *Nano Lett.,* 9:695, (2009).

[72] V. G. Dubrovskii, N. V. Sibirev, J. C. Harmand, and F. Glas, *Phys. Rev. B*, 78:235301, (2008).

[73] H. Huang, X. Ren, X. Ye, J. Guo, Q. Wang, X. Zhang, S. Cai, and Y. Huang, *Nanotech.*, 21:475602, (2010).

[74] R. Leitsmann, and F. Bechstedt, *J. Appl. Phys.*, 102:063528, (2007).

[75] F. Glas, J.-C. Harmand, and G. Patriarche, *Phys. Rev. B*, 99:146101, (2007).

[76] S. Huang, and L. Yang, *Appl. Phys. Lett.*, 98:093114, (2011).

[77] M. Montazeri, M. Fickenscher, L. M. Smith, H. E. Jackson, J. M. Yarrison-Rice, J. H. Kang, Q. Gao, H. H. Tan, C. Jagadish, Y. Guo, J. Zou, M. Pistol, and C. E. Pryor, *Nano Lett.*, 10:880, (2010).

[78] Z. Zanolli, M.-E. Pistol, L. E. Froberg, and L. Samuelson, *J. Phys. Condens. Matter.*, 19:295219, (2007).

[79] X. Jiang, Q. Xiong, S. Nam, F. Qian, Y. Li, and C. M. Lieber, *Nano Lett.*, 7:3214, (2007).

[80] S. Manna, S. Das, S. P. Mondal, R. Singha, and S. K. Ray, I. *Phys. Chem.*, 116:7126, (2012).

[81] J. Gronqvist, N. Sondergaard, F. Boxberg, T. Guhr, S. Aberg, and H. Q. Xu, *J. Appl. Phys.*, 106:053508, (2009).

[82] S. A. Dayeh, W. Tang, F. Boioli, K. L. Kavanagh, H. Zheng, J. Wang, N. H. Mack, G. Swadener, J. Y. Huang, L. Miglio, K.-N. Tu, and T. Picraux, *Nano Lett.*, 13:1869, (2013).

[83] J. P. Hirth, and J. Lothe, *Theory of dislocations*, Wiley, New York, second edition, (1982).

[84] M. Y. Gutkin, I. A. Ovid'ko, and A. G. Sheinerman *J. Phys. Condens. Matter*., 15:3539, (2003).

[85] I. A. Ovid'ko, and A. G. Sheinerman, *Advances in Phys.*, 55:627, (2006).

[86] I. A. Goldthrope, A. F. Marshall, and P. C. McIntyre, *Nano Lett.*, 8:4081, (2008).

[87] Y. Chou, and J. Eshelby, *J. Mech. Phys. Solids*, 10:27, (1962).

[88] P. M. Anderson, and J. R. Rice, *J. Mech. Phys. Solids*, 35:743, (1987).

[89] R. M. Martin, *Phys. Rev. B,* 6:4546, (1972).

[90] S. C. Jain, M. Willander, and H. Maes, Semicond. *Sci. Technol.*, 11:641, (1996).

[91] W. F. Boyle, and R. J. Sladek, *Phys. Rev. B*, 11:2933, (1975).

[92] L.H. DeVaux, and F. A. Pizzarello, *Phys. Rev.*, 102:85, (1956).

[93] L. Pan, K.-K.Lew, J. M. Redwing, and E. C. Dickey, *Nano Lett.*, 5:1081, (2005).

[94] E. Uccelli, J. Arbiol, J. R. Morante, and A. F. i Morra, *ACS Nano*, 4:5985, (2010).

[95] X. Yan, X. Zhang, X. Ren, H. Huang, J. Guo, X. Guo, M. Liu, Q. Wang, S. Cai, and Y. Huang, *Nano Lett.*, 11:3941, (2011).

[96] H. Gao, and W. D. Nix, *Annu. Rev. Mater. Sci.*, 29:173, (1999).

[97] O. Salehzadeh, K. L. Kavanagh, and S. P. Watkins, *J. Appl. Phys.*, **113**:134309, (2013).

[98] S. G. Ghalamestani, M. Heurlin, L.-E. Wernersson, S. Lehmann, and K. A. Dick, *Nanotech.*, 23:285601, (2012).

[99] G. Perillart-Merceroz, R. Thierry, P.-H. Jouneau, P. Ferret, and G. Feuillet, *Appl. Phys. Lett.*, 100:173102, (2012).

[100] H. J. Joyce, Q. Gao, H. H. Tan, C. Jagadish, Y. Kim, X. Zhang, Y. Guo and J. Zou, *Nano Lett.*, **7**:921, (2007).

[101] H. Huang, X. Ren, X. Ye, J. Guo, Q. Wang, Y. Yang, S. Cai and Y. Huang, *Nano Lett.*, 10:64, (2010).

[102] L. Rigutti, A. D. L Bugallo, M. Tchernycheva, G. Jacopin, F. H. Julien, G. Cirlin, G. Patriarche, D. Lucot, L. Travers, and J.-C. Harmand, *J. Nanomater.*, 2009:435451, (2009).

[103] E. Tutuc, J. O. Chu, J. A. Ott, and S. Guha, *Appl. Phys. Lett.*, 89:263101, (2006).

[104] T. Kikkawa, H. Tanaka, and J. Komeno, *J. Electron. Mater.*, 21:305, (1992).

[105] J. H. Neave, P. J. Dobson, J. J. Harris, P. Dawson and B. A. Joyce, *Appl. Phys. A*, 32:195, (1983).

[106] M. Hilse, M. Ramsteiner, S. Breuer, L. Geelkaar, and H. Riechert, *Appl. Phys. Lett.*, 96:193104, (2010).

[107] B. Ketterer, E. Mikheev, E. Uccelli, and A. F. I Morral, *Appl. Phys. Lett.*, 97:223103, (2010).

[109] C. Gutsche, A. Lysov, I. Regolin, K. Blekker, W. Prost, and F.–J. Tegude, *Nano Scale Res. Lett.*, 6:65, (2011).

[109] J. Caram, C. Sandoval, M. Tirado, D. Comedi, J. Czaban, D. A. Thomson, and R. R. LaPierre, *Nanotech.*, 21:134007, (2010).

[110] C.-S. Son, S.-I. Kim, B.-D. Min, Y. Kim, E. K. Kim, S.-K. Min, and I.-H. Choi, *Jpn. J. Appl. Phys.*, 35:6562, (1996).

[111] N. Kobayashi, T. Makimoto, and Y. Horikoshi, *Appl. Phys. Lett.*, 50:1435, (1987).

[112] T. B. Massalski, H. Okamoto, P. R. Subramanian, L. Kacprzakm, *Binary alloy phase diagrams* (2$^{th}$ edition, ASM International: Metals Park, OH, 1990) pp 346.

[113] H. D. Chen, C. Y. Chang, K. C. Lin, S. H. Chan, M. S. Feng, P. A. Chen, C. C. Wu, and F. Y. Juang, *J. Appl. Phys.*, 73:7851, (1993).

[114] O. Salehzadeh, K. L. Kavanagh, and S. P. Watkins, *J. Appl. Phys.*, 112:054324, (2012).

[115] O. Salehzadeh, K. L. Kavanagh, and S. P. Watkins, *J. Appl. Phys.*, 112:094323, (2012).

[116] O. Salehzadeh, K. L. Kavanagh, and S. P. Watkins, *Appl. Phys. Lett.*, 99:182102, (2011).

[117] A. L. Persson, M. W. Larsson, S. Stenström, B. J. Ohlsson and L. R. Wallenberg, *Nature Mater.*, 3:677, (2004).

[118] S. M. Sze, *Physics of Semiconductor Devices*, Wiley, New York, (1985).

[119] A. K. Sinha, and J. M. Poate, *Appl. Phys. Lett.*, 23:666, (1973).

[120] J. R. Waldrop, *J. Vac. Sci. Technol. B*, 2:445, (1984).

[121] M. K. Hudait and S. B. Krupanidhi, *Physica B*, 307:125, (2001).

[122] D. Mouani, G. Morgant and B. Legendre, *J. Alloys and Compounds.*, 226:222, (1995).

[123] R. Bhat, C. Caneau, C. E. Zah, M. A. Koza, W. A. Bonner, D. M. Hwang, S. A. Schwarz, S. G. Menocal and F. G. Favire, *J. Cryst. Growth*, 107:772, (1991).

[124] V. L. Dalal, A. B. Dreeben, and A. Triano, *J. Appl. Phys.*, 42:2864, (1971).

[125] K. S. Sandhu, A. E. Staton-Bevan, and M. A. Crouch, *Mater. Sci. Technol.*, 11:1083, (1995).

[126] L. G. Meiners, *Appl. Phys. Lett.*, 33:747, (1978).

[127] K. H. Tan, S. F. Yoon, Q. F. Huang, R. Zhang, and Z. Z. Sun, *Phys. Rev. B,* 67:035208, (2003).

[128] K. A. Dick, *Prog. Cryst. Growth Characterization*, 54:138, (2008).

[129] M. Longoa, R. Magnaninia, A. Parisinia, L. Tarriconea, A. Carbognania, C.Bocchib, and E. Gombia, *J. Cryst. Growth*, 248:119, (2003).

[130] R. C. Newman, *Mater. Sci. Eng. B*, 66:39, (1999).

[131] C. Liu, O. Salehzadeh, P. J. Poole, S. P. Watkins, and K. L. Kavanagh, *Semi. Sci. Technol.*, 27**:**105020, (2012).

[132] A. A. Talin, F. Léonard, A. M. Katzenmeyer, B. S. Swartzentruber, S. T. Picraux, M. E. Toimil-Molares, J. G. Cederberg, X. Wang, S. D. Hersee, and A. Rishinaramangalum, *Semicond. Sci. Technol.*, 25:024015, (2010).

[133] A. D. Schricker, F. M. Davidson, R. J. Wiacek, and B. A. Korge, *Nanotech.*, 17:2681, (2006).

[134] D. Manasijevic, D. Zivkovic, N. Talijan, V. Cosovic, L. Gomidzelovic, R. Todorovic, D. Minic, J. Phys. Chem. Solids, 74:280, (2013).

[135] O.Salehzadeh, K. L. Kavanagh and S. P. Watkins, *J. Appl. Phys.*, 114:54301, (2013).

[136] X. Liu, V. G. Dubrovskii and X. Ren, *J. Phys. Condens. Matter*, 25:215302, (2013).

[137] H. Wang, L. A. Zepeda-Ruiz, G. H. Gilmer and M. Upmanyu, *Nature Commun.*, 4:1956, (2013).